Models for Compaction and Ejection of Powder Metal Parts

by

Jayant Khambekar

A Thesis

Submitted to the Faculty

of

Worcester Polytechnic Institute

In partial fulfillment of the requirements for the

Degree of Master of Science

In

Mechanical Engineering

By

April 2003

APPROVED:

Prof. Mark W. Richman, **Advisor.**	**Prof. Diran Apelian,** **Committee Member.**
Prof. Zhikun Hou, **Committee Member.**	**Prof. John M. Sullivan, Jr.,** **Graduate Committee Representative.**

ABSTRACT

We focus on single punch compaction of powder metals in hollow cylindrical geometries, and pay special attention to the effects of non-uniform initial density distribution on final green densities, the effects of density-dependent powder properties and pressure dependent coefficients of friction on the evolution of the pressure and density profiles during compaction, and the time variations of the force required for ejection after the compaction pressure is removed.

In studying the effects of non-uniform initial density distribution, we extend the work of Richman and Gaboriault [1999] to allow for fill densities that vary with initial location in the die. The process is modeled using equations of equilibrium in the axial and radial directions, a constitutive relation that relates the axial pressure to the radial pressure at any point in the specimen, and a plausible equation of state that relates local density to the local pressure. Coulomb friction is assumed to act at the interfaces between the specimen and both the die wall and core rod. In this manner, we determine the axial and radial variations of the final density, the axial, radial and tangential pressures, and the shear stress. Of special interest are the inverse problems, in which we find the required non-uniform initial density distribution that, in principle, will yield no variation in the final green density.

For incorporating the effect of pressure and density dependent powder properties, we employ a one-dimensional model that predicts the axial variations of the pressure and density. In this model, however, we incorporate the density dependence of the radial-to-axial pressure ratio, as well as the pressure-dependence of the coefficients of friction at the die wall and core rod. The density-dependence of the pressure ratio is based on the

experimental measurements of Trassoras [1998], and the pressure dependence of the friction coefficients is based on the measurements of Sinka [2000] and Solimanjad et. al [2001]. In the course of this study, we focus attention on a Distalloy AE powder, and establish the relation between its compressibility and its radial-to-axial pressure ratio.

Finally, we employ linear elasticity theory to model the ejection of the green compact. In the first phase, we model relaxation of the compact after removal of the compaction pressure as a misfit of three cylinders, representing the core rod, the compact and the die wall. The known input is radial pressure distribution at the conclusion of compaction, and the output is the corresponding radial pressure distributions that prevail after the compaction pressures are removed. In the second phase, we determine the variations with punch displacement of the ejection forces required to overcome friction at the core rod and die wall. The model includes additions to the friction forces due to the radial expansion (i.e. the Poisson effect) that occurs during ejection. Predictions of the model compare well to the experimental results of Gethin et.al. [1994].

ACKNOWLEDGEMENTS

I would like to thank all members in my defense committee, Prof. Diran Apelian, Prof. Zhikun Hou and Prof. John Sullivan for reading my thesis. Especially, I want to thank my advisor Prof. Mark Richman, without whose guidance the successful completion of this thesis was not possible. He has taken great pains to go out of his way to guide me through this endeavor. It is a pleasure to work with him.

Also, I would like to thank the Powder Metallurgy Research Center, Metal Processing Institute, WPI for its financial support for this work.

I am thankful to my colleague Ed Gaboriault, for his help during the initial stages of this work.

Finally, I want to express thanks to my parents Pappa and Mammi, my brother Nilesh, and my fiancée Aparna for their encouragement, support and understanding.

TABLE OF CONTENTS

LIST OF FIGURES

Chapter 2

Chapter 3

Chapter 4

CHAPTER 1

Introduction

Powder metallurgy (P/M) is an important process of manufacturing metal parts from metal in powdered form. Although it traces its roots, back to 3000 years B.C., the first modern powder metal product was the tungsten filament for electric light bulbs developed in the early 1900s. This was followed by tungsten carbide cutting tool materials in the 1930s, automobile parts like transmission gears, connecting rods, bearings, bushings in the '60s and '70s, aircraft turbine engine parts in the '80s and parts made by powder forging (P/F), metal injection molding (MIM) and warm compacting in the '90s. P/M parts are used in a variety of end products such as lock hardware, garden tractors, snowmobiles, automobile engines and transmissions, auto brake and steering systems, washing machines, power tools and hardware, sporting arms, copiers and postage meters, off-road equipment, hunting knives, hydraulic assemblies, x-ray shielding, oil and gas drilling wellhead components, fishing rods and wrist watches. Canadian nickels are made from strip rolled from pure nickel powder. The typical U.S. passenger car contains more than 37 pounds of P/M parts, a figure that will go higher within the next several years. New commercial aircraft engines contain 1,500-4,400 pounds of P/M superalloy extruded forgings per engine. Also, specialty P/M products such as superalloys, porous products, friction materials, strip for electronic applications, high strength permanent magnets, magnetic powder cores and ferrites, tungsten carbide cutting tools and wear parts, metal injection molded parts and tool steels are manufactured nowadays. The annual worldwide powder metal production exceeds one

million tons and the powder metal parts and products industry in North America alone has estimated sales of over $5 billion (White, 2001).

The basic P/M process uses pressure and heat to form precision metal parts and shapes. A mechanical or hydraulic compacting press squeezes powder in a rigid precision die into an engineered shape like a gear. After the mass of powder is squeezed into a shape and ejected from the press, it is fed slowly through a special high-temperature controlled atmosphere furnace to bond the particles together. They are metallurgically fused without melting, a phenomenon called "sintering". Other processes are also used to consolidate powders into finished shapes such as cold or hot isostatic pressing, direct powder rolling, forging, injection molding and gravity sintering. In contrast to other metal forming techniques, P/M parts are shaped directly from powders while castings are formed from metal that must be melted, and wrought parts are shaped by deformation of hot or cold metal, or by machining.

The process is not completely understood, scientifically, yet. Even today, the technology is still developing and provides a lot of scope for scientific research and industrial applications. Hence, comprehensive understanding of the P/M process is of vital importance for the industry.

1.1 Review of Previous Work

The complex nature of powder mechanical behavior coupled with complex geometries and boundary conditions, precludes analytical solutions to these problems. During the late 80s, maturing of numerical simulation to finite strain plasticity, allowed initial attempts of modeling powder compaction process. Formally, powder compaction

modeling requires the solution of a boundary value problem, a set of partial differential equations representing balance laws for mass, momentum and energy and constitutive laws giving relation between stress and strain and friction laws. Finite element method (FEM) is most widely used to solve these equations. Modern FEM codes incorporate constitutive models for a wide variety of materials.

Empirical constitutive laws have been developed based on stress-strain behavior observed. Development of constitutive law for plastically deforming materials requires knowledge of yield surface for the material, which is the surface in the stress space within which the material responds elastically. The size and shape of yield surface is a function of loading history.

Attempts were made to understand yield surface for the material. Kim, Suh and Kwon (1990) cold isostatically pressed tubes of iron powder, sintered them and then those tubes were tested in combined tension and torsion, to obtain yield surface. Brown and Weber(1988) demonstrated that the mechanical response of compacted and sintered powders is very different from that of only compacted powder. Sintering amounts to add to the strength of the compact. Watson and Wert (1993) compacted aluminium powders hydrostatically and by using closed die compaction. They performed uniaxial tensile and compressive tests on these samples to obtain yield surface. Once the yield surface is identified, it remains to develop appropriate laws for the expansion, translation and change in shape of the yield surface, as the material deforms plastically. Trasorras, Parameswaran and Cocks (1998) have summarized the work done by many researchers in this regard.

Morimoto, Hayashi and Takei (1982) analyzed the compaction of T shaped compact, using single and double punch compaction. Trasorras, Armstrong and McCabe (1994) analyzed the compaction of metal powders with ductile particles. Trasorras, Krishnaswamy, Godby and Armstrong (1995) modeled the compaction of metal powder to complicated gear geometry using finite elements method. Gethin, Tran, Lewis and Ariffin (1994) demonstrated that during compaction, particle rearrangement phase is important and occupies a significant portion of compaction process. Doremus, Geidreau, Debove, Lecot and Dao (1995) studied the important influence of deviatoric stress on densification, using a numerically controlled triaxial press. Sinka, Cocks, Morrison and Lightfoot (1999) performed similar triaxial consolidated compaction and also isostatic compaction with high pressure triaxial testing facility and obtained results which were in broad agreement with Doremus et al. (1995).

After modeling compaction, attempts were made to study the effects of different parameters on compaction. Gasiorek, Korczak and Kaminski (1989) studied the effect of compressibility of powder on compaction and showed that for metallic powders, the compactibility coefficient most likely will never be a constant in practical density range. Bocchini and Rapallo (1995) studied the effect of friction on compaction and proposed a simple model that will take into account the friction at the punch face. Roure, Bouvard, Doremus and Pavier (1999) used industrial type press which had measurement facilities for measuring upper and lower punch forces as well as average radial force. A mechanical analysis of the data obtained from the experiments showed that the ratio of radial to axial pressures also is not constant during compaction. The ratio increases with increase in the average compact density. Wikman, Solimanjad, Larsson, Oldenburg and

Haggblad (1999) modeled the variation of radial to axial pressure ratio with a Cap yield function. It was observed that the friction coefficient and radial to axial pressure ratio evolve during compaction in a manner such that their product remains roughly the same. Friction tests carried out using high pressure apparatus measured bulk coefficient of friction, i.e., the coefficient of friction that takes into account particle-wall friction as well as inter particle friction. This bulk coefficient of friction was found to increase during the initial stages of compaction and then decrease. Solimanjad, Wikstrom and Larsson (2001) designed a powder friction measuring device to measure the friction coefficient between powder particles and die wall. By measuring the torque required to prevent the upper punch from rotation in a rotating die assembly, actually coefficient of friction between the punch face and iron powder particles was measured. This coefficient of friction was found to decrease with increasing average compact density. Sinka, Cunningham and Zavaliangos et al. (2001) carried out experimental measurement of coefficient of friction for pharmaceutical powder and obtained qualitatively similar results. Also, comparison was done with modeling results using variation of the coefficient of friction as a function of pressure.

Modeling of relaxation and ejection remained neglected for a long time. Ferguson and Krauss (1984) applied finite elements method to investigate stress state developed in single and two level parts during ejection. Gethin, Ariffin, Tran and Lewis (1994) studied experimentally relaxation and ejection using different powders including iron, carbon, ceramic and bronze. It was found that relaxation is approximately elastic in all except the ceramic powders. The variation of required ejection force during ejection was also measured. Required ejection force was found to increase sharply at the beginning and

then decrease. Gethin, Lewis and Ariffin (1995) modeled relaxation and ejection by taking the elastic properties of the compact to be constant and compared with previous experimental results. Arrifin, Gethin and Lewis (1998) also measured variation of the required ejection force and obtained qualitatively similar results. Holownia (1996) studied ejection and demonstrated an effective way of reducing the required ejection force. Mosbah and Bouvard (1997) studied experimentally the density profiles before and after ejection of the compact and then compared finite element modeling results with the experimental.

Accurate estimation of the elastic properties of the compact, which include Young's modulus and Poisson's ratio, is essential in any modeling effort for ejection. Pavier and Doremus (1996) conducted experimental studies and observed that the elastic properties of the compact are not constant during compaction. Using cyclic loading technique they obtained the variation of Young's modulus with the average compact density. Pavier and Doremus (1999) obtained the variation of the Poisson's ratio as a function of the average compact density. Similar experiments were done by Mosbah, Bouvard, Ouedraogo and Stutz (1996).

Richman, Apelian and Burgos (1998) presented a simple phenomenological theory to model the process of powder compaction with the intention to reveal the underlying physics governing the process. The theory was presented for a frictionless compaction of a cylindrical compact with inner solid cylindrical region consisting of one powder and the outer annular region consisting of another powder. Richman and Gaboriault (1999) extended the theory to include frictional compaction of hollow cylindrical compact with uniform initial density.

1.2 Summary of Approach

There are many analyses available in literature which model the process of powder compaction. Though some of them are more accurate than the analysis we intend to present, because of their complicated nature they require intense numerical calculations to obtain solutions. We present a simple analysis that avoids intense numerical calculations. Our goal is to focus on the physics underlying the process, which even today is not entirely revealed.

In this work, we extend the theory of Richman and Gaboriault (1999) to include the effects of variation in material properties and to model the ejection phase. The theory assumes that all the particles have the same size and shape, such that the particle mass can be approximated as continuum. Also, input required is powder specific so that the theory is valid for any metal powder. Pressures are obtained using force equilibrium and momentum balance. Constitutive relation obtains the induced radial pressure in terms of applied axial pressure. The constant of proportionality, which is the radial to axial pressure ratio, indirectly measures the inter-particle friction. Density and pressures are related by an equation of state. The theory is for the plastic deformation zone only, in the stress space and hence this equation of state can replace the complicated yield surface concept.

In chapter 2, we find the effects of initial non uniformities in the fill density due to improper filling of the die or feed-shoe movement. The material properties, coefficient of friction and the radial to axial pressure ratio are taken as constants for simplicity. The compaction is carried out using only upper punch. The pressure variation in the compact is obtained and using that the density variation in three dimensions is predicted. Changes

in the profiles of density and pressure due to changes in the values of initial height of compact, final height, friction coefficient between the wall and particles, the ratio of the core rod radius to die wall radius are studied. Also, inverse solution is obtained, which prescribes how the initial fill can be improved to obtain a perfectly uniform green state.

Chapter 3 takes into account the variation of radial to axial pressure ratio with local density and pressure and also the variation of the coefficient of friction with the local pressure and density. The solution to the pressure distribution is sought by considering the force equilibrium of a thin slice of infinitesimal thickness under externally applied axial pressure and friction forces. The inertia forces arising due to instantaneous acceleration of the thin slice as it travels downwards during compaction and gravitational forces are neglected in favor of huge externally applied pressure force. So, the model does not take into to the effects of compaction velocity. Same equation of state governs the relation between local pressure and density.

Chapter 4 discusses the ejection problem. After the removal of external axial pressure, walls confining the compact spring back and produce a different radial pressure distribution compared to the one at the end of compaction. This radial pressure distribution gives rise to frictional forces that dictate the required ejection force. The solution to the radial pressure distribution is sought by solving a problem of elasticity in which three cylinders are inserted into one another. The variation of the required ejection force during ejection is obtained.

CHAPTER 2

Compaction in Hollow Cylindrical Dies with Non uniform Initial Density Distribution

2.1 Governing Equations and Boundary Conditions

We are concerned with single punch compaction of a powder in a hollow cylindrical die of inside radius R_i and outside radius R_o. The height of the powder fill before compaction is L, and the current height, at any instant during compaction is H. The geometry of the compact is described by the following dimensionless quantities: the radii ratio $a \equiv R_i/R_o$, which is a measure of the wall thickness of the compact; the height ratio H/L, which is a measure of the degree of compaction; and the aspect ratio $h \equiv H/R_o$, which is a dimensionless measure of the instantaneous height of the compact. The geometry of the compact is shown in Figure 2.1.

The average pressure applied over the top surface of the compact is p_o, so that the total compaction load F_C is equal to $\pi(R_o^2 - R_i^2)p_o$. We establish a cylindrical coordinate system in which the axial Z^*-coordinate measures the initial distance along the centerline from the lower face of the fill, before compaction and the radial R^*-coordinate measures the initial distance from centerline. In a similar way, the axial z^*–coordinate measures the instantaneous distance along the centerline from the lower face of the compact, during compaction and the radial r^*-coordinate measures the instantaneous distance from the centerline. The angular position about the centerline is measured by θ. If there is symmetry, there will be no variations with angular position, θ. But even for small variations with angular position about the centerline, the pressure distribution can be

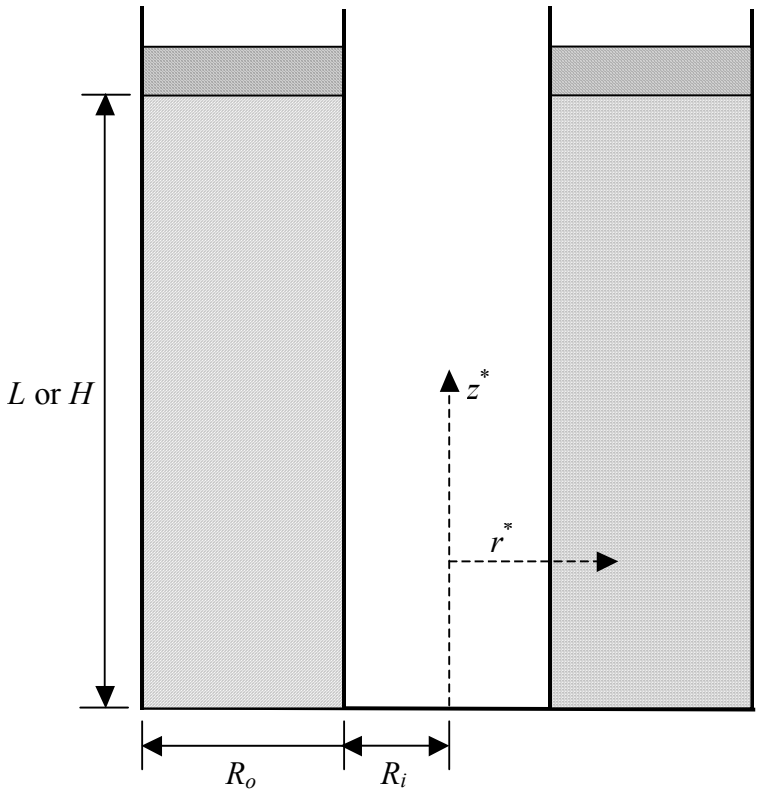

Figure 2.1: The pre- and post-compaction geometry.

assumed to be almost independent of angular position. In this case, the axial pressure p^*, the radial pressure σ^*, the tangential pressure φ^* and the shear stress τ^* each vary with only r^* and z^* throughout the compact.

In what follows, we employ a dimensionless axial coordinate, $Z \equiv Z^*/L$ which varies from 0 at the bottom of the compact to 1 at the top and a dimensionless radial coordinate $R \equiv R^*/R_o$ which varies from a at the core rod to 1 at the die wall. Similarly, $z \equiv z^*/H$ varies from 0 at the bottom of the compact to 1 at the top and $r \equiv r^*/R_o$, varies from a at the core rod to 1 at the die wall. The corresponding angular coordinates are Θ before compaction and θ during compaction. In what follows we consider perfectly axisymmetric cases or cases in which the inhomogeneities in initial fill contain only small variations with Θ. Under these circumstances, a complete description of the deformation during compaction is given by the functions $z(R,Z)$ and $r(R,Z)$. If z depends on R, then flat "discs" of powder in the pre-compaction state will not remain flat in the evolving state. Wherever r is not equal to R, radial movement of the powder will occur.

The dimensionless axial pressure, $p \equiv p^*/p_o$ and the dimensionless radial pressure, $\sigma \equiv \sigma^*/p_o$, the dimensionless tangential pressure, $\varphi \equiv \varphi^*/p_o$, and the dimensionless shear stress, $\tau \equiv \tau^*/p_o$ vary with r and z. In what follows, we carry out all calculations in terms of dimensionless quantities.

In terms of the axial pressure p and the shear stress τ, the axial equilibrium equation is given by,

$$\frac{\partial p}{\partial z} = \frac{h}{r}\frac{\partial (r\tau)}{\partial r} \quad . \tag{2.1}$$

Here, in what follows, we assume that the radial pressure σ is equal to the tangential pressure φ. In terms of the radial pressure σ and the shear stress τ, the radial equilibrium equation is,

$$\frac{\partial \sigma}{\partial r} = -\frac{1}{h}\frac{\partial \tau}{\partial z} \quad . \tag{2.2}$$

The tangential equilibrium equation is identically satisfied. In this model, the radial pressure σ is induced by an axial pressure p according to the simple constitutive relation,

$$\sigma = \alpha p \quad , \tag{2.3}$$

where α is the radial-to-axial pressure ratio of the powder that measures the tendency of the powder to develop radial pressure when subjected to axial pressure. Values of α vary between 0 and 1. For simplicity, we take α to be a constant and ignore its variations with density in the course of compaction. The constant value may be crudely interpreted as an average value over the entire compact during the entire compaction process.

With appropriate boundary conditions, equations (2.1), (2.2) and (2.3) determine the variations of the axial pressure, the radial pressure, and the shear stress. Boundary conditions at the die wall and the core rod relate the shear stress to the radial pressure through Coulomb friction. If, for example, μ_o is the coefficient of friction between the die wall and the powder compact, then the boundary condition at r=1 is given by,

$$\tau(r=1,z) = \mu_o \sigma(r=1,z) \quad . \tag{2.4}$$

Similarly, if μ_i is the coefficient of friction between the core rod and the powder compact, then the corresponding boundary condition at $r=a$ is

$$\tau(r=a,z) = -\mu_i \sigma(r=a,z) \quad . \tag{2.5}$$

It is possible to obtain closed form expressions for the pressures p and σ, and the shear stress τ that satisfy equations (2.1) to (2.3) and conditions (2.4) and (2.5).

Constitutive relation (2.3) may be employed to eliminate σ from the radial equilibrium equation (2.2). The result may be combined by cross differentiation with axial equilibrium (2.1) to yield a single equation for p, given by,

$$\frac{\partial^2 p}{\partial z^2} = \frac{h^2 \alpha}{r} \frac{\partial}{\partial r}\left(r \frac{\partial p}{\partial r} \right) \quad . \tag{2.6}$$

In order to express conditions (2.4) and (2.5) entirely in term of the axial pressure p, we employ constitutive relation (2.3) to write the radial pressure σ in terms of the axial pressure p, differentiate the two conditions with respect to z, and employ equation (2.2) to eliminate $\partial \tau/\partial z$ from the intermediate results. In this manner, we obtain

$$h \frac{\partial p}{\partial r} = \mu_o \frac{\partial p}{\partial z} \quad , \tag{2.7}$$

at $r=1$, and

$$h \frac{\partial p}{\partial r} = -\mu_i \frac{\partial p}{\partial z} \quad , \tag{2.8}$$

at $r=a$. Equation (2.6) and conditions (2.7) and (2.8) determine $p(r,z)$. In the case of a solid cylindrical compact, the ratio a is equal to 0, and condition (2.8) at $r=a$ is replaced by the simple requirement that the stresses remain finite at $r=0$.

Based upon the form of equation (2.6), the axial pressure has the form :

$$p(r,z) = F(z)G(r) \quad . \tag{2.9}$$

When this form is substituted in equation (2.6) and the z and r dependence are separated, we find that both F and G are the solutions to two second order well known ordinary differential equations. In this manner, we find that

$$F(z) = A\left[\exp(\lambda z) + B\exp(-\lambda z)\right] \quad , \tag{2.10}$$

and

$$G(r) = \frac{C}{A}\left[I_o(\lambda r / h\sqrt{\alpha}) + DK_o(\lambda r / h\sqrt{\alpha})\right] \quad . \tag{2.11}$$

Reassembling the product of F and G according to equation (2.9)gives the axial pressure $p(r, z)$ to within four unknown constants (B, C, D, and λ). The manner in which these constants are determined depends on whether the compact is a solid cylinder (with no core rod), or a hollow cylinder (with core rod surface at $r=a$). Each of this case will be treated separately in sections 2.3 and 2.4.

Once the axial pressure $p(r,z)$ is determined, the radial pressure $\sigma(r,z)$ can be fixed by the simple constitutive relation (2.3), and the shear stress $\tau(r,z)$ is determined to within additional constant by integrating equations (2.1) and (2.2). The constant is fixed as follows. We define the average pressure $P(z)$ at any axial location z according to

$$P(z) \equiv \frac{2}{(1-a^2)} \int_a^1 p(r,z)\, r dr \quad . \tag{2.12}$$

and we require that at z=1,

$$P(z{=}1) = 1 \quad . \tag{2.13}$$

This in turn guarantees that the average of the *dimensional* axial pressure on the top face is equal to p_o, as it must be.

2.2 Equation of State and Mass Balance

The equation of state relates the axial pressure $p^*(r, z)$ to the corresponding local density $\rho^*(r, \theta, z)$. A relatively simple equation of state has the form,

$$\rho^* = \eta^* \left[1 + k(1-\alpha) p^*\right] \quad , \tag{2.14}$$

where $k(1\text{-}\alpha)$ is the compressibility of the specimen at any stage of the compaction and $\eta^*(R, \theta, Z)$ is the apparent density of the loose powder. The compressibility is the slope of the variation of ρ^* with p^*, and it vanishes when the deformation is incompressible (when, for example, α=1). Because the initial fill can be nonuniform, η^* can depend on R, θ, and Z. By assumption, the Θ dependence will be small. The compressibility $k(1\text{-}\alpha)$ is itself a decreasing function of density, so that equation (2.14) actually describes a nonlinear relationship between density ρ^* and pressure p^*. As ρ^* increases from the apparent density η^* of the powder, the compressibility decreases monotonically from its initial value $\beta(1\text{-}\alpha)$. Moreover, as ρ^* approaches its maximum theoretical value M, the

local compressibility approaches zero. The simplest relation between k and ρ^* that satisfies these conditions is

$$k = \beta\left[1 - \frac{\rho^* - \eta^*}{M - \eta^*}\right] \quad . \tag{2.15}$$

By eliminating k between equations (2.14) and (2.15), we obtain the following equation of state:

$$\frac{\rho^*}{\eta^*} = \frac{(M - \eta^*) + \beta(1-\alpha)Mp^*}{(M - \eta^*) + \beta(1-\alpha)\eta^* p^*} \quad . \tag{2.16}$$

If we non-dimensionalize the densities by the maximum theoretical value, M, then $\eta \equiv \eta^*/M$ represents nondimensional initial density and $\rho \equiv \rho^*/M$ represents relative local density during compaction. Equation (2.16) can be written in nondimensional form as :

$$\frac{\rho}{\eta} = \frac{(1-\eta) + (1-\alpha)\beta p_o p}{(1-\eta) + \eta(1-\alpha)\beta p_o p} \tag{2.17}$$

The nondimensional average density $\rho_{avg} \equiv \rho^*_{avg}/M$ at any height z is defined by the integral,

$$\pi(1-a^2)\rho_{avg} = 2\pi\int_a^1 \rho(r,z) r dr \quad . \tag{2.18}$$

The quantity ρ_{avg} is of special interest because it can be determined experimentally by measuring the weight of very thin annular disks that are successively removed from the green compact.

Finally, we imagine that the compact is comprised of infinitely many thin flat circular discs that are perpendicular to the centerline, and we approximate the deformation during compaction by assuming that each disc remains flat during compaction. Under these circumstances, the balance of mass requires that the mass of each disc (of thickness dZ before compaction, and thickness dz after compaction) must remain constant through the compaction cycle. Therefore, the final axial location z is independent of the initial radial location, and the balance of mass becomes

$$LdZ \int_a^1 \int_0^{2\pi} \eta R dR d\Theta = Hdz \int_a^1 \int_0^{2\pi} \rho r dr d\theta \quad . \tag{2.19}$$

If, in addition, the dependence of η on the angular coordinate Θ is small, then the dependence of z on Θ can be neglected. In that case, z is a function of Z only, and equation (2.19) can be written as the following ordinary differential equation:

$$\frac{dz}{dZ} = \frac{L \int_a^1 \int_0^{2\pi} \eta R dR d\Theta}{H \int_a^1 \int_0^{2\pi} \rho r dr d\theta} \quad . \tag{2.20}$$

The boundary conditions require that the bottom of the compact does not move during compaction, and that the particles that comprise the top surface of the compact remain unchanged during compaction. In mathematical terms, these conditions are simply,

$$z(Z=0) = 0 \qquad \text{and} \qquad z(Z=1) = 1 \quad . \tag{2.21}$$

In what follows, it is assumed for simplicity that the radial and angular locations don't change during compaction, so that $r=R$ and $\theta=\Theta$.

2.3 Solid Cylindrical Compacts

In the case of solid cylindrical compacts, there is no core rod and $a=0$. Coulomb friction conditions (2.5) and (2.8) at $r=a$ are replaced by the requirement that the stresses and pressures remain finite at the centerline ($r=0$) of the cylindrical compact. This in turn implies that the constant D must vanish in expression (2.11).

The remaining constants (B, C, and λ) in $p(r, z)$ may be determined as follows. First, the form of axial pressure given by equation (2.9) is substituted in Coulomb friction condition (2.7) at the die wall. This yields a simple first order differential equation for $F(z)$, from which we obtain,

$$F(z) = Q_o \exp\left\{\left[\frac{hG'(1)}{\mu_o G(1)}\right] z\right\} \quad . \tag{2.22}$$

where Q_o is an unknown constant and the primes denote differentiation with respect to r. By comparing equations (2.22) and (2.10), we find that $B=0$ and that,

$$\lambda = \frac{hG'(1)}{\mu_o G(1)} \quad . \tag{2.23}$$

With $G(r)$ (with $D=0$) given by equation (2.11), equation (2.23) yields the transcendental relation,

$$\mu_o \sqrt{\alpha}\, I_o(\lambda/h\sqrt{\alpha}) = I_1(\lambda/h\sqrt{\alpha}) \quad , \tag{2.24}$$

that determines λ as a function of the products $\mu_o\sqrt{\alpha}$ and h$\sqrt{\alpha}$. For prescribed values of these products, equation (2.24) may be solved numerically by Newton-Raphson iteration to determine λ.

With the constants B=0 and D=0, the product (2.9) for $p(r, z)$ reduces to,

$$p(r,z) = C\exp(\lambda z)\, I_0(\lambda r/h\sqrt{\alpha}) \quad . \tag{2.25}$$

The expression for the radial pressure $\sigma(r, z)$,

$$\sigma(r,z) = C\alpha\exp(\lambda z)\, I_0(\lambda r/h\sqrt{\alpha}) \quad . \tag{2.26}$$

is obtained from constitutive relation (2.3). The corresponding expression for the shear stress $\tau(r, z)$ is obtained by integrating axial equilibrium equation (2.1) with respect to r, integrating radial equilibrium equation (2.2) with respect to z, and ensuring that the two results are consistent. In this manner, we obtain

$$\tau(r,z) = C\sqrt{\alpha}\exp(\lambda z)\, I_1(\lambda r/h\sqrt{\alpha}) \quad . \tag{2.27}$$

In order to completely specify the pressures and the shear stress, it remains only to determine the constant of integration C.

Constant C is determined by integral force balance (2.13). With $p(r,z)$ given by equation (2.25), the integration for the average pressure at the top of the compact yields,

$$C = \frac{\lambda e^{-\lambda}}{2h\sqrt{\alpha}\, I_1(\lambda/h\sqrt{\alpha})} \quad . \tag{2.28}$$

With C determined in this fashion, equations (2.25), (2.26), (2.27) completely determine the r- and z-variations of the dimensionless axial pressure $p(r, z)$, the radial pressure $\sigma(r, z)$ and the shear stress $\tau(r, z)$ throughout the solid cylindrical compact. The average pressure at any height is then calculated by substituting equation (2.25) for p in integral definition (2.12) to yield,

$$P(z) = \frac{2C\exp(\lambda z)}{(1-a^2)\Lambda^2}\left[\Lambda I_1(\Lambda) - a\Lambda I_1(a\Lambda)\right] \quad , \tag{2.29}$$

in which $\Lambda \equiv \lambda/h\sqrt{\alpha}$.

The quantities p, σ, τ, and P are each scaled by the average pressure p_o applied to the top surface of the compact. If p_o is specified, then the height H of the compact is to be determined. If, on the other hand, the height H is specified, then it remains to find p_o.

2.4 Hollow Cylindrical Compacts

For hollow cylindrical compacts, Coulomb friction conditions (2.7) and (2.8) apply at r=1 and r=a, respectively. As in the case of solid cylinders, condition (2.7) at r=1 yields exponential solution for $F(z)$ given by Equation (2.22). But now, an additional differential equation for $F(z)$ can be generated by substituting the product (2.9) into the Coulomb friction condition (2.8) at r=a. The solution to this equation is given by,

$$F(z) = Q_i \exp\left\{\left[-\frac{hG'(a)}{\mu_i G(a)}\right] z\right\} \tag{2.30}$$

By comparing Equations (2.10), (2.22) and (2.30), we conclude that $Q_o=Q_i=A$, $B=0$, and

$$\lambda = \frac{hG'(1)}{\mu_o G(1)} \qquad \text{and} \qquad \lambda = -\frac{hG'(a)}{\mu_i G(a)} \quad . \tag{2.31}$$

If expression for $G(r)$ given by equation (2.11) is employed in the first of equations (2.31), then the result is

$$D = \frac{I_1(\lambda/h\sqrt{\alpha}) - \mu_o\sqrt{\alpha} I_o(\lambda/h\sqrt{\alpha})}{\mu_o\sqrt{\alpha} K_o(\lambda/h\sqrt{\alpha}) + K_1(\lambda/h\sqrt{\alpha})} \quad . \tag{2.32}$$

In a similar manner, the second of equations (2.31) yields:

$$D = \frac{\mu_i\sqrt{\alpha} I_o(\lambda a/h\sqrt{\alpha}) + I_1(\lambda a/h\sqrt{\alpha})}{K_1(\lambda a/h\sqrt{\alpha}) - \mu_i\sqrt{\alpha} K_o(\lambda a/h\sqrt{\alpha})} \quad . \tag{2.33}$$

Equations (2.32) and (2.33) simultaneously determine the dependence of $\lambda/h\sqrt{\alpha}$ and D on $\mu_o\sqrt{\alpha}$, $\mu_i\sqrt{\alpha}$, and a. Solutions are obtained numerically via Newton-Raphson iteration.

With $B=0$, the product (2.9) for $p(r,z)$ reduces to,

$$p(r,z) = C\exp(\lambda z)\left[I_0(\lambda r/h\sqrt{\alpha}) + DK_0(\lambda r/h\sqrt{\alpha})\right] \quad , \tag{2.34}$$

and the expression for the radial stress $\sigma(r, z)$ is obtained from equation (2.3) as :

$$\sigma(r,z) = C\alpha\exp(\lambda z)\left[I_0(\lambda r/h\sqrt{\alpha}) + DK_0(\lambda r/h\sqrt{\alpha})\right] \quad . \tag{2.35}$$

The corresponding expression for the shear stress $\tau(r, z)$ is obtained by integrating axial equilibrium equation (2.1) with respect to r, integrating radial equilibrium equation (2.2) (with $\sigma=\alpha p$) with respect to z, and ensuring that the two results are consistent. In this manner, we obtain

$$\tau(r,z) = C\sqrt{\alpha}\exp(\lambda z)\left[I_1(\lambda r/h\sqrt{\alpha}) - DK_1(\lambda r/h\sqrt{\alpha})\right] \quad . \tag{2.36}$$

With D and λ determined by equations (2.32) and (2.33), the dimensionless shear stress and pressures are known to within a constant C.

The constant C is determined by integral condition (2.13). With $p(r,z)$ given by equation (2.34), the integration yields,

$$2C = \frac{(1-a^2)(\lambda/h)\exp(-\lambda)/\sqrt{\alpha}}{\left[I_1(\lambda/h\sqrt{\alpha}) - aI_1(\lambda a/h\sqrt{\alpha})\right] + D\left[K_1(\lambda/h\sqrt{\alpha}) - aK_1(\lambda a/h\sqrt{\alpha})\right]} \quad . \tag{2.37}$$

With C determined in this fashion, equations (2.34), (2.35), and (2.36) completely specify the r- and z-variations of the dimensionless axial pressure, radial pressure and the shear stress throughout the compact. The average pressure at any height is then calculated by substituting equation (2.34) for p in integral definition (2.12) to yield,

$$P(z) = \frac{2C\exp(\lambda z)}{(1-a^2)\Lambda^2}\left\{\Lambda I_1(\Lambda) - a\Lambda I_1(a\Lambda) + D\left[\Lambda K_1(\Lambda) - a\Lambda K_1(a\Lambda)\right]\right\} \quad , \tag{2.38}$$

in which in which $\Lambda\equiv\lambda/h\alpha^{1/2}$. The quantities p, σ, τ, and P are each scaled by the average pressure p_o applied to the top surface of the compact. If p_o is specified, then the height H

of the compact is to be determined. If, on the other hand, the height H is specified, then it remains to find p_o.

2.5 Solution Procedure

In the previous two sections, we have described how to compute the variations of the scaled pressures and shear stress in both solid and hollow compacts. The quantities that were prescribed were: h, a (for hollow cylinders), α, μ_o, and μ_i (for hollow cylinders). It remains to compute the average applied pressure p_o, which scales the pressures and the shear stress throughout, and the resulting density profiles in the compact.

First, we consider forward problems, in which the initial density distribution, $\eta(R=r,\Theta=\theta,Z)$ is prescribed and the final density distribution $\rho(\mathrm{r},\theta,\mathrm{z})$ is to be determined. In such problems, $\rho[\eta(r,\theta,Z),p(r,z),\beta p_o]$ is given by equation of state (2.17), and is employed in the balance of mass (2.20). For prescribed ratios H/L and an initial guess for βp_o, equation (2.20) is integrated subjected to the first of boundary conditions (2.21). We then iterate on the guess for βp_o until the second of conditions (2.21) is satisfied. With $z(Z)$ determined in this manner, it is inverted to determine $Z(z)$. The density profile $\rho(r,\theta,z)$ is then determined from equation of state (2.17) with $Z(z)$ used to eliminate Z.

Next, we consider inverse problems, in which the desired final density distribution, $\rho(r,\ \theta,\ z)$ is specified, and the required initial density distribution, $\eta(R=r,\Theta=\theta,Z)$ is determined. Of greatest interest are those initial density variations that yield perfectly uniform (i.e. $\rho\equiv$constant) final density profiles. In the inverse problem the initial density

$\eta[\rho(r,\theta,z),p(r,z),\beta p_o]$ is determined by inverting equation of state (2.17). In this manner, we find that the expression for $\eta[\rho(r,\theta,z),p(r,z),\beta p_o]$ is given by,

$$2(1-\eta)=-(1-\rho)\left[(1-\alpha)\beta p_o p-1\right]+\sqrt{(1-\rho)^2\left[(1-\alpha)\beta p_o p-1\right]^2+4(1-\rho)(1-\alpha)\beta p_o p}\quad , \tag{2.39}$$

and employ $\eta[\rho(r,\theta,z),p(r,z),\beta p_o]$ in balance of mass (2.20). Then, as in the forward problem, for prescribed ratios H/L and an initial guess for βp_o, equation (2.20) is integrated subjected to the first of boundary conditions (2.21). We then iterate on the guess for βp_o until the second of conditions (2.21) is satisfied. With $z(Z)$ determined in this manner the initial density profile $\eta(r=R,\theta=\Theta,Z)$ is then determined from the inverted equation of state (2.39).

2.6 Results and Discussion

In this section we present the results obtained using the solution procedure described above. First we focus on cases in which the initial fill is uniform and evaluate the extent of the nonuniformities in green density caused by friction at the core rod and die wall. Figure 2.2 shows the radial variation of density (at axial locations z=0, .25, .5, .75 and 1) resulting from a uniform initial fill η=.41 when the pre-compaction aspect ratio L/R_o=8.88, the final compaction height H/L=.45, the coefficients of friction $\mu_i=\mu_o$=.2, the radial-to-axial pressure ratio α=.5, and the ratio of radii $a\equiv R_i/R_o$=.5. The variation in density caused by friction at the die wall and core rod is almost entirely seen in differences in axial location; friction causes almost no variation of density with radial

location. In this case, due to friction, the density decreases by about 12.5 percent from the top to the bottom of the compact.

Figure 2.3 shows the corresponding axial variations of axial pressure, $\beta p_o p$, for different radial locations r=1, .9, .8, .7, .6 and .5. Friction causes the pressure to decrease with distance from the punch. In this case the pressure decreases by about 80 percent from the top to the bottom of the compact. This is an illustration of the equation of state, which predicts that at high pressures, large pressure differences give rise to considerably smaller density differences. The pressure profiles fall on top of each other, indicating that (like the densities) the pressures do not vary much in radial direction. Figure 2.4 shows an alternative view of the same axial pressure variations. For the same case, we show in Figure 2.5 the radial variations of the relative density, ρ, at a fixed axial location z=.5 for compaction heights H/L=1, .9, .8, .7, .6, .5 and .45. As expected, during compaction the relative density increases from η=.41 without much radial variation.

In general, the density may vary in both axial and radial directions. To crudely characterize these variations, we introduce parameters that describe their size and direction. For example, at any stage of compaction, the inside-to-outside density increase, δ_r , is defined by:

$$\delta_r \equiv \frac{\rho(r=1)-\rho(r=a)}{\rho(r=a)} \times 100 \quad . \tag{2.40}$$

The initial value of δ_r that describes the radial variation of the fill density is denoted by Δ_r. Non-zero values of Δ_r correspond to examples of nonuniform fill.

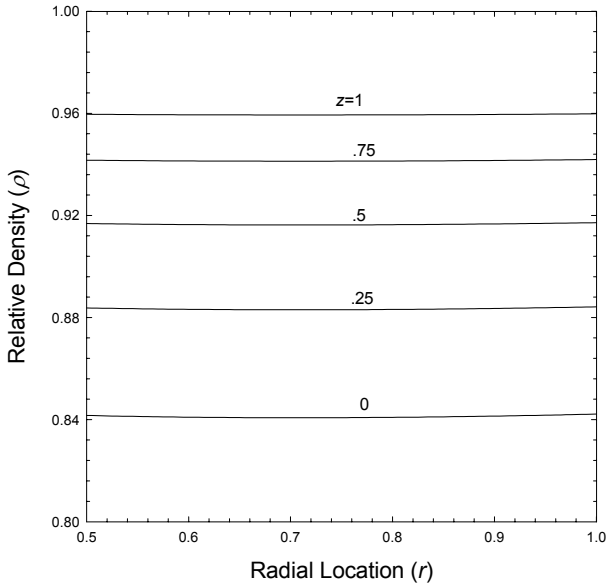

Figure 2.2: Variation of ρ with r for z =1,.75,.5,.25 and 0 for uniform initial density distribution and parameter values η=.41, R_i/R_o=.5, α=.5, $\mu_i=\mu_o$=.2 and L/R_o=8.88.

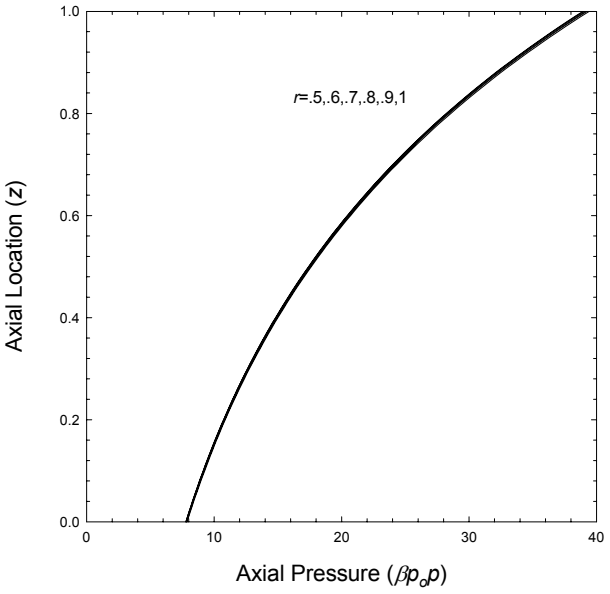

Figure 2.3: Variation of $\beta p_o p$ with z for r =1,.9,.8,.7,.6 and .5 for uniform initial density distribution and parameter values η=.41, R_i/R_o=.5, α=.5, $\mu_i=\mu_o$=.2, z =.5 and L/R_o=8.88.

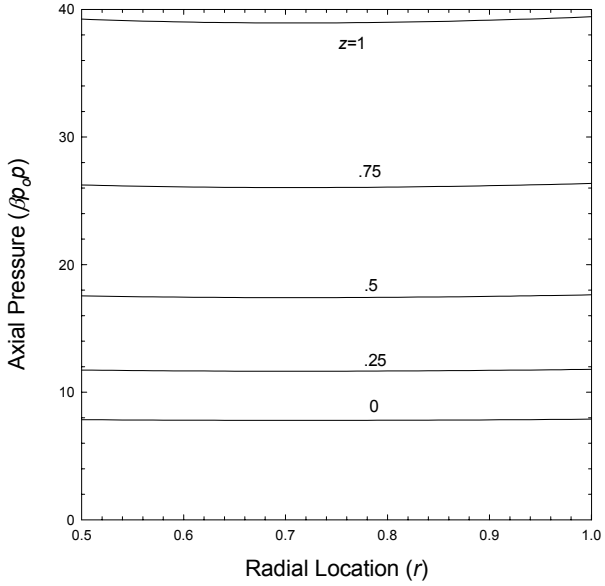

Figure 2.4: Variation of $\beta p_o p$ with r for z =1,.75,.5,.25 and 0 for uniform initial density distribution and parameter values η=.41, R_i/R_o=.5, α=.5, $\mu_i=\mu_o$=.2, and L/R_o=8.88.

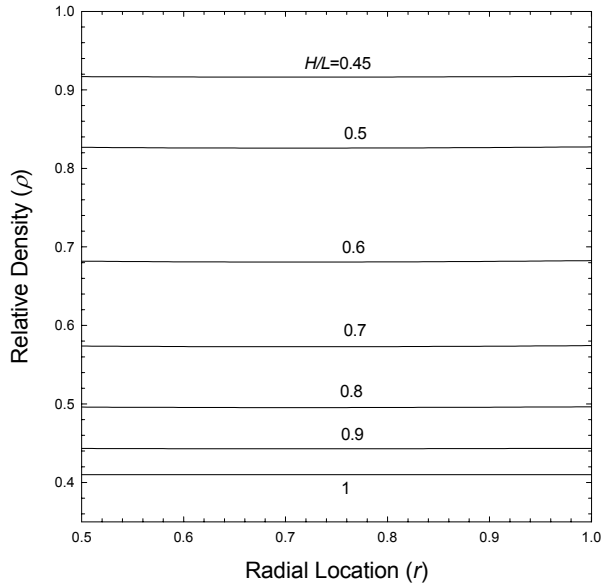

Figure 2.5: Variation of ρ with r for H/L=1,.9,.8,.7,.6,.5 and .45 for uniform initial density distribution and parameter values η=.41, R_i/R_o=.5, α=.5, $\mu_i=\mu_o$=.2, z=.5 and L/R_o=8.88.

In order to focus on the effects of nonuniform fill, in Figure 2.6, we show the variation of the δ_r with the compaction height H/L (at the bottom (z=0), mid-plane(z=.5), and top (z=1) when L/R_o=8.88, $\mu_i=\mu_o$=.2, α=.5, $a\equiv R_i/R_o$=.5, and η_{avg} =.41) for initial fills with radial density variations that are linear in r for which Δ_r=10% (solid), 0% (short dashed), and –10% (long dashed). The case of Δ_r=0% corresponds to uniform fill. As the compaction progresses, the initially non-uniformity decreases in magnitude. This is a "pancake effect" in which regions of relatively high density require higher pressures, which in turn drive powder to regions of lower pressure and density. The effect is most marked at the top where the pressures are highest. In this case, for example, with density variations reduce from 10% initially to about 1% finally. By contrast, at the bottom where the pressures are lowest, the variations reduce from 10% to about 3.8%. When the fill is initially uniform (i.e. Δ_r=0), almost no radial density variations are produced at any stage of the compaction.

Figures 2.7 show the variations with friction coefficients ($\mu_i=\mu_o$) of the inside-to-outside density increase δ_r when H/L=.45 at z=1,.75,.5,.25 and 0 for Δ_r=10 and -10 when η_{avg} =.41, a=.5, α=.5, and L/R_o=8.88. In both cases (Δ_r=10 and –10), when there is no friction, the radial density variation reduces to about 2 percent regardless of axial location. As coefficient of friction increases, however, the pressure required to carry out the compaction also increases, while the fraction of pressure reaching the bottom of the compact decreases. Consequently, the "pancake effect" is more pronounced near the top and less pronounced near the bottom of the compact. For extremely high friction coefficients, the pressures are extremely high near the top, and the initial non-uniformity in density is almost eliminated. But, the pressures near the bottom are relatively low, so

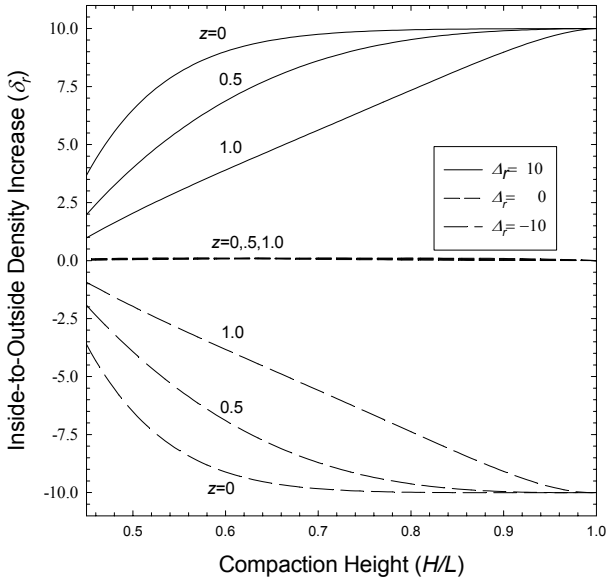

Figure 2.6: Variation of δ_r with H/L for z=1,.5 and 0 and for three different cases Δ_r=10, Δ_r=0 and Δ_r=-10 for parameter values η_{avg} =.41, R_i/R_o=.5, α=.5, μ_i=μ_o=.2 and L/R_o=8.88.

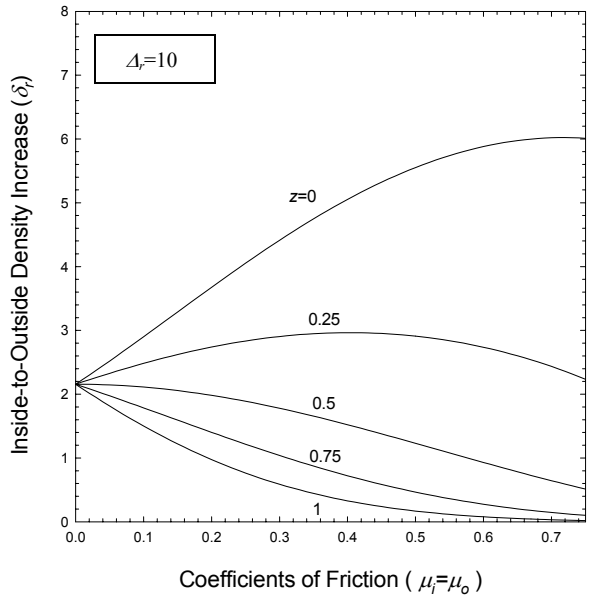

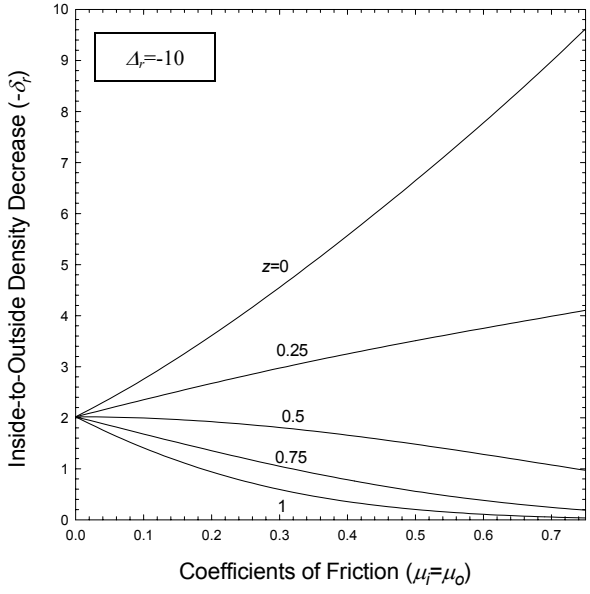

Figure 2.7: Variation of δ_r with μ_i=μ_o for axial locations z=1,.75,.5,.25 and 0 for Δ_r=10 and -10 for parameter values η_{avg} =.41, R_i/R_o=.5, α=.5, H/L=.45 and L/R_o=8.88.

the final nonuniformity is much larger than it would be in the absence of friction. Account must be taken of *both* the radial and axial density variations that result to see that the overall nonuniformity of the compact increases with increasing friction coefficients.

In a similar fashion, Figures 2.8 shows the effect of radial-to-axial pressure ratio, α, on the inside-to-outside density variations for the case considered in Figure 2.7 when H/L=.45 at z=1,.75,.5,.25 and 0 for Δ_r=10 and -10 when η_{avg} =.41, a=.5, $\mu_i=\mu_o$=.2, and L/R_o=8.88. Because increases in radial pressures give rise to increased friction forces at the die wall and core rod, the radial-to-axial pressure ratio has qualitatively similar effect on the density differences as do the coefficients of friction.

Figures 2.9 show the variation of the inside-to-outside density increase, δ_r, with the ratio of radii, $a \equiv R_i/R_o$ when H/L=.45 at z=1,.75,.5,.25 and 0 for Δ_r=10 and -10 when η_{avg} =.41, α=.5, $\mu_i=\mu_o$=.2, and L/R_o=8.88. As the ratio R_i/R_o increases to 1, the effects of friction and the therefore the required pressure for compaction increases. Consequently, the trends in Figures 2.9 are qualitatively similar to those in Figures 2.7 and 2.8.

From the results shown above when Δ_r=0, it is clear that if there are no radial variations in the initial fill, then the resulting radial variations in density will be extremely small. In these cases, there are only axial variations of density, and the average relative density, $\rho_{avg}(z)$, defined by equation (2.18) is an adequate descriptor of these density variations throughout the compact. At any stage of the compaction, we define $\bar{\rho}$ as the average density over the entire compact,

$$\bar{\rho} \equiv \int_0^1 \rho_{avg}(z)dz \quad , \tag{2.41}$$

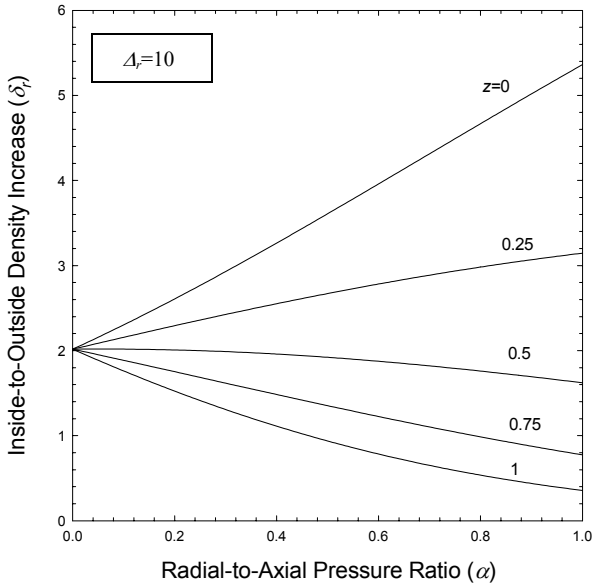

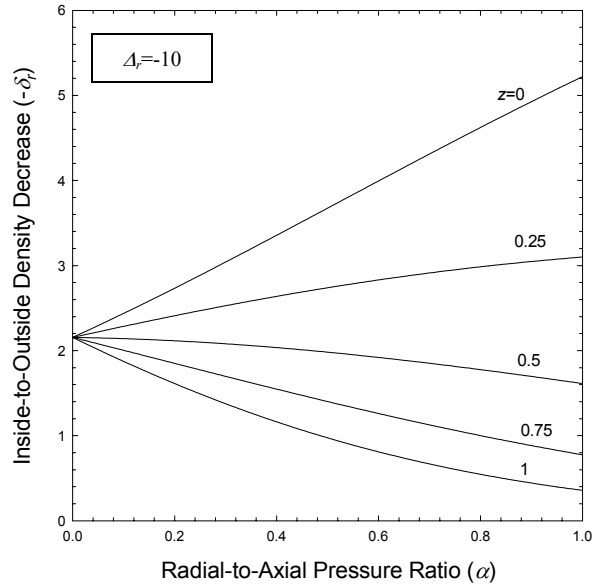

Figure 2.8: Variation of δ_r with α for z=1,.75,.5,.25 and 0 , for Δ_r=10 and -10 for parameter values η_{avg} =.41, R_i/R_o=.5, H/L=.45, μ_i=μ_o=.2 and L/R_o=8.88.

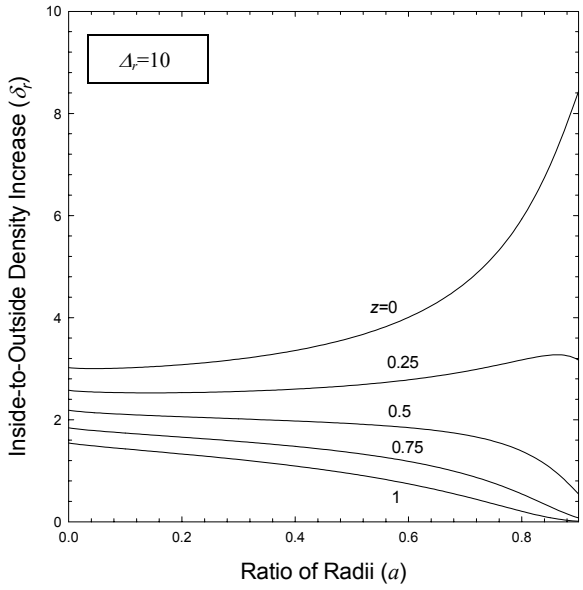

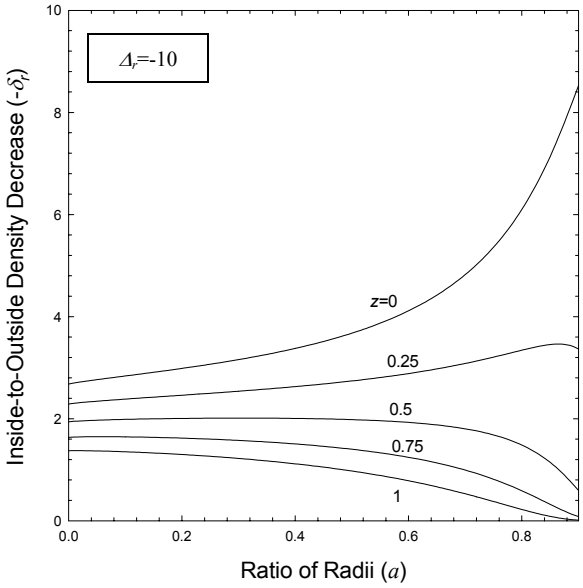

Figure 2.9: Variation of δ_r with a for z=1,.75,.5,.25 and 0 , for Δ_r=10 and -10 for parameter values η_{avg} =.41, α=.5, H/L=.45, μ_i=μ_o=.2 and L/R_o=8.88.

and denote by $\bar{\eta}$, the value of $\bar{\rho}$ just before compaction begins.

To measure axial variation in density at any stage of compaction, we define the top-to-bottom density *decrease* δ_z as:

$$\delta_z \equiv \frac{\rho_{avg}(z=1) - \rho_{avg}(z=0)}{\rho_{avg}(z=1)} \times 100 \quad . \tag{2.42}$$

The initial top-to-bottom density *increase* Δ_z=is the initial pre-compaction value of $-\delta_z$.

Figure 2.10 shows the axial variations of average relative density, ρ_{avg} at successive stages of compaction (H/L=1,.9,.8,.7,.6,.5 and .45) for a uniform initial fill ($\Delta_z=\Delta_r=0$) for $\bar{\eta}=\eta$=.41, α=.5, L/R_o=8.88, $\mu_i=\mu_o$=.2 and R_i/R_o=.5. At H/L=1, the density is uniform throughout. As expected, as compaction proceeds (and H/L decreases), the densities increase more rapidly near the top and less rapidly near the bottom. We also note that the percentage difference between the densities at the top and bottom increases in the early stages of compaction but decreases in the latter stages.

In Figures 2.11 we show how density distributions evolve when the initial fills have axial variations (Δ_z=10% and –10%) for the case corresponding to that described by Figure 10.. In the first of these cases (i.e. Δ_z=10%), the initial top-to-bottom density increase quickly reverses. At the end of compaction, (i.e. H/L=.45) the top-to-bottom density variation (.954-.856=.098), is less than that (.96-.84=.12) which resulted from the uniform fill shown in Figure 2.10. In the second case (i.e. Δ_z=-10%) the initial top-to-bottom density decrease is quickly increased. At the end of compaction, the top-to-bottom density variation (.965-.827=.138) is larger than that which resulted from the

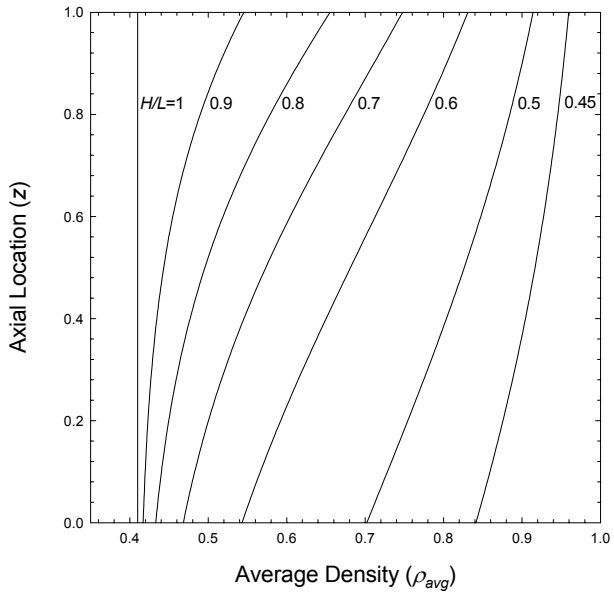

Figure 2.10: Variation of ρ_{avg} with z for H/L=1,.9,.8,.7,.6,.5 and .45 for uniform initial density distribution and for parameter values η=.41, α=.5, L/R_o=8.88, $\mu_i=\mu_o$=.2 and R_i/R_o=.5.

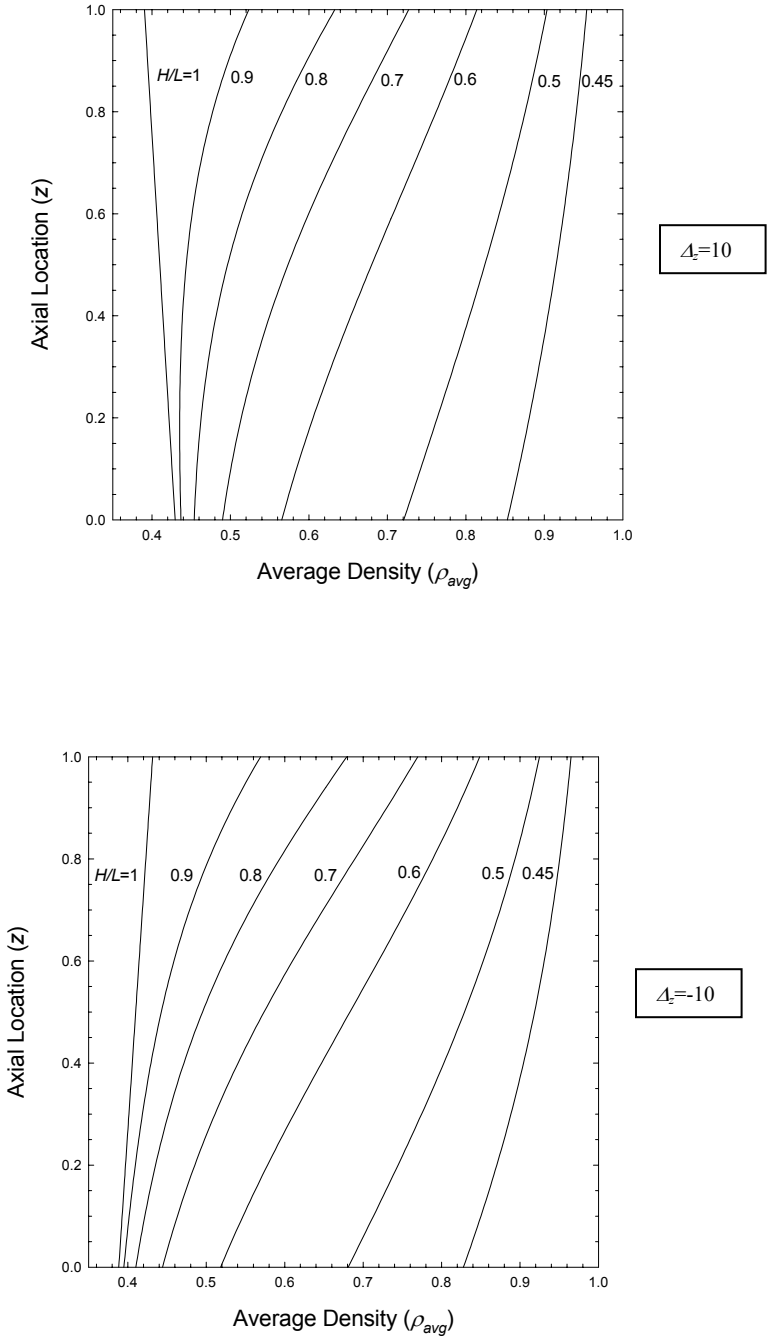

Figure 2.11: Variation of ρ_{avg} with z for H/L=1,.9,.8,.7,.6,.5 and .45 for Δ_z =10 and -10 and for parameter values $\bar{\eta}$=.41, α=.5, L/R_o=8.88, μ_i=μ_o=.2 and R_i/R_o=.5.

initially uniform fill.

In Figure 2.12, we show the evolution of the top-to-bottom density decrease δ_z during the compaction for three different cases shown in Figures 2.10 and 2.11 when initial density distribution, Δ_z=10%, 0%, -10%. In all three cases, because the pressures are much higher at the top than at the bottom of the compact, the top-to-bottom density decrease δ_z first increases to a maximum value. However, the compressibility of the powder is inversely related to its density, and at about H/L=.7, regions of lower density compress more readily than the regions of higher density even at significantly lower pressures. Consequently, at this stage of the compaction and beyond, the top-to-bottom density decrease actually diminishes. When Δ_z=0%, the final value of δ_z is 12.33%; when Δ_z=10%, the final value of δ_z is 10.59%; and when Δ_z=-10%, the final value of δ_z is 14.21%. These results are interesting because they suggests that more uniform compacts could be produced from non-uniform fills that are more dense at the bottom than at the top.

Next we now focus on how several other parameters affect the final axial variations of green density. In Figure 2.13, for example, we show the variation of top-to-bottom density δ_z with the coefficients of friction $(\mu_i=\mu_o)$ for the three cases Δ_z=10%, 0% 10% when $\bar{\eta}$=.41, α=.5, L/R_o=8.88, H/L =.45 and R_i/R_o=.5. As expected, increases in coefficients of friction result in increases of the final top-to-bottom density decrease, and as Δ_z increases, δ_z decreases.

In a similar manner, Figure 2.14 shows the variation of the top-to-bottom density decrease δ_z with the radial-to-axial pressure ratio, α for the three cases Δ_z=-10, Δ_z=10 and Δ_z=0 when when $\bar{\eta}$=.41, $\mu_i=\mu_o=.2$, L/R_o=8.88, H/L =.45 and R_i/R_o=.5. The

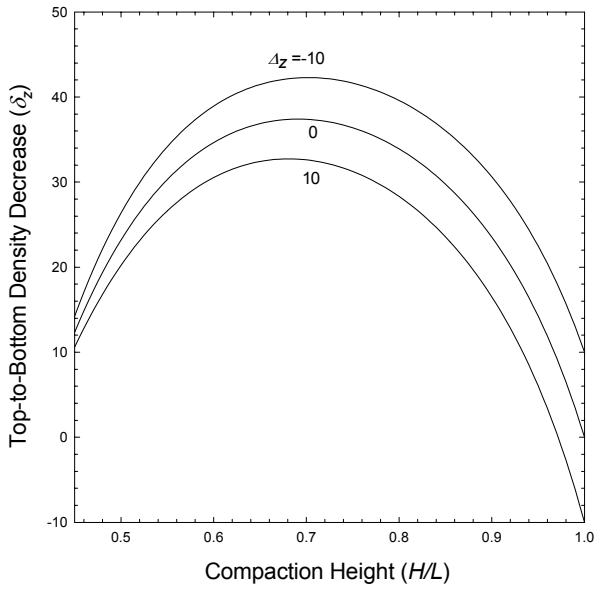

Figure 2.12: Variation of δ_z with H/L for different cases Δ_z =10, Δ_z =0 and Δ_z =-10 and for parameter values $\bar{\eta}$=.41, α=.5, L/R_o=8.88, μ_i=μ_o=.2 and R_i/R_o=.5.

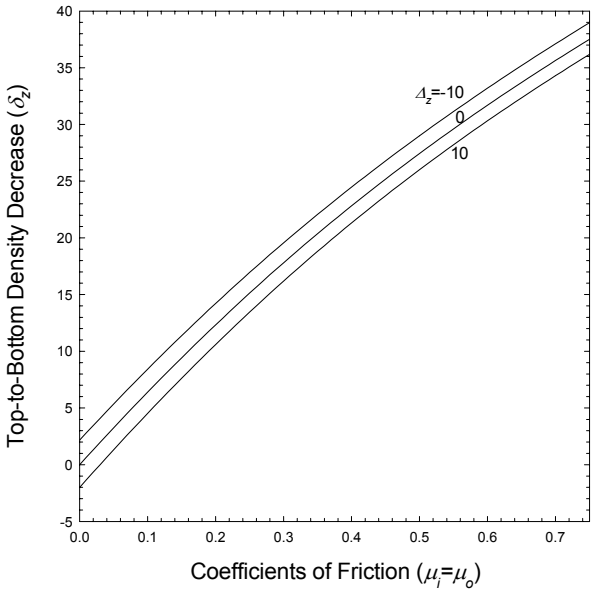

Figure 2.13: Variation of δ_z with μ_i=μ_o for different cases Δ_z =10, Δ_z =0 and Δ_z =-10 and for parameter values $\bar{\eta}$=.41, α=.5, L/R_o=8.88, H/L =.45 and R_i/R_o=.5.

effect of the parameter α, is qualitatively similar to that of coefficient of friction shown in Figure 2.13. For α=0, there is no radial pressure transmitted to the die wall and core rod. There is no friction developed there and the results are the same as in the frictionless case.

Figure 2.15 shows the effect of varying the ratio of radii, $a \equiv R_i/R_o$ on the resulting axial density variations for the same three cases when $\bar{\eta}$=.41, $\mu_i=\mu_o$=.2, L/R_o=8.88, H/L =.45 and α=.5. As a increases, the thickness of the compact decreases, the effect of die wall and core rod friction increases, and the non uniformity in the final density distribution increases.

In Figure 2.16, we show the variation of the final top-to-bottom density decrease δ_z with the initial top-to-bottom density increase Δ_z for $\mu_i=\mu_o$=0, .1, and .2 when $\bar{\eta}$=.41, L/R_o=8.88, H/L =.45, α =.5 and R_i/R_o=.5. For zero friction, a uniform initial fill results in a uniform final compact. In the presence of friction, on the other hand, zero top-to-bottom density variation in the final compact can in principle be achieved with an initial fill that has an appropriate top-to-bottom density decrease. The model predicts, for example, that when $\mu_i=\mu_o$=.1, a final density distribution with no top-to-bottom density variation will be obtained only if the die is filled such that it is 37.5 % more dense at the bottom than at the top.

In Figure 2.17, we show the variation of the final top-to-bottom density decrease δ_z with the initial top-to-bottom density increase Δ_z for different values of the post-compaction aspect ratio H/R_o=1, 2, 3 and 4 when $\bar{\eta}$=.41, $\mu_i=\mu_o$=.2, H/L =.45, α =.5 and R_i/R_o=.5. Again we can see that filling the die more densely at the bottom yields more uniform density distributions at the end of compaction. As the post-compaction aspect

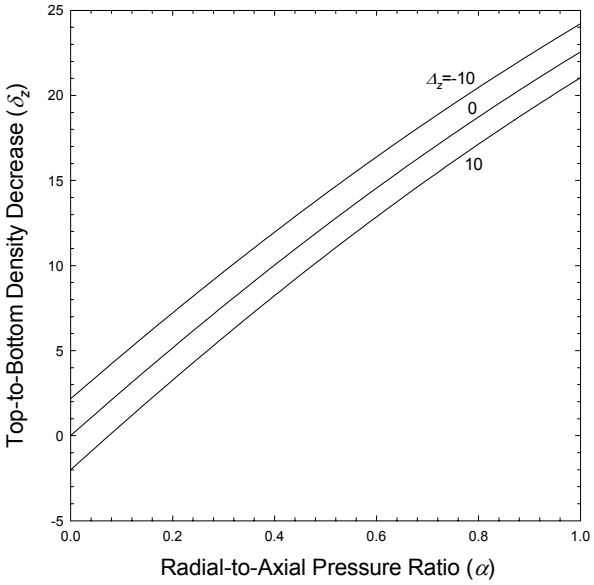

Figure 2.14: Variation of δ_z with α for different cases Δ_z =10, Δ_z =0 and Δ_z =-10 and for parameter values $\bar{\eta}$=.41, μ_i=μ_o=.2, L/R_o=8.88, H/L =.45 and R_i/R_o=.5.

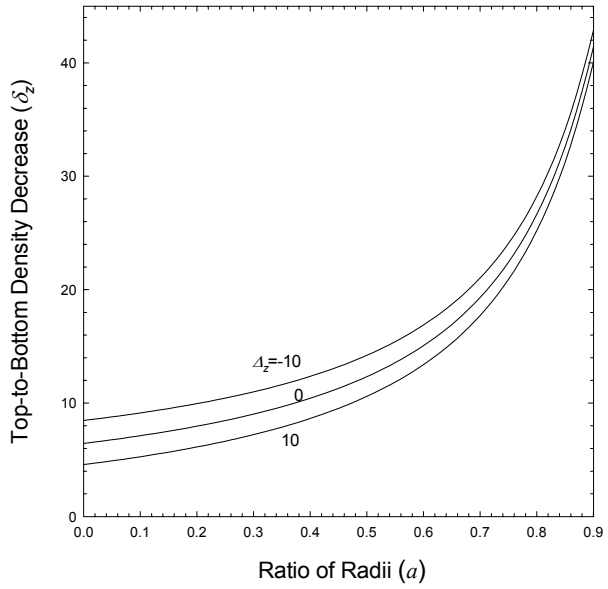

Figure 2.15: Variation of δ_z with R_i/R_o for different cases Δ_z =10 Δ_z =0 Δ_z =-10 and for parameter values η_{avg} =.41, μ_i=μ_o=.2, L/R_o=8.88, H/L =.45 and α =.5.

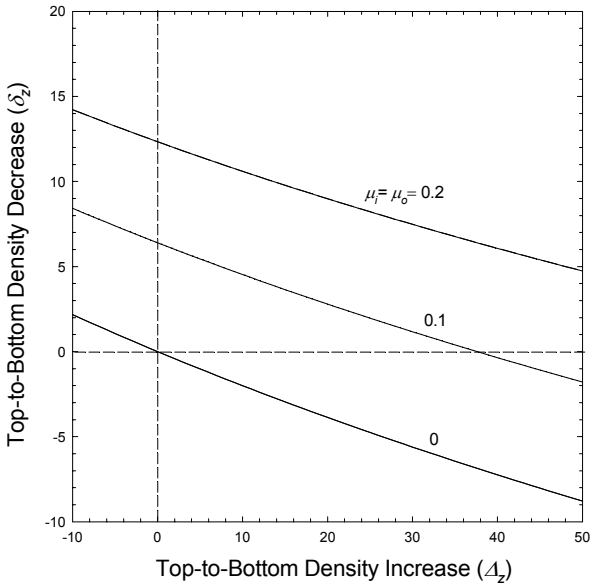

Figure 2.16: Variation of δ_z with Δ_z for three different cases $\mu_i=\mu_o=.2$, .1 and 0 and for parameter values $\bar{\eta}=.41$, $L/R_o=8.88$, $H/L=.45$, $\alpha=.5$ and $R_i/R_o=.5$.

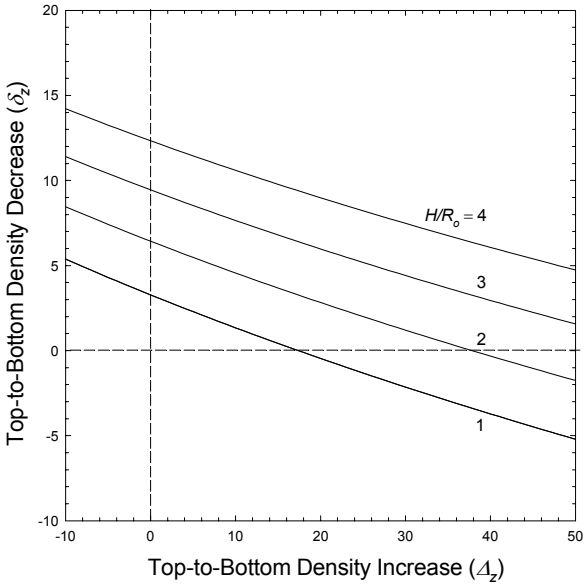

Figure 2.17: Variation of δ_z with Δ_z for four different cases $L/R_o=8.88$, 6.66, 4.44 and 2.22 and for parameter values $\bar{\eta}=.41$, $\mu_i=\mu_o=.2$, $H/L=.45$, $\alpha=.5$ and $R_i/R_o=.5$.

ratio H/R_o increases, the compact becomes longer, and the final non-uniformity of the compact increases. Consequently, the initial fill must be made increasingly more dense at the bottom to compensate for the increasing non-uniformity. For H/R_o=1, it is sufficient to fill the die 17.3% more densely at bottom to eliminate the final axial variation in density. By contrast, for H/R_o=2 the die must be filled such that the density is 37.7% greater at the bottom than at the top.

Figures 2.16 and 2.17 suggest that for a given set of parameters we can determine the exact non-uniformity required in the initial fill to obtain a perfectly uniform final density distribution. This is the fundamental idea behind a special class of "inverse problems" in which, more generally, we specify the desired density distribution at a prescribed stage of compaction and compute the required distribution of initial fill to achieve that distribution.

Figure 2.18, we take $\bar{\eta}$=.41, μ_i=μ_o=.2, L/R_o=8.88 α =.5 and R_i/R_o=.5 and show the evolution (at H/L=1, .9, .8, .7, .6, .5, and .45) of one such inverse solution. In this case, the prescribed density distribution at H/L=.45 was uniform (ρ_{avg}=.911 =.41/.45), and we find that in principle the initial fill should be nonlinear in z (as shown) such that the η_{avg} at the top is equal to .294 and increases to η_{avg}=.55 at the bottom (yielding Δ_z =86.8%). Of course, in practice it is not possible to achieve such large non-uniformities in initial density .

To focus on situations that may not require such large initial density variation, we consider a case in which the pre-compaction aspect ratio is L/R_o=4 and the ratio of radii is R_i/R_o=.25, while the remaining parameters are unchanged. Figure 2.19 shows the corresponding evolution of the inverse solution obtained here. In this case, to obtain a

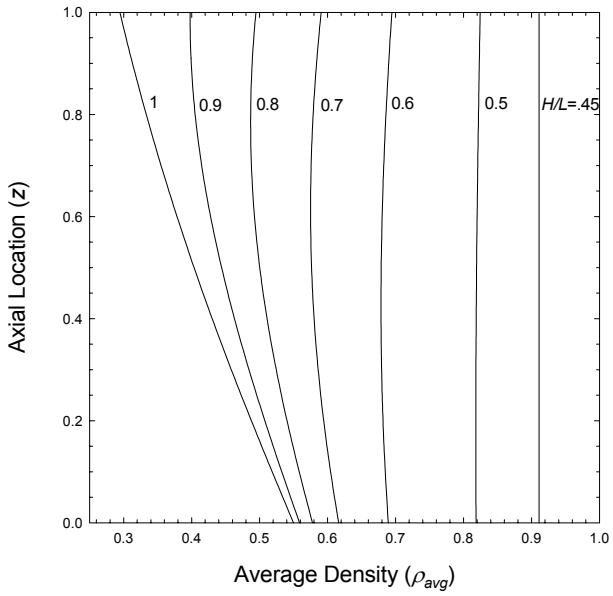

Figure 2.18: Variation of z with ρ_{avg} for H/L=1,.9,.8,.7,.6,.5 and .45 and $\delta_{\bar{z}}$=0 at H/L=.45, and for parameter values $\bar{\eta}$=.41, μ_i=μ_o=.2, L/R_o=8.88 α=.5 and R_i/R_o=.5.

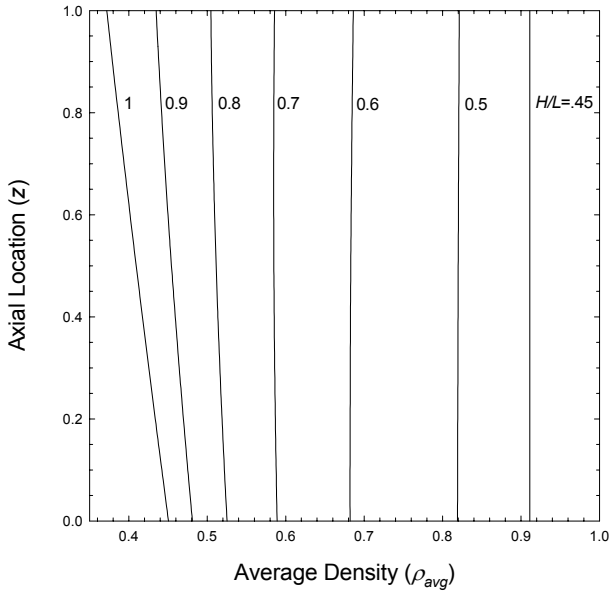

Figure 2.19: Variation of z with ρ_{avg} for H/L=1,.9,.8,.7,.6,.5 and .45 and $\delta_{\bar{z}}$=0 at H/L=.45, and for parameter values $\bar{\eta}$=.41, μ_i=μ_o=.2, L/R_o=4, α=.5 and R_i/R_o=.25.

perfectly uniform final density of ρ_{avg}=.911 at H/L=.45, we require the initial fill to be η_{avg}=.372 at the top and increase in a nonlinear way to η_{avg}=.450 at the bottom. Here the required value of Δ_z is decreased to 21%.

The inverse solutions obtained in Figures 2.18 and 2.19 demonstrate that the initial top-to-bottom density increase required to yield perfectly uniform green densities will vary widely depending on the values of the relevant parameters. In fact, the results suggest that only under special circumstances will it be possible in practice to actually fill the die with initial nonuniformities predicted by the model. In order to see how the top-to-bottom density variation (Δ_z) required for uniform green density changes with corresponding changes in coefficients of friction (μ_i=μ_o) and radial to axial pressure ratio (α), for example, we show in Figure 2.20 the variation of Δ_z with μ_i=μ_o for α= .4, .5 and .6, when $\bar{\eta}$=.41, L/R_o=4, R_i/R_o=.25 and H/L=.45. The top-to-bottom density decrease produced by a uniform initial fill becomes larger as either the coefficients of friction or the radial-to-axial pressure ratio increase. Figure 2.20 demonstrates that to exactly compensate for these phenomenon, the corresponding initial top-to-bottom density increase must get larger. Of course, when there is no friction at the die wall and core rod, a uniform initial density distribution is required to produce uniform final density distribution.

In Figure 2.21, we show the variation with precompaction aspect ratio L/R_o of the value of Δ_z required to produce uniform green density for a= .25, .4, and .5, when $\bar{\eta}$=.41, μ_i=μ_o =.2, α=.5 and H/L=.45. The top-to-bottom density decrease produced by a uniform initial fill becomes larger as either the aspect ratio increases or the wall thickness of the compact decreases (i.e. as R_i/R_o increases). Figure 2.21 demonstrates

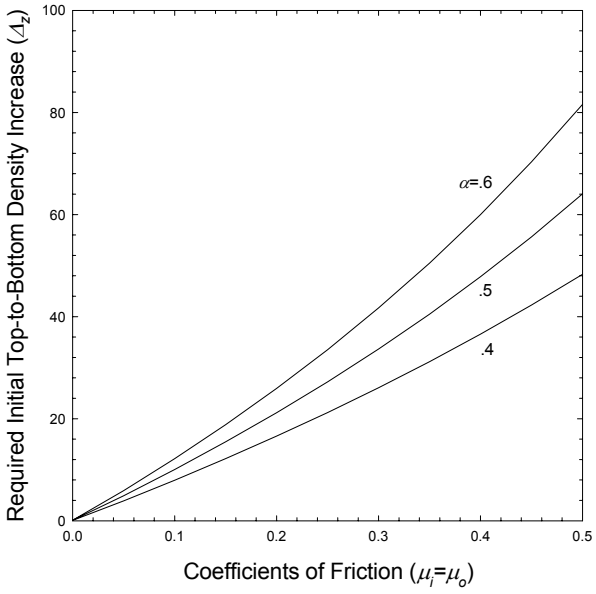

Figure 2.20: Variation of Δ_z with μ_i=μ_o for α =.6, .5 and .4 and δ_z=0 at H/L=.45, and for parameter values $\bar{\eta}$=.41, L/R_o=4, , R_i/R_o=.25 and H/L=.45.

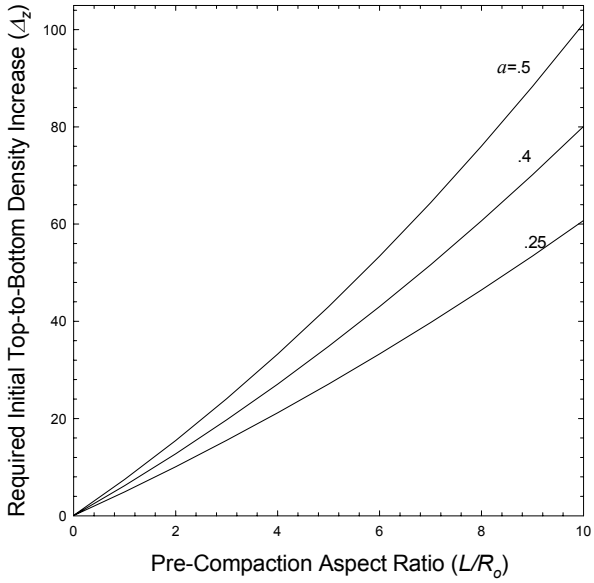

Figure 2.21: Variation of Δz with L/R_o for R_i/R_o=.25, .4 and .5 and δ_z=0 at H/L=.45, and for parameter values $\bar{\eta}$=.41, μ_i=μ_o =.2, α =.5 and H/L=.45.

that to exactly compensate for these phenomenon, the corresponding initial top-to-bottom density increase must get larger. Of course, as the height of the compact approaches zero, no axial variations in density are possible when the fill is uniform.

Figure 2.10 demonstrates that (for $\bar{\eta}=\eta=.41$, $\alpha=.5$, $L/R_o=8.88$, $\mu_i=\mu_o=.2$ and $R_i/R_o=.5$) when the fill is uniform, the top-to-bottom density decrease at $H/L=.45$ is $\delta_z=12.33\%$. For the same parameters, Figure 2.18 demonstrates that in order produce perfectly uniform green densities at $H/L=.45$, the initial top-to-bottom density increase must be $\Delta_z=86.8\%$. Because this axial variation is impractically large, we can instead require only that the density distribution be uniform at some intermediate stage of compaction. Although the final density distribution will then contain axial variations, we expect that these variations will be smaller than those produced by a uniform initial fill. As an illustration of this idea, we consider in Figure 2.22 the case in which $\bar{\eta}=.41$, $\mu_i=\mu_o=.2$, $\alpha=.5$, $L/R_o=8.88$ and $R_i/R_o=.5$, compute the initial density distribution that yields a perfectly uniform distribution at $H/L=.9$ (when the density is everywhere equal to .41/.9=.455), and track the evolution of the density profiles for $H/L=1$, .9, .8, .7, .6, .5 and .45. In this case, the required initial top-to-bottom density increase is $\Delta_z=32.5\%$, which is significantly lower than the 86.8% required to produce a uniform compact at $H/L=.45$. Moreover, final density variation is $\delta_z=8.12\%$, which is a significant improvement over the 12.33% variation that results form the uniform fill.

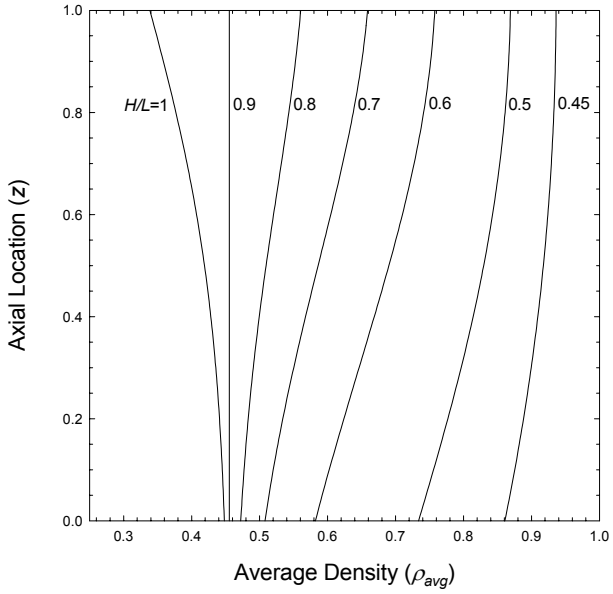

Figure 2.22: Variation of z with ρ_{avg} for H/L=1, .9, .8, .7, .6, .5 and .45 and δ_z=0 at H/L=.9 and for parameter values $\bar{\eta}$=.41, μ_i=μ_o =.2, α =.5, L/R_o=8.88 and R_i/R_o=.5.

CHAPTER 3

The Effects of Density-Dependent Powder Properties and Pressure-Dependent Coefficients of Friction on Compaction in Hollow Cylindrical Dies

3.1 Introduction

In the previous chapter, we modeled compaction with the powder properties, radial-to-axial pressure ratio, α, and coefficients of friction μ_i and μ_o, as constants throughout the process. But in modeling compaction of powder metal parts, it is critical that the radial-to-axial pressure ratio and friction between the compact and the die wall and core rod be properly incorporated because the friction forces that develop at these containing surfaces are responsible for the density variations that are of primary concern to part makers and part users. During compaction, the metal specimen evolves from its initially loose powdered state to its final green solid state. As a result, the nature of the interactions between the specimen and the containing surfaces changes dramatically from the beginning to the end of compaction

Frictional interactions between the evolving specimen and the surfaces that contain it may be approximated by Coulomb's law. Accordingly, the shear stress that develops at any such surface is proportional to the normal pressure that develops there. The factor of proportionality is the coefficient of friction appropriate to the surfaces in contact. Compaction models are typically restricted by the assumption that the coefficients of friction do not change during compaction. Further, the radial-to-axial pressure ratio is responsible for providing the normal pressure on the containing walls. During the three stages of compaction (rearrangement of particles, elastic deformation, and plastic deformation) the radial-to-axial pressure ratio varies with density at different

rates. To predict frictional forces correctly, it is therefore necessary to account for the density dependence of the coefficients of friction and the radial-to-axial pressure ratio. Ignoring the variations with density accounts for neither the roughly two-fold increase in average density that occurs as the compaction proceeds from beginning to end, nor the spatial variations in density that exist at any single stage of compaction.

We have identified several workers who have measured the dependence of the radial-to-axial pressure ratio and coefficient of friction on either pressure or density. In particular, we incorporate the experimental results of Trasorras et al [1998] for variation of radial-to-axial pressure ratio and the results of Sinka et.al. [2001] and Solimanjad et.al. [2001] for variation of coefficients of friction. We propose a mathematical dependence that is qualitatively similar to that measured by them, and employ it to predict how the density and pressure distributions evolve during compaction of bushing-like parts that have rotational symmetry about their centerlines. As expected, our results demonstrate that the manner in which the friction coefficients and radial-to-axial pressure ratio change during compaction strongly influence the manner in which the density distribution evolves to its green state.

3.2 Axial Equilibrium

We are concerned here with single punch compaction of a powder in a hollow cylindrical die of inside radius R_i and outside radius R_o. The height of the powder fill before compaction is L, and the current height, at any instant during compaction is H. The geometry of the compact is described by the following dimensionless quantities: the radii

ratio $a \equiv R_i/R_o$; the height ratio H/L, and the aspect ratio $h \equiv H/R_o$. The geometry of the compact has been shown in Figure 2.1.

The average pressure applied over the top surface of the compact is p_o. We establish a cylindrical coordinate system in which the axial Z^*-coordinate measures the initial distance from the lower face of the fill before compaction, and the radial R^*-coordinate measures the initial distance from centerline. In a similar way, the axial z^* coordinate measures the instantaneous distance from the lower face of the compact during compaction, and the radial r^*-coordinate measures the instantaneous distance from the centerline. In the axi-symmetric case, there is no variation with angular position. So, the axial pressure p^*, the radial pressure σ^* and the shear stress τ^* each vary with only r^* and z^* throughout the compact.

In what follows, we employ dimensionless axial coordinates $Z \equiv Z^*/L$ and $z \equiv z^*/H$, and dimensionless radial coordinates $R \equiv R^*/R_o$ and $r \equiv r^*/R_o$. The dimensionless axial pressure, radial pressure, and shear stress are defined by $p \equiv p^*/p_o$, $\sigma \equiv \sigma^*/p_o$, and $\tau \equiv \tau^*/p_o$, respectively. We carry out all calculations in terms of dimensionless quantities.

In terms of the axial pressure p and the shear stress τ, the axial equilibrium equation is given by,

$$\frac{\partial p}{\partial z} = \frac{h}{r}\frac{\partial (r\tau)}{\partial r} \quad . \tag{3.1}$$

As in Chapter 2, we assume that the radial and tangential pressures are equal. Coulomb friction at the core rod ($r=a$) and die wall ($r=1$) relate the shear stress to the radial

pressure there. If μ_i is the coefficient of friction at the core rod and μ_o is the coefficient of friction at the die wall, then the corresponding boundary conditions are,

$$\tau(r=a,z)=-\mu_i\sigma(r=a,z) \quad \text{and} \quad \tau(r=1,z)=\mu_o\sigma(r=1,z) \tag{3.2}$$

As compaction proceeds, the density of the compact, the frictional nature of the compact, and therefore the coefficients of friction μ_i and μ_o vary dramatically. The focus of this chapter is on quantifying these effects.

At any point in the powder during compaction, the local radial pressure σ is proportional to the local axial pressure p, so that,

$$\sigma=\alpha p \quad , \tag{3.3}$$

where α is the radial-to-axial pressure ratio that depends on the local value of the pressure and density within the evolving compact.

In order to calculate the radial and axial variations of p, σ, and τ, it would be necessary to introduce a radial equilibrium equation. However, of primary concern here are axial variations of the pressures (p and σ) and density. In order to average the effects of the radial variations without calculating them explicitly, we multiply equation (3.1) by $2r/(1-a^2)$, integrate from $r=a$ to $r=1$, and employ equations (3.2) and (3.3) to eliminate τ and σ. In this manner, the average pressure $P(z)$, defined by

$$P(z)=\frac{2}{(1-a^2)}\int_a^1 p(r,z)r\,dr \quad , \tag{3.4}$$

arises naturally, and we obtain the simple first order equation,

$$\frac{dP}{dz} = Q\alpha\left(\mu_o + a\mu_i\right)P \qquad , \tag{3.5}$$

in which $Q \equiv 2h/(1-a^2)$. Equation (3.5) could also be derived directly from a balance of forces on a compact slice of thickness dz.

At the top of the compact (z=1), the average of the dimensional pressure is equal to p_o. This condition becomes,

$$P(z=1) = 1 \qquad , \tag{3.6}$$

in dimensionless form. In principle, equation (3.5) can be integrated to determine the axial pressure variation to within a constant of integration determined by condition (3.6).

3.3 Equation of State and Balance of Mass

The average pressure P at any distance z is related to the corresponding average density. Here, we introduce the dimensionless density $\rho(z)$ equal to the average dimensional density at any height z scaled by the maximum theoretical density M. A plausible form of the equation of state that relates P to ρ, or inversely ρ to P, is,

$$\beta p_o P = \frac{(1-\eta)(\rho/\eta - 1)}{(1-\alpha)(1-\rho)} \qquad \text{or} \qquad \frac{\rho}{\eta} = \frac{(1-\eta)+(1-\alpha)\beta p_o P}{(1-\eta)+(1-\alpha)\eta\beta p_o P} \qquad , \tag{3.7}$$

where β is constant factor related to the compressibility of the loose powder, and $\eta(Z)$ is the average pre-compaction density (at any initial height Z) scaled by the maximum density M. Because η depends on Z, the model can incorporate the effects of non-uniform fill. Equations of state (3.7) require that the pressure vanish (P=0) when the

density is equal to the pre-compaction density ($\rho=\eta$), and that the pressure becomes unbounded when the density equals its theoretical maximum ($\rho=1$).

In this one-dimensional model, the compact can be viewed as infinitely many thin discs that remain flat during compaction. Under these circumstances the final axial location z depends on the initial axial location Z but not on the initial radial location R. The balance of mass requires that the mass of each disc with thickness LdZ before compaction be equal to the mass of the corresponding disc with thickness Hdz after compaction. In terms of the densities η before compaction and ρ after, the balance of mass becomes simply,

$$\frac{dZ}{dz} = \frac{H}{L}\frac{\rho}{\eta} \quad . \tag{3.8}$$

Because the bottom surface of the compact remains stationary and at all stages of compaction, the top of the fill corresponds to the top of the compact, the boundary conditions that must be satisfied are

$$Z(z=0)=0 \qquad \text{and} \qquad Z(z=1)=1 \quad . \tag{3.9}$$

If the coefficients of friction μ_i and μ_o as well as the radial-to axial pressure ratio α were independent of pressure and density, then for given values of a and h, equation (3.5) could be integrated to find $P(z)$. For a prescribed value of the compressibility factor β, a prescribed variation of the pre-compaction density $\eta(Z)$, and a guess for the required compaction pressure p_o, the second of equations (3.7) determines the density variation $\rho(z)$. The details $Z(z)$ of the deformation could then be found from equation (3.8) in

which the constant of integration and the unknown p_o would be determined by boundary conditions (3.9).

In fact, the coefficients of friction μ_i and μ_o as well as the radial-to axial pressure ratio α depend on pressure and density. In this more realistic case, equations (3.5), (3.7), and (3.8) must be solved simultaneously. The focus in the next two sections is on writing down plausible variations of the radial-to-axial pressure ratio and coefficients of friction with pressure and density, and then incorporating these variations into the model described above.

3.4 Dependence of Radial-to-Axial Pressure Ratio on Pressure and Density

In order to write down a plausible variation of α with P, we introduce a value α_0 of α in the loose powdered state, and note that as the density of the compact reaches its theoretical maximum value (ρ=1), the deformation becomes incompressible, the induced radial pressure equals the applied axial pressure, the axial pressure becomes unbounded, and according to equation (3.3) the parameter α must approach unity. A simple function that has these properties is given by,

$$\alpha = 1 - \frac{(1-\alpha_0)}{[1+k(\beta p_o P)^n]} \quad , \tag{3.10}$$

where k is nonnegative constant and n is a constant in the range $0<n<1$. Both k and n characterize the details of the dependence of radial to axial pressure ratio α on axial pressure P. As such, they must be chosen to match the behavior of a particular powder as

it is compacted. In the special case when $k = 0$, the radial to axial pressure ratio, α equals a constant value α_0.

Eliminating βp_o between equation (3.10) and the first equation (3.7) determines the implicit dependence of α on ρ. In this manner, we obtain

$$(1-\alpha)^{n-1}\left[(1-\alpha_0)-(1-\alpha)\right] = K_n \quad , \tag{3.11}$$

in which the quantity K_n depends on k, ρ, and η according to,

$$K_n \equiv k\left[\frac{(1-\eta)(\rho-\eta)}{\eta(1-\rho)}\right]^n \quad . \tag{3.12}$$

From the implicit dependence of α on ρ determined by equation (3.11), it can be seen that n must be restricted to the range $0<n<1$ to ensure that $\alpha=1$ as ρ approaches unity. Only when $n=1/2$ can we find the explicit dependence of α on ρ. In this special case, we find that,

$$(1-\alpha)^{1/2} = \frac{-K_n + \sqrt{K_n^2 + 4(1-\alpha_0)}}{2} \quad . \tag{3.13}$$

In Figure 3.1, we demonstrate the *general* effects of the parameters α_0, k and n on the density variations of α. Whenever one parameter is varied, the others are kept constant at $\alpha_0=.35$, $n=.6$ and $k=.1$. In all cases the apparent density η is 0.41.

As expected, increasing the initial value α_0 increases the values of α over the full range of densities. The parameters k and n alter the shape of the curves. For values of k

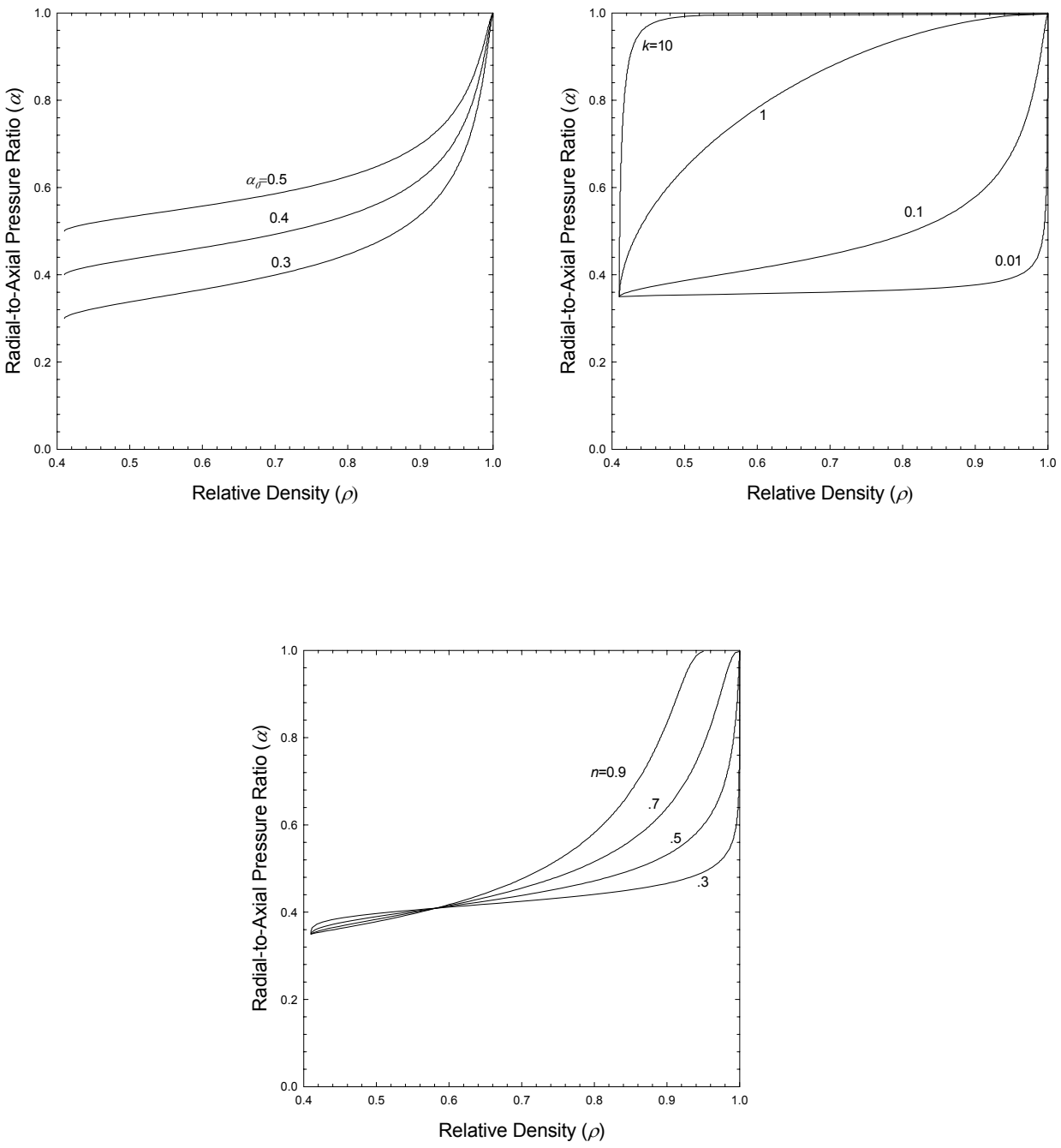

Figure 3.1: Studying the variation in α with ρ by varying the parameters n, k and α_0, one at a time and keeping others fixed, the fixed values of the parameters being given as k=.1, n=.6 and α_0=.35.

close to zero, for example, α remains close to its initial value until the density nears its maximum value. For large values of k, α rises quickly to values near unity.

In order to determine plausible values of k, n and α_0 for a particular powder, we need to fit the dependence of α on density ρ given by equation (3.11) to experimental results for a specified powder. In particular, we focus on a powder blend which is 99.5% by weight of Distalloy AE, .5% by weight of graphite, and 1% wax Hoechst micropulver admixed as internal lubricant. Distalloy AE is a diffusion alloyed iron powder with composition 4 wt% Ni, 1.5 wt% Cu, and .5 wt% Mo. Particle sizes range from 20 to 180 μm. The apparent density of the powder is 3.04 g/cm^3, and the theoretical maximum density M is 7.33g/cm^3 (so that the relative apparent density η is equal to .41). The plasticity theory for powder compaction described by Trasorras and Parameswaran [1998] indicates that the radial-to-axial pressure ratio is given by,

$$\alpha = \frac{3-b}{3+2b} \quad , \tag{3.14}$$

where b is a function of relative density ρ. By curve fitting to data obtained from triaxial consolidation experiments, Trasorras and Parameswaran [1998] have found that for the powder blend of interest,

$$b(\rho) = \frac{1}{2.8287} \ln\left[\frac{7.6 - 7.33\rho}{.2516}\right] \quad . \tag{3.15}$$

Equations (3.14) and (3.15) determine an alternative expression for the variation of pressure ratio α with relative density ρ. We can compare this variation with that fixed by

equation (3.11) to determine an appropriate set of parameters k, α_0 and n. In Figure 3.2, the dashed curve corresponds to the variation determined by Trasorras and Parameswaran [1998]. We can see that α increases monotonically from its initial (low density) value α_0 near .38. During the initial stages of densification, the gradual increase in the value of α is attributed to the rearrangement of particles. Then, due to deformation that is initially elastic but gradually becomes increasingly plastic (and incompressible) α increases to unity. The solid curve shows the fit to this dependence obtained from equation (3.11) when α_0 =.38, k=.11, n=.6.

The relation between pressure and density also can not be written down explicitly for general values of n. Instead we employ equation (3.10) to eliminate (1-α), from the first equation of state (3.7) and numerically determine the dependence function $P=P(\rho)$. In Figure 3.3, we show the variation of the relative density ρ with dimensionless pressure $\beta p_o P$, plotted for Distalloy AE powder blend described above. The dark curve shows the variation obtained using our parametric model with α_0 =.38, k=.11, n=.6. As expected, the relative density increases to unity as the pressure becomes unbounded. When the density is low, the powder is highly compressible, and the density is very sensitive to changes in pressure. When the density is high, the powder is much less compressible, and the density is much less sensitive to changes in pressure. The two dashed curves correspond to constant values α=0 and α=.75. As α increases, the material becomes less compressible, and therefore less dense at the same level of pressure. Finally, to completely characterize the powder, the factor β of compressibility must be determined. The value of β can be chosen to ensure good agreement between experimentally determined compaction loads and those predicted by our model. Trasorras et al. (1994),

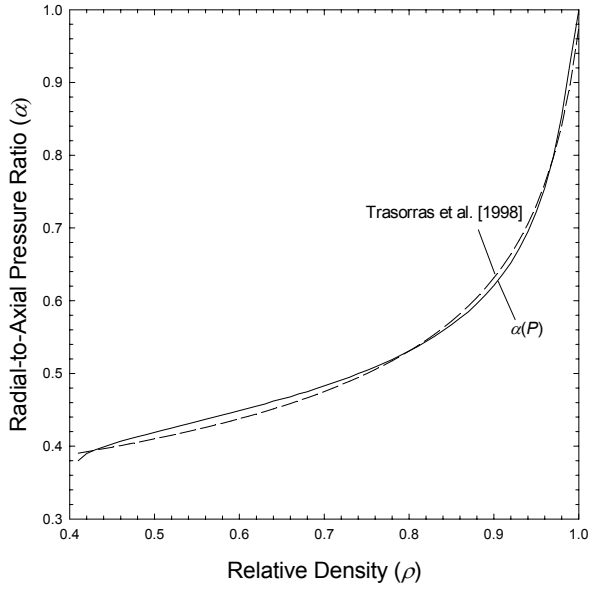

Figure 3.2: The variation of α with ρ. η=.41. The dashed line shows experimental results of Trasorras et al for Distalloy AE powder blend and the solid line shows the empirical fit obtained for the values of k=.11, n=.6, α_0=.38

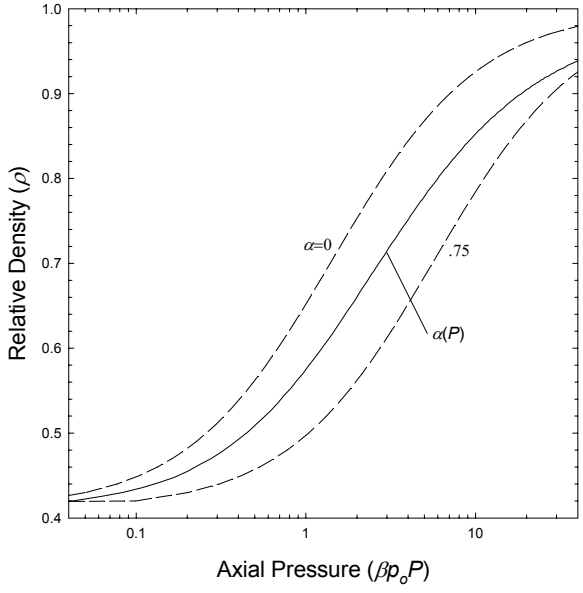

Figure 3.3: The Equation of state, variation of ρ with $\beta p_o P$, solid line shows α as a function of pressure and density k=.11, n=.6, α_0=.38 and the dashed lines indicate constant values of α=0 and .75 . η=.41.

for example, carried out single punch compaction of the Distalloy AE blend described above in a solid cylindrical die with R_o= .5 inch, H=.47 inch, L=1 inch, with reported values $\mu_i=\mu_o$=.2. The measured variation of the compaction load with punch displacement is shown by the solid data points in Figure 3.4. The solid curve is the corresponding prediction made by our model when the value β=9.75×10^{-5} in^2/lb is chosen to best match with the experimental results.

The radial-to-axial pressure ratio within the powder is related to, but not the same as, the compressibility of the powder. Both vary with density. In order to determine the direct relationship between them, we use equations (2.14) and (2.15) to identify the compressibility C as,

$$C = \beta(1-\alpha)\left[1-\frac{\rho-\eta}{1-\eta}\right] \quad . \tag{3.16}$$

It is then possible to eliminate the density between this expression and the implicit dependence of α on ρ determined by equation (3.11). Figure 3.5 shows the resulting variation of radial-to-axial pressure ratio with compressibility. As expected, we see that when $\alpha=\alpha_0$, compressibility is $\beta(1-\alpha_0)$. Then, as α increases, the compressibility decreases until (when α=1) the compressibility goes to zero.

Finally, to determine the manner in which the pressure distribution is affected by the pressure- and density-dependence of the radial-to-axial pressure ratio, we employ expression (3.10) for α in force balance (3.5) and integrate in closed form. In order to isolate the effects of variable α, we take the coefficients of friction μ_i and μ_o to be constants. The integration yields,

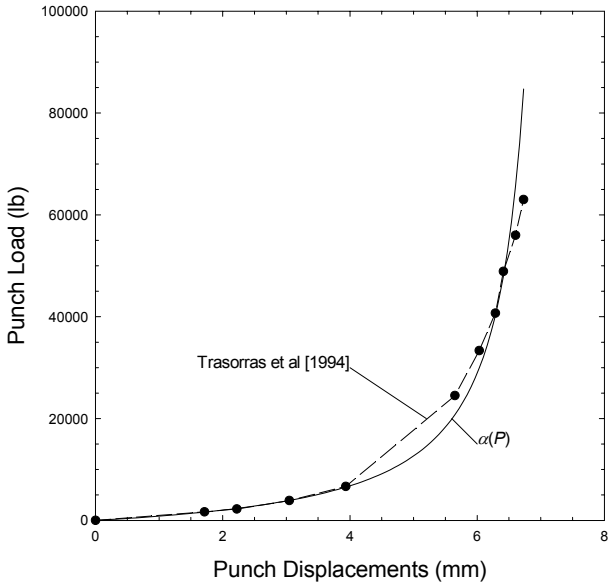

Figure 3.4: Variation of applied punch load with the displacement of the punch. The solid line indicates results from the model with α as function of pressure with k=.11, n=.6, α_0=.38 and the dots correspond to the experimental results obtained by Trasorras et al. for η=.42, L/R_o=2, $\mu_i=\mu_o$=.2, H/L=.47, L=1in

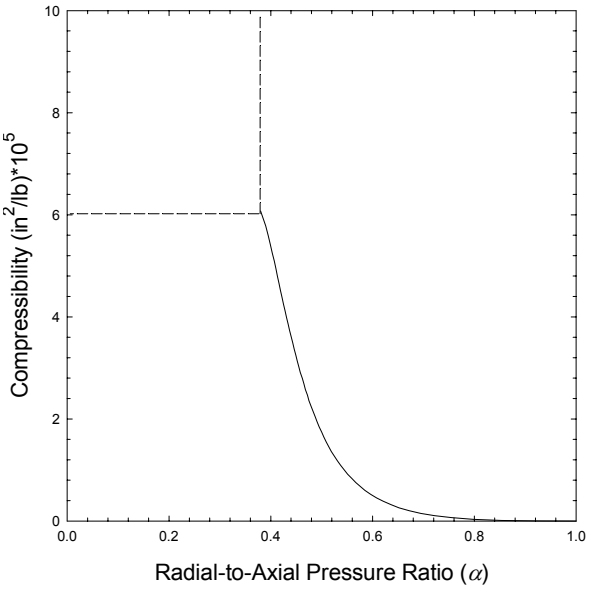

Figure 3.5: Relation between compressibility and α for Distalloy AE powder blend. α is function of pressure with k=.11, n=.6, α_0=.38

$$\frac{(\beta p_o P)^n}{[\alpha_0 + k(\beta p_o P)^n]^{1-\alpha_0}} = D\exp[(Qn(\mu_o + a\mu_i)(z-1)] \quad , \tag{3.17}$$

in which, in order to satisfy boundary condition (3.6), the constant D is,

$$D \equiv \frac{(\beta p_0)^n}{[\alpha_0 + k(\beta p_0)^n]^{1-\alpha_0}} \quad . \tag{3.18}$$

When k=0, the radial-to-axial pressure ratio is constant and equation (3.17) reduces to a simple exponential variation of P with z. In the general case when k, α_0 and n are chosen to characterize a particular powder but it is not possible to solve equation (3.17) explicitly for $\beta p_o P$ as a function of z. However, if equation (3.17) is rewritten in the form.

$$[\alpha_0 + k(\beta p_o P)^n]^{\alpha_0} - \alpha_0[\alpha_0 + k(\beta p_o P)^n]^{\alpha_0 - 1} - kDf^n(z) = 0 \quad , \tag{3.19}$$

where $f(z) \equiv \exp[(Q(\mu_o + a\mu_i)(z-1)]$, then it is clear that there are values of α_0 for which the variation $P(z)$ can be found explicitly. In particular, when α_0=1/2, equation (3.19) is quadratic with solution,

$$[(\alpha_0 + k(\beta p_o P)^n]^{1/2} = \frac{kDf^n(z) + \sqrt{k^2 D^2 f^{2n}(z) + 4\alpha_0}}{2} \quad . \tag{3.20}$$

In Figure 3.6 we show the variations of $P(z)$ given by equation (3.20) when α_0=.5, H/R_o=4, k=.11, n=.6, μ_1= μ_2=.2 for βp_o=1, 10, and 100 and 1000 As the pressures at the top of the compact increase, typical values of the pressure-dependent radial-to-axial

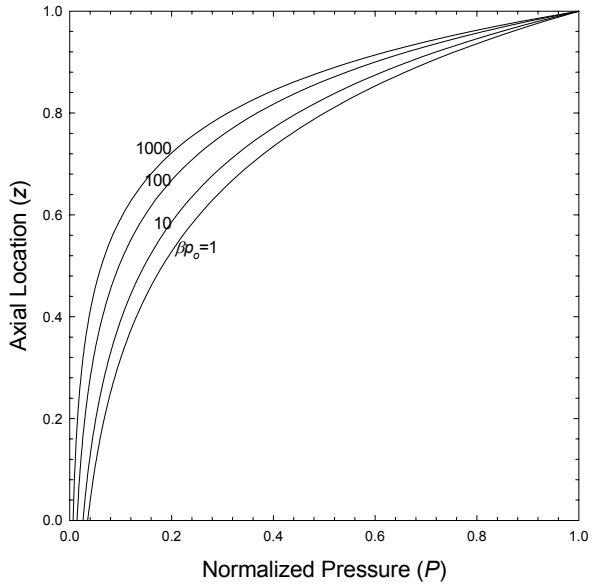

Figure 3.6: Axial Variation of Normalized Pressure *P*. for βp_o=1, 10, 100, 1000 and *h*=4.0, a=0.5, α_0=.5, *k*=.11, *n*=.6, μ_i=μ_o=.2

pressure ratio increase. This in turn increases the frictional stresses and hence yields an increase in the top-to-bottom pressure drop in the compact.

Although the solutions are not provided here, we note that when α_0=1/3 and α_0=2/3, equation (3.17) becomes cubic, and in principle can also be solved explicitly for $P(z)$.

3.5 Dependence of Friction Coefficients on Pressure and Density

In the past, several workers have investigated the relation between sliding friction and such parameters as temperature, contact resistance, and surface area that have relevance to powder metallurgy. Earlier studies of this type include those conducted by Bockstiegel et.al [1971], Mallender et.al. [1972, 1974], and Ernst et.al. [1990]. However, only recently have measurements been made that characterize the changes in the coefficient of friction during compaction as the compact evolves from loose powder to green solid. Without such a characterization, it is not possible to predict the manner in which the density distributions distort during compaction.

Here, we focus on the more recent work of Sinka et.al. [2001], who employed an instrumented die to measure the friction coefficient as it changed during the compaction of pharmaceutical powders into solid cylindrical tablets of radii R_o. They employed a computer-controlled press with linear variable differential transformers (LVDTs) that measured the height H of the compact as it decreased during compaction, load cells that measured the axial pressures p_o and $p_oP(z=0)$ at the top and bottom, and piezo-electric sensors to measure the corresponding radial pressure $p_o\sigma(z)$ at every stage. Reliable results were obtained provided that sensors were at least 20 percent of H away from the bottom of the compact and at least 30 percent of H away from the top (i.e. $.2<z<.7$)

The determination of the dependence of coefficient of friction on pressure was indirect because Sinka et. al. [2001] then used the following simple model for compaction of a solid cylinder to relate these measured quantities to the coefficient of friction at the die wall in a solid cylindrical compact (i.e. R_i=0). If the coefficients α and μ_o were constants, then equation (3.5) could be integrated to yield,

$$P(z)=\exp[(2\alpha\mu_o H/R_o)(z-1)] \quad , \tag{3.21}$$

Equation (3.21) can be re-written as,

$$\frac{P(z)}{P(z=0)}=\left[\frac{1}{P(z=0)}\right]^z \quad , \tag{3.22}$$

Solving equation (3.21) for the coefficient of friction, employing equation (3.3) to eliminate α, and using equation (3.22) to eliminate $P(z)$ from the final result, we obtain

$$\mu_o=\frac{R_o}{2H}\frac{P(z=0)}{\sigma(z)}\left[\frac{1}{P(z=0)}\right]^z \ln\left[\frac{1}{P(z=0)}\right] \quad . \tag{3.23}$$

Equation (3.23) forms the basis for the indirect measurement of μ_o, shown in Figure 3.7. According to these results, the coefficient of friction decreases dramatically with increasing radial pressure. It can be inferred, therefore, that the coefficient of friction also decreases with increasing density of the powder. This variation of μ_i=μ_o is drastic, starting (in this case) from a low density value of .9 and dropping to a high density value of .25.

Direct measurements made by Solimanjad et.al. [2001] during the compaction of a .5% lubricated iron powder yielded variations of the friction coefficient that were qualitatively similar to those obtained by Sinka et.al. [2001]. By contrast, Solimanjad et.al. [2001] employed a powder friction measuring device (PFMD) to measure the torque exerted on a flat punch in contact with rotating cylindrical specimens of controlled average densities. The die and the core rod were rotated at the same speed. With no relative motion between compact and side walls, measurements were made of the torque and pressure required to prevent the top punch from rotating with the compact. Employing a simple Coulomb law to relate the torque, pressure, and friction coefficient, these measurements yielded variations of the friction coefficient with changes in density.

Results obtained in this manner are shown in Figure 3.8 for the Distalloy AE powder blend described above.. Again we note the drastic decrease in the value of the coefficient of friction from 0.7 for the loose powder at the start of compaction to 0.3 for the compact near the end. These results are qualitatively similar to those obtained by Sinka et.al. [2001].

The experimental results of Sinka et.al. [2001] and Solimanjad et.al. [2001] indicate that the coefficient of friction decreases monotonically with increasing pressure (or density), so that it is greatest when the specimen is in its loose powdered state. As the pressure increases from zero, the coefficient of friction decreases rapidly at first, more slowly for larger pressures, and hardly at all as the pressures become extremely large. Their results fit well to the mathematical variation,

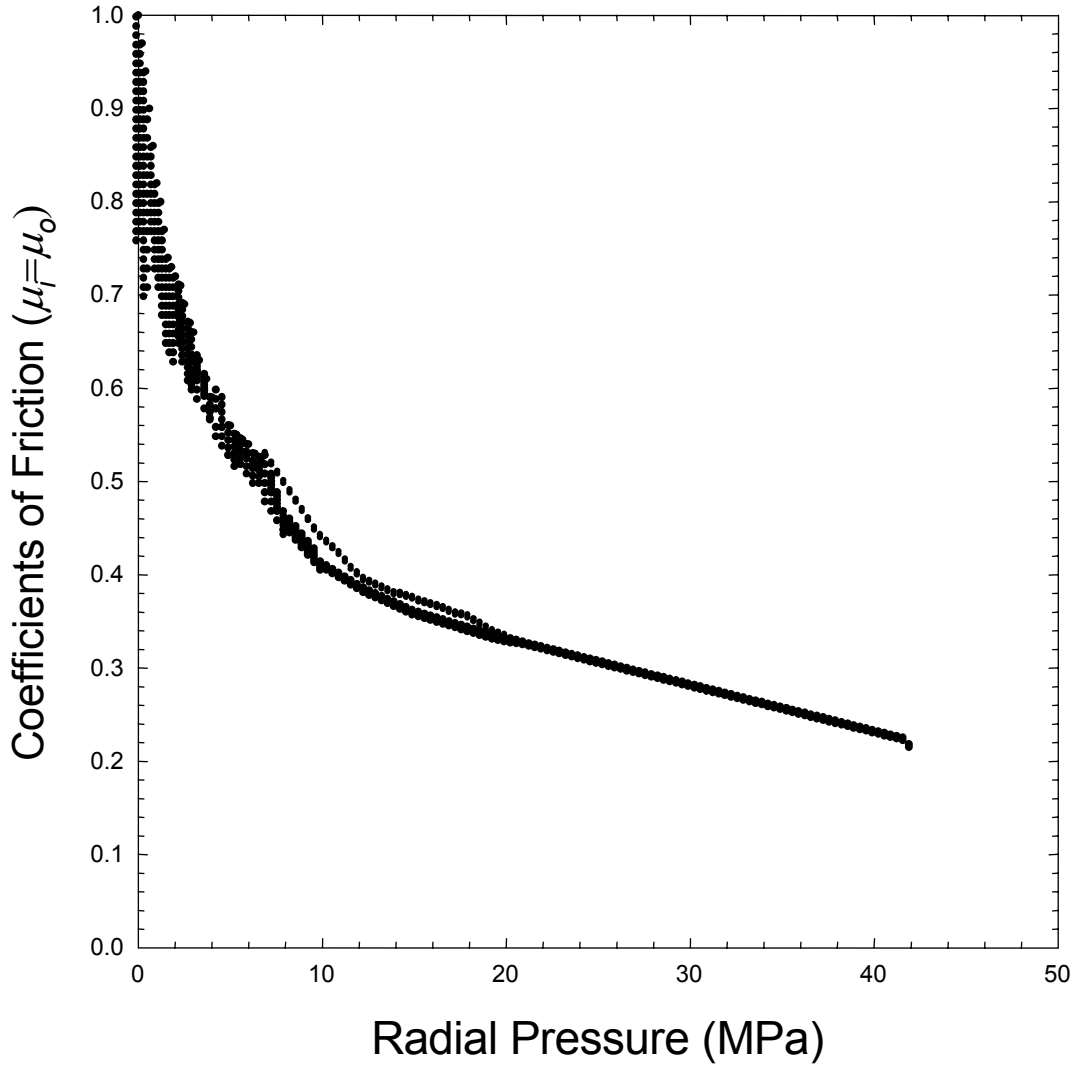

Figure 3.7: Variation of μ_i=μ_o with radial pressure in MPa for Microcrystalline cellulose powder with 1w% magnesium state, plotted experimentally by Sinka et al. (2001).

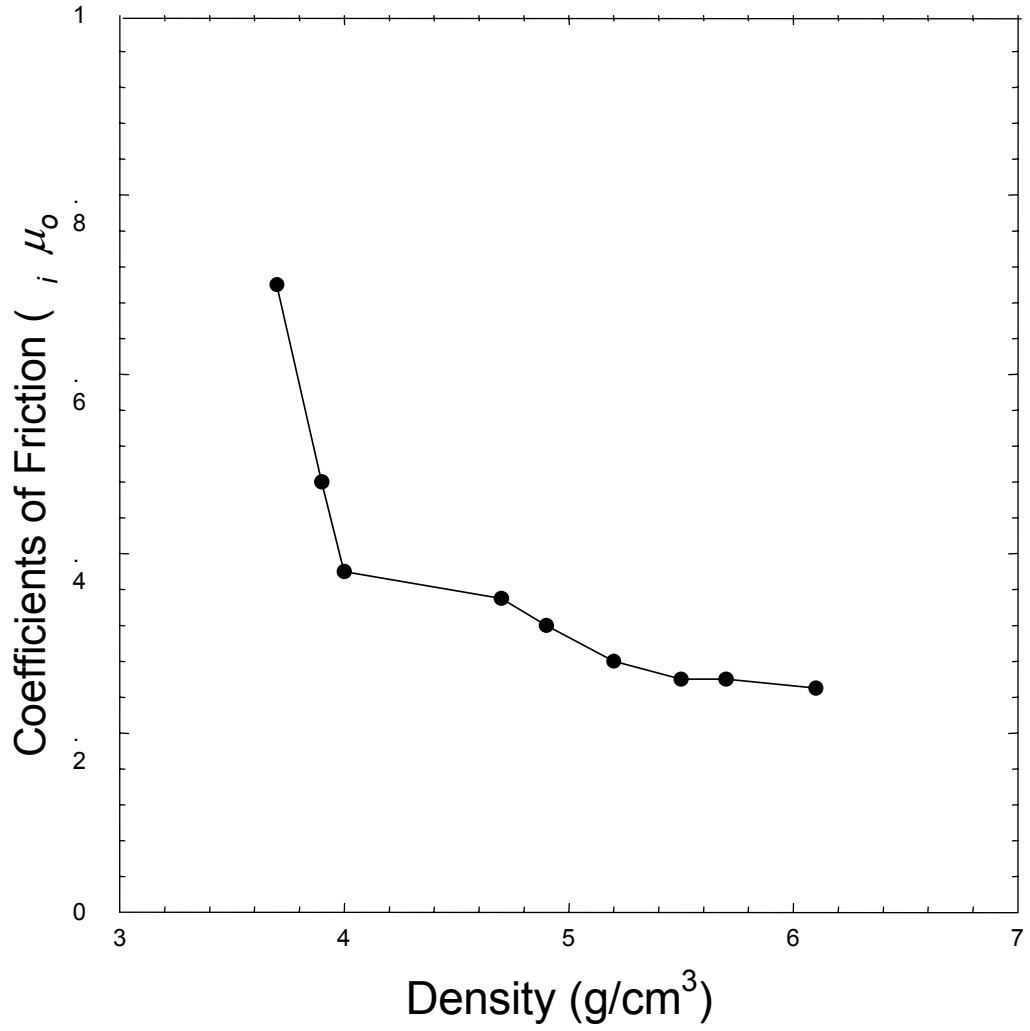

Figure 3.8: Variation of μ_i=μ_o with density in g/cm^3 for Distalloy AE powder blend comprising of .5w% lubricant, plotted experimentally by Solimanzad et al. (2001).

$$\mu_o = \frac{\mu_2 + c\mu_1 p_o P}{1 + cp_o P} \quad , \tag{3.24}$$

where μ_2 is the coefficient of friction between the die wall and the loose powder (when $P=0$), and μ_1 is the corresponding coefficient of friction when the compact is at maximum theoretical density (when P becomes unbounded). The parameter c determines the rate at which the friction coefficient varies with changes in P. Notice that when μ_2 is greater than μ_1, the rate of change of μ_o with P,

$$\frac{d\mu_o}{dP} = \frac{(\mu_1 - \mu_2)cp_o}{(1 + cp_o P)^2} \quad , \tag{3.25}$$

is always negative and that it decreases to zero with increasing P. Although there was a dependence found on punch velocity, typical values found by Solimanjad et.al. [2001] for these parameters were: μ_2=.85, μ_1=.10, and c=.14 $(\text{MPa})^{-1}$. Because the density increases with pressure, and because the first equation of state (3.7) may be used to eliminate pressure from equation (3.24), these results may also be used to infer that the coefficient of friction decreases monotonically with increasing density, and that it approaches a minimum value as the density reaches its theoretical maximum value.

The friction forces at the die wall and core rod are influenced by both the coefficients of friction there and the value of the prevailing normal pressures. The effects caused by the dependence of the friction coefficients on the pressure (and density) are not easy to isolate because the ratio α of the induced normal stress to the applied axial stress also depends on pressure. In this section, in order to avoid this complication, we present

an illustrative example that isolates the effects of pressure-dependent friction coefficients. We do so by taking α to be a constant throughout the compaction. In the sections that follow, we show numerical results in which both the radial to axial pressure ratio α and the friction coefficients μ_i and μ_o depend on density.

For simplicity, we consider the case in which the friction coefficients μ_i at the core rod, and μ_o at the die wall are equal. Provided that they vary according to equation (3.24), the pressure variations may be obtained by integrating equation (3.5) in closed form for constant values of α. In this manner, we obtain,

$$P(\mu_2 + cp_o\mu_1 P)^m = (\mu_2 + cp_o\mu_1)^m \exp[2h\alpha\mu_2(z-1)/(1-a)] \quad , \tag{3.26}$$

where the constant m is defined by $m \equiv (\mu_2 - \mu_1)/\mu_1$.. Equation (3.26) implicitly determines $P(z)$ in terms of the unknown constant p_o, which is determined by satisfying the balance of mass.

If the coefficients of friction were independent of pressure, then either $c=0$ or both $\mu_2=\mu_1$ and $m=0$. In this case, expression (3.26) for $P(z)$ would reduce to a simple exponential variation, and clearly the pressure would scale with the applied pressure p_o. For non-zero values of the friction parameter $m \equiv (\mu_2 - \mu_1)/\mu_1$, equation (3.26) demonstrates that p does not scale simply with p_o. In general, equation (3.26) can not be solved explicitly for $P(z)$. However, if the initial value μ_2 of the friction coefficient is twice the final value μ_1, then $m=1$ and equation (3.26) becomes a quadratic equation for P. Under these circumstances, the explicit expression for the axial pressure profile is,

$$P = \frac{1}{cp_o}\left[-1 + \sqrt{1 + cp_o(2 + cp_o)\exp[2h\alpha\mu_2(z-1)/(1-a)]}\right] \quad , \tag{3.27}$$

which shows clearly that the dimensional pressure normalized by the applied pressure p_o itself depends on the parameter cp_o. In order to determine the applied pressure p_o, it is necessary to employ equation (3.27) in the second equation of state (3.7), and to use the intermediate result in balance of mass (3.8). For fixed ratios $h \equiv H/R_o$ and H/L and the parameter ratio β/c that describe a particular powder, both boundary conditions (3.8) are satisfied only by the correct choice for cp_o.

To illustrate the effect of variable coefficients of friction on the pressure, we compare the profile given by equation (3.27) to the simple exponential obtained from equation (3.26) when the coefficients of friction μ_i at the core rod and μ_o at the die wall are equal constants throughout compaction (i.e.: when c=0). For the purpose of comparison, we take the friction coefficients μ_i and μ_o in the constant friction case to be equal to the average of the maximum value μ_2 and minimum value μ_1 in the variable case. When μ_2=2μ_1, this means that μ_i=μ_o=3μ_2/4. In Figure 3.9, we show as thin-lined curves the scaled pressure profiles $P(z)$ given by equation (3.27) when μ_1=.3 and μ_2=.6 and α=.5, $a \equiv R_i/R_o$=.5, and H/R_o=4.0 for cp_o=0, 1, 10, and 100. For relatively low values of p_o, the pressures are everywhere relatively low, the coefficients of friction are relatively high (i.e. near μ_2=.6), and the percent top-to-bottom pressure decreases are relatively high. For relatively high values of p_o, the pressures are relatively high, the coefficients of friction are everywhere relatively low (i.e. near μ_1=.3), and the percent top-to-bottom pressure decreases are relatively low.

In this case, then, not only do the overall pressures increase as compaction proceeds, but the shapes of the pressure profiles change as well.

By contrast, the thick solid curve in Figure 3.9 corresponds to the single profile $P(z)$ that occurs for all values of p_o when the coefficients of friction are constant ($\mu_i=\mu_o=.45$) throughout compaction. In this case, the pressures throughout the die increase in proportion to the applied pressure p_o, but the shape of the profile, and therefore the percent top-to-bottom pressure decrease, for example, remain unchanged during compaction.

An alternative expression for variation of μ_o with pressure that is qualitatively similar to one observed experimentally, is

$$\mu_o = \mu_1 + (\mu_2 - \mu_1)\exp(-\phi\beta p_o P) \quad , \tag{3.28}$$

where, as in equation (3.24), μ_2 is coefficient of friction of loose powder and μ_1 is the coefficient of friction in solid state. Here φ is a dimensionless parameter analogous to the quantity c in equation (3.24) that reflects how rapidly μ changes with P. We employ expression (3.28) when carrying out further numerical calculations.

To determine plausible values of φ , we examine the variation of coefficient of friction, given by equation (3.28). The explicit dependence of friction coefficients on density for the Distalloy AE powder is obtained by employing the first equation of state (3.7) to eliminate $\beta p_o P$ from relation (3.28), and by employing equation (3.14) to eliminate α from the intermediate result. Figure 3.10 shows the variation of coefficient of friction $\mu_i=\mu_o$ with the relative density ρ obtained in this manner, for φ=.5, 1, 5, and

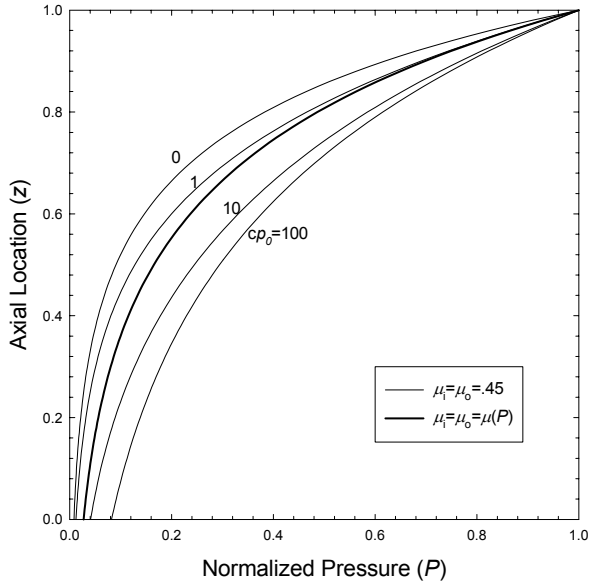

Figure 3.9: Axial profiles of P for $\mu_i=\mu_o=\mu(P)$ with $\varphi=1$ when $cp_o = 0,1,10,100$ (thin solid curves) and for $\mu_i=\mu_o=.45$ (dark solid line). Here, $\alpha=.5$, $a\equiv R_i/R_o=.5$, and $H/R_o=4.0$..

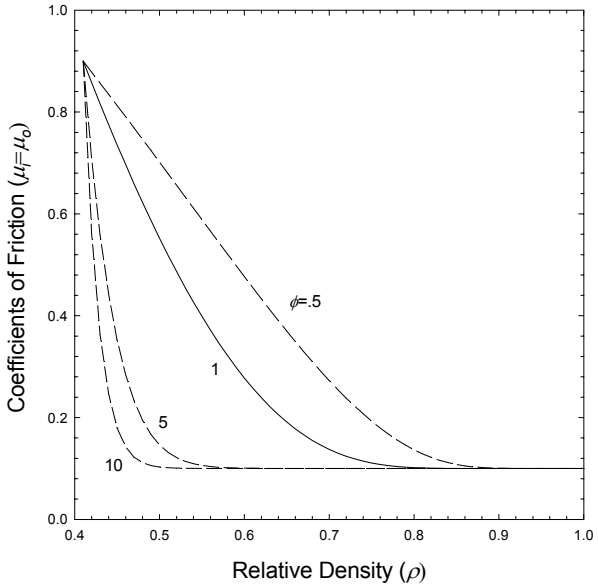

Figure 3.10: The variation of $\mu_i=\mu_o$ with relative density ρ as given by Equation (3.28) for different values of $\varphi=.5,1,5,10$. The parameters $\mu_2=.9$ and $\mu_1=.1$. From the different profiles, we select $\varphi=1$.

10. The values of the parameters μ_1=.1 and μ_2=.9 are chosen such that the variation predicted is in the range of the typical experimental results discussed above. Figure 3.10 demonstrates that qualitative behavior like that predicted by Solimanjad et.al. [2001] for metal powders may be obtained when φ in equation (3.28) is between .5 and 5. In fact, in what follows we take φ=1 as a plausible value.

3.6 Solution Procedure

Finally, it remains to calculate the manner in which the axial pressure and density profiles evolve during compaction when both the friction coefficients (μ_i and μ_o) and the radial-to-axial pressure ratio (α) vary with pressure and density. Force balance (3.5) for the pressure is complicated by the fact that α depends explicitly on P or ρ. In fact, ρ can be determined directly as follows. The first equation of state (3.7) gives $P=P[\rho,\alpha(P \text{ or } \rho),\eta(Z)]$. If α depends explicitly on ρ, the axial gradient of the pressure can be expressed in terms of the density and its axial gradient as follows:

$$\frac{dP}{dz}=\left(\frac{\partial P}{\partial \rho}+\frac{\partial P}{\partial \alpha}\frac{d\alpha}{d\rho}\right)\frac{d\rho}{dz}+\frac{\partial P}{\partial \eta}\frac{d\eta}{dZ}\frac{dZ}{dz} \quad . \tag{3.29}$$

If α depends explicitly on P, then the axial gradient of P can be determined from

$$\left[1-\frac{\partial P}{\partial \alpha}\frac{d\alpha}{dP}\right]\frac{dP}{dz}=\frac{\partial P}{\partial \eta}\frac{d\eta}{dZ}\frac{dZ}{dz}+\frac{\partial P}{\partial \rho}\frac{d\rho}{dz} \tag{3.30}$$

where the first equation (3.7) can be used to calculate the derivatives of P with respect to ρ, α, and η. By including the term involving $d\eta/dZ$, we have accounted for the

possibility that the initial fill density η may be non-uniform. When α depends explicitly on ρ, force balance (3.5) becomes,

$$\frac{d\rho}{dz} = \left[\frac{\partial P}{\partial \rho} + \frac{\partial P}{\partial \alpha}\frac{d\alpha}{d\rho}\right]^{-1}\left\{Q\alpha(\mu_o + a\mu_i)P - \frac{H}{L}\frac{\rho}{\eta}\frac{\partial P}{\partial \eta}\frac{d\eta}{dZ}\right\} \quad , \tag{3.31}$$

where $P[\rho,\alpha(\rho),\eta(Z)]$ is given by equation (3.7), $\mu_o\{P[\rho,\alpha(\rho),\eta(Z)]\}$ is given by equation (3.28), $\mu_i\{P[\rho,\alpha(\rho),\eta(Z)]\}$ is given by an equation analogous to (3.28), and for the Distalloy AE powder described in section 3.4, $\alpha(\rho)$ is given by equation (3.14) and (3.15). Note that we have used equation (3.8) to eliminate dZ/dz from equation (3.30) to obtain (3.31).

Similarly, if α depends explicitly on P, then

$$\frac{d\rho}{dz} = \left(\frac{\partial P}{\partial \rho}\right)^{-1}\left[Q\alpha(\mu_o + a\mu_i)P\left(1 - \frac{\partial P}{\partial \alpha}\frac{d\alpha}{dP}\right) - \frac{H\rho}{L\eta}\frac{\partial P}{\partial \eta}\frac{d\eta}{dZ}\right] \tag{3.32}$$

where, for example, a plausible form of $\alpha(P)$ is given by equation (3.10). Here, we have used equation (3.8) to eliminate dZ/dz from equation (3.30) to obtain equation (3.32).

Numerical integration of equations (3.8) and (3.31) or (3.32) may be carried out simultaneously to determine $\rho(z)$ and $Z(z)$. If, for example, integrations are initiated at the top of the compact, then we employ the second of boundary conditions (3.9), guess at the value $\rho(z=1)$, and iterate on our guess until the first of boundary conditions (3.9) is satisfied at $z=0$. With $\rho(z)$ and $Z(z)$completely determined in this manner, the quantity βp_o is determined by the first equation of state (3.7) at $z=1$ and subjected to condition (3.6), and the pressure variation $P(z)$ for all other values of z is fixed by the first equation

(3.7). With $Z(z)$ known, the net downward displacement $u(z)$ of any particle in the compact is simply equal to the difference $Z(z)$-z of its initial and final locations.

If the initial fill density is uniform, then η does not depend on Z, and integration of equations (3.8) and either (3.31) or (3.32) need not be done simultaneously. In this case, we guess at the value $\rho(z=1)$, integrate equation (3.31) or (3.32) alone to get $\rho(z)$, use this result to integrate equation (3.8), and iterate on $\rho(z=1)$ until both boundary conditions (3.9) can be satisfied.

3.7 Results and Discussion

In this section we present the results obtained in the manner described above. In all that follows, unless otherwise specified, we use the powder properties of the powder blend comprising of 99.5% Distalloy AE, 0.5% Graphite and 1% Wax Hoechst Lubricant. This allows us to compare our results with the available experimental results for the same powder. Its apparent density is 3.04 g/cm^3, its maximum theoretical density is 7.33 g/cm^3, and, its relative apparent density η is therefore 0.41. The radial-to-axial pressure ratio α, as a function of density ρ, for this powder blend is given by either by equations (3.14) and (3.15) or by equation (3.10) with k=.11, n=.6, α_0=.38. In all cases, we take the coefficients of friction μ_i and μ_o at the core rod and die wall to be equal.

In presenting the results, we first take the coefficients of friction to be constant throughout compaction, and consider only the effects introduced when the radial-to-axial pressure ratio α depends on pressure. In the Figure 3.11, we take μ_i=μ_o=.2, a≡R_i/R_o=.5, and L/R_o=10, and show as solid curves the axial variations of the density ρ when α varies with pressure. The solid curves show how the relative density profiles evolve (from an

initially uniform density distribution) at different stages (H/L=1, .9, .8, .7, .6, 5, and .45) of compaction. As the compaction proceeds, the difference between the top and bottom densities increases to a maximum at approximately H/L=0.7. Beyond H/L=0.7 the density difference decreases. This is because regions of higher density are less compressible than regions of lower density. In the final stage of compaction, ρ varies from .962 at the top to .836 at the bottom.

We also show in Figure 3.11 a set of corresponding dashed curves that are generated with an appropriate constant value of α. For uniform apparent density η=.41, the average density at the end stage of compaction H/L=.45 is equal to 0.911. From Fig.3.2, the value of α corresponding to a density of .911 is α =0.66. The variations predicted by using constant value of α are qualitatively similar to but quantitatively different from those obtained using varying α. The variations of density computed based on the constant value of α are greater than those based on the constant value. This is because constant value of α is typically greater than the variable values, which in turn yields higher radial pressures σ, higher frictional forces, and greater axial pressure variations. Since, we have taken constant value of α appropriate to the last stage of compaction, the variations shown by the solid and dashed curves match increasingly well as the final stage is stage approached. In fact, at the final stage (H/L=.45) the value of α varies around the constant value of .66. These relatively minor variations are entirely responsible for the differences in the solid and dashed density profiles at the end of compaction.

Fig 3.12 shows how the percent top-to-bottom density decrease varies with the compaction height H/L, for the cases presented in Figure 3.11. The solid line

corresponds to the predictions based on varying α, and the dashed line corresponds to those based on α=.66 throughout compaction. At the start of compaction, the densities are uniform and the difference between the top and bottom densities is zero. As the compaction proceeds, wall friction creates increasing top-to-bottom pressure differences. Initially these differences serve to increase the top-to-bottom density differences. But at some point (at about H/L= .7 in this case), these differences begin to decrease because the compressibility of the powder reduces to a greater extent in regions of higher density. In this case, the solid curve demonstrates that the maximum top-to-bottom density decrease is equal to 36.2 percent at about H/L=.7, and the final value reduces to 13.4 percent at H/L=.45. The corresponding dashed curve (for α=.66) are qualitatively similar, with density differences that are typically greater than those predicted by the solid curve as explained above (Figure 3.11). In this case, the maximum top-to-bottom density decrease is equal to 46 percent at about H/L= .7, and the final value reduces to 17.7 percent at H/L=.45.

We now focus attention on cases in which *both* the coefficients of friction $\mu_i=\mu_o\equiv\mu$ *and* the radial-to-axial pressure ratio α vary with density and pressure. Equation (3.28) describes the variation of $\mu_i=\mu_o$ with pressure. Based on observations made in section 3.5, we take the low density value of μ to be μ_2=.9, the high density value to be μ_1=.1 and the parameter φ that measures the sensitivity of friction coefficient to changes in pressure to be φ=1. The variation of α with pressure is given by equation (3.10) with k=.11, n=.6, α_0=.38.

In Fig. 3.13, we show as solid curves the axial variations of relative density ρ and non-dimensional pressure $\beta p_o P$ at H/L =.9, when the initial density distribution is uniform

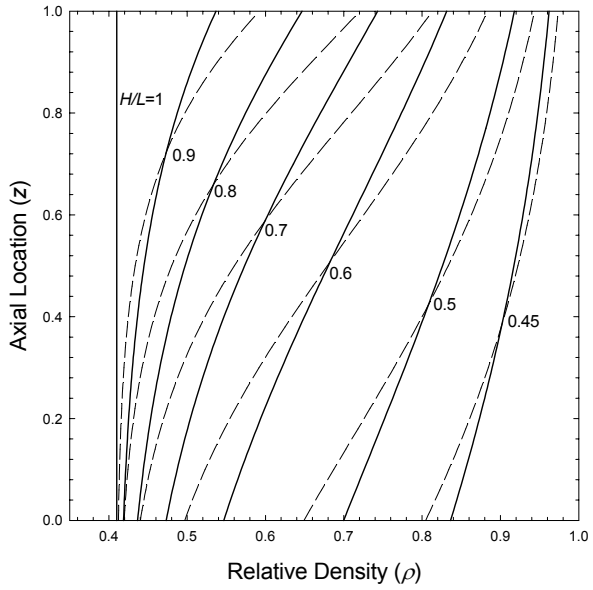

Figure 3.11: The variation of ρ with z, for H/L=1, .9, .8, .7, .6, .5 and .45. The solid lines indicate results from the model with α as function of pressure with k=.11, n=.6, α_0=.38 and the dashed lines correspond to constant value of α =.66 for uniform initial density η=.41, a=.5, L/R_o=10, μ_i=μ_o=.2.

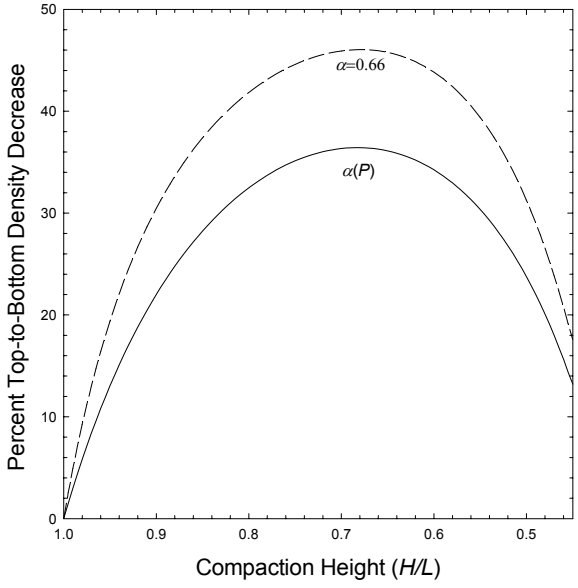

Figure 3.12: Variation of δ_z with H/L. The solid line indicates results from the model with α as function of pressure with k=.11, n=.6, α_0=.38 and the dashed lines correspond to constant value of α =.66 for uniform initial density distribution η=.41, a=.5, L/R_o=10, μ_i=μ_o=.2.

at η =.41 and when the compact geometry is described by a=.5, L/R_o=8. For the purpose of comparison, we also show (as dashed curves) two corresponding variations predicted when $\mu \equiv \mu_f$=.1 and $\mu \equiv \mu_{avg}$=.302 remain unchanged throughout compaction. The value $\mu \equiv \mu_f$=.1 is simply the high density value μ_1. The value $\mu \equiv \mu_{avg}$=.302 is the value (taken from Figure 3.10) corresponding to the mean relative density .615 between the initial average density .41 (at H/L=1) and the final average density .82 (at H/L=.5). The value .615 is the average relative density when H/L=2/3. In Figures 3.14 and 3.15, we show the corresponding density and pressure profiles at H/L=2/3 and .5.

At the earliest stage of compaction, the coefficient of friction $\mu(P)$ is still near μ_2=.9, so that the density variations are much greater than those for $\mu_i=\mu_o=\mu_{avg}$=.302 and $\mu_i=\mu_o$=.1. As H/L and $\mu(P)$ decrease, the differences between the details of the profiles for the variable coefficient of friction and the minimum coefficient of friction diminish until they are virtually indistinguishable at H/L=.5. Interestingly, at no stage of compaction do the variable friction coefficient $\mu(P)$ and average friction coefficient μ_{avg} profiles become indistinguishable. Even at H/L=2/3=.667, when the average relative density in the compact is equal to .615, the large spatial variations in pressure at that instant yield differences between profile generated based on a uniform coefficient of friction appropriate to the average density and a corresponding profile based on friction coefficients that depend on pressure.

In Figure 3.16, we show how the percent top-to-bottom density variations evolve during compaction as H/L decreases from 1 at the start of compaction to .5 at the end, when $\mu_i=\mu_o$ is the function $\mu(P)$ of pressure given by equation (3.28). Interestingly, the nonuniformity induced in the density distribution increases to a maximum (42 percent) at

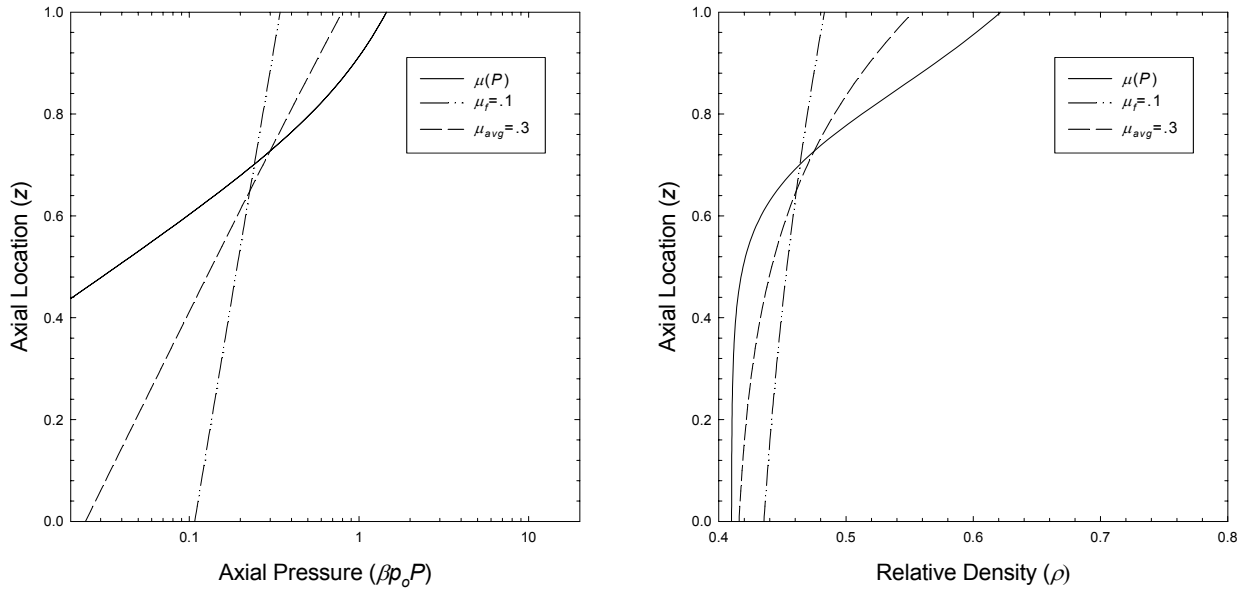

Figure 3.13: The variation of $\beta p_o P$ and ρ with z for H/L=.9 for three different cases of μ. α .is function of pressure with k=.11, n=.6, α_0=.38 and density distribution is initially uniform with η=.41, a=.5, L/R_o=8

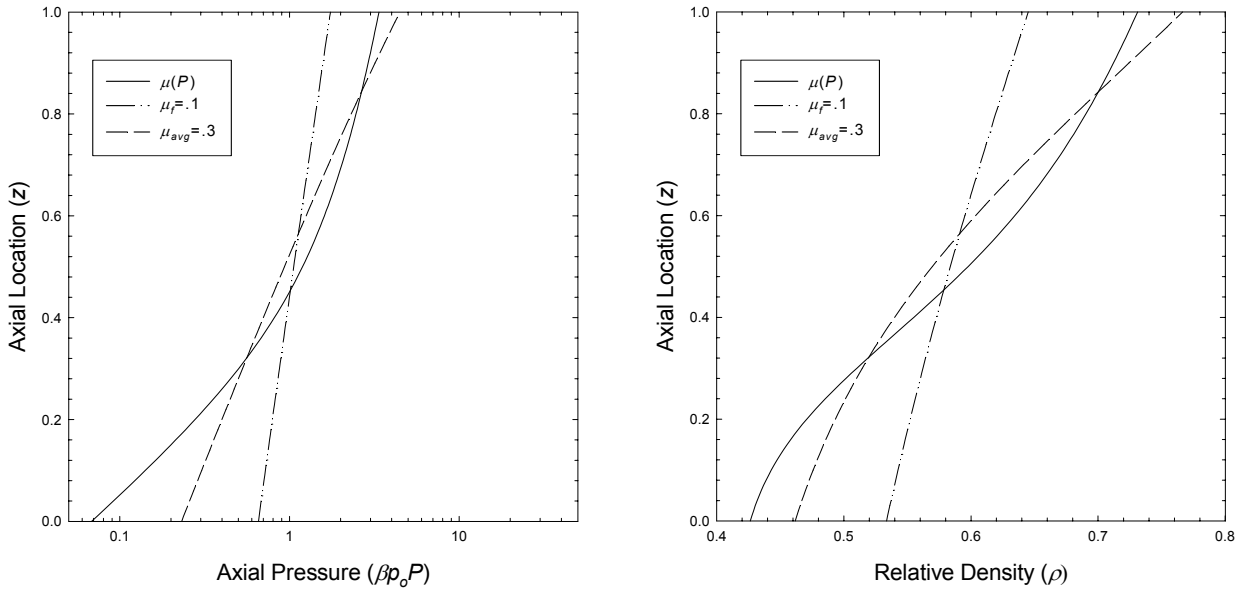

Figure 3.14: The variation of $\beta p_o P$ and ρ with z for H/L=.667 for three different cases of μ. α .is function of pressure with k=.11, n=.6, α_0=.38 and density distribution is initially uniform with η=.41, a=.5, L/R_o=8

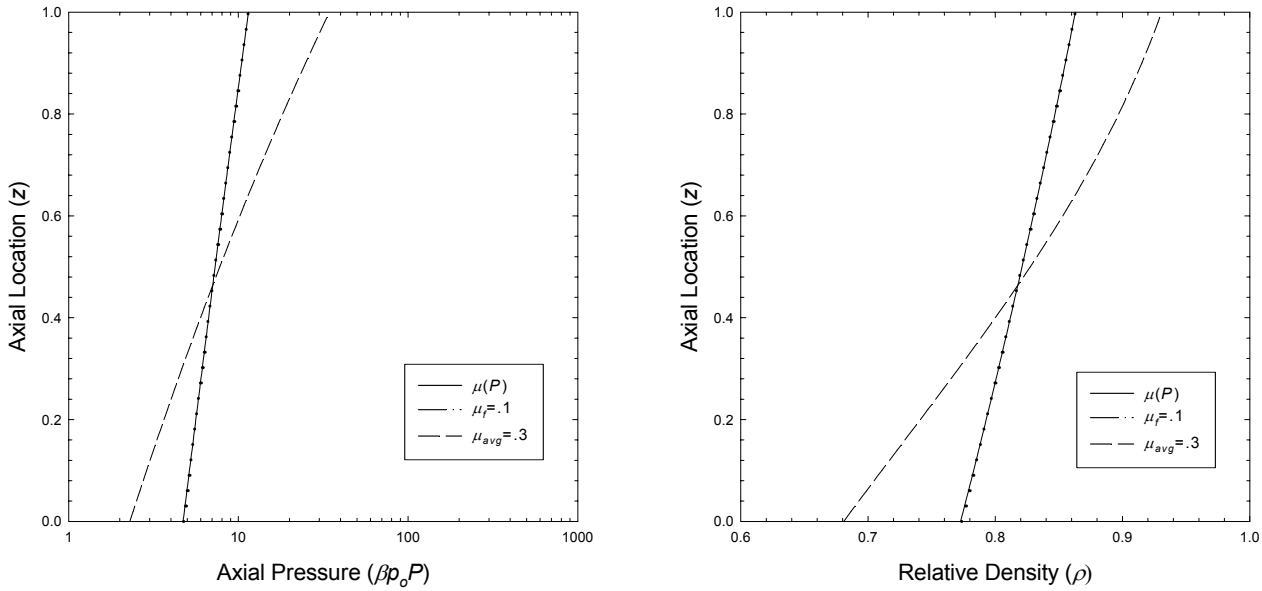

Figure 3.15: The variation of $\beta p_o P$ and ρ with z for H/L=.5 for three different cases of μ. α .is function of pressure with k=.11, n=.6, α_0=.38 and density distribution is initially uniform with η=.41, a=.5, L/R_o=8

an intermediate height of H/L=.72 that is approximately four times the nonuniformity (10.3 percent) that is present in the final green compact. The increase in nonuniformity that occurs in the early stages of compaction is due to the fact that (according to the equation of state (3.7)) even small top-to-bottom pressure differences give rise to fairly large density differences when the magnitudes of the pressures are low. The decrease in nonuniformity that occurs in the later stages of compaction is due to two effects. First, even if the coefficients of friction were constant throughout the compaction, the equation of state demonstrates that even large top-to-bottom pressure differences give rise to only small density differences when the magnitudes of the pressures are high. Second, the coefficient of friction, and therefore the percent top-to-bottom pressure variations diminish as compaction proceeds.

For the purpose of comparison, we have also shown on Figure 3.16 the corresponding variations of top-to-bottom density decrease when the coefficients of friction $\mu_i=\mu_o$ are taken to be constants. Just as in Figures 3.13, 3.14, and 3.15, in one comparison, we take $\mu_i=\mu_o$ equal to the high density value μ_1=.1, and in the other we take $\mu_i=\mu_o$ equal to an average value μ_{avg}=.302, which (from equations (3.14), (3.7), and (3.15)) is appropriate to the average relative density (ρ=.615) between .41 at the start of compaction and .82 at the end. As expected, the nonuniformities predicted for minimum coefficients of friction are typically smaller than those predicted as the friction coefficients decrease to their minimum values, and the predictions approach one another as compaction concludes. The nonuniformities predicted by the $\mu_i=\mu_o=\mu_{avg}$=.302 curve, on the other hand, are smaller than those predicted by the $\mu_i=\mu_o=\mu(P)$ curve in the early stages of compaction when μ_{avg} is less than $\mu(P)$, are larger than those on the $\mu_i=\mu_o=\mu(P)$

curve in the later stages of compaction when μ_{avg} is greater than $\mu(P)$, and agree well near the instant (H/L=2/3) at which μ_{avg}. is equal $\mu(P)$.

In Figure 3.17, we show the variation of the applied pressure βp_o during compaction for the three cases considered in Figures 3.13 through 3.16. In the earliest stages of compaction, the predictions based on pressure-dependent friction coefficients yield the largest required compaction pressures because the friction coefficients are highest in this case. There is a cross-over between the compaction loads predicted by the variable friction model and the μ_{avg}-model, because at the final stages of compaction the μ_{avg}-model employs the largest friction coefficients and therefore predicts the largest required pressures. The gradual approach and eventual coincidence of the compaction loads predicted by the variable friction model and those predicted by the minimum friction model is in every way consistent with the observations made concerning the profiles of pressure and density shown in Figure 3.13, 3.14, and 3.15.

The differences in predicted compaction loads for differing friction models suggest that a significant fraction of the total load must be devoted to overcoming the frictional forces exerted at the die wall and core rod. To isolate this phenomenon, in Figure 3.18 we calculate the fraction of the total load that is exerted to overcome friction, and show how it varies during compaction in the three cases ($\mu_i=\mu_o=\mu(P)$, $\mu_i=\mu_o=\mu_{avg}$, and $\mu_i=\mu_o=\mu_f$) of interest here. The portion of the load that is devoted to friction is essentially the difference between the pressure at the top of the compact and the pressure at the bottom. Figure 3.18 demonstrates that in all cases the fraction of the load devoted to overcoming friction decreases as the compaction proceeds. In the case of constant friction coefficients (μ_{avg} and μ_f), this is because the specimen becomes less compressible

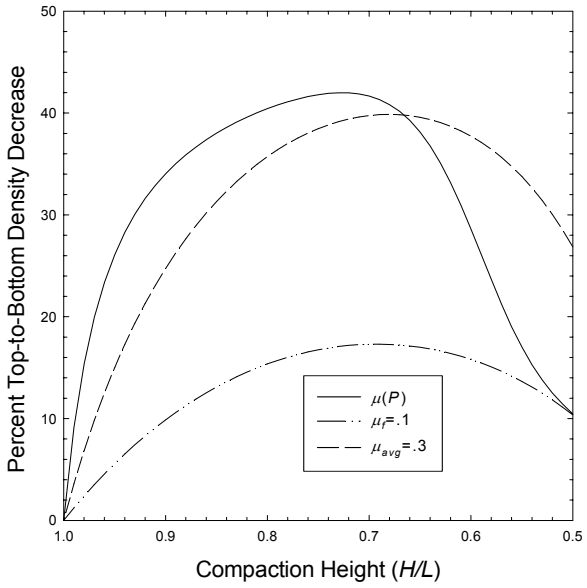

Figure 3.16: The variation of δ_z with H/L for three different cases of μ. α is function of pressure with k=.11, n=.6, α_0=.38 and density distribution is initially uniform with η=.41, a=.5, L/R_o=8

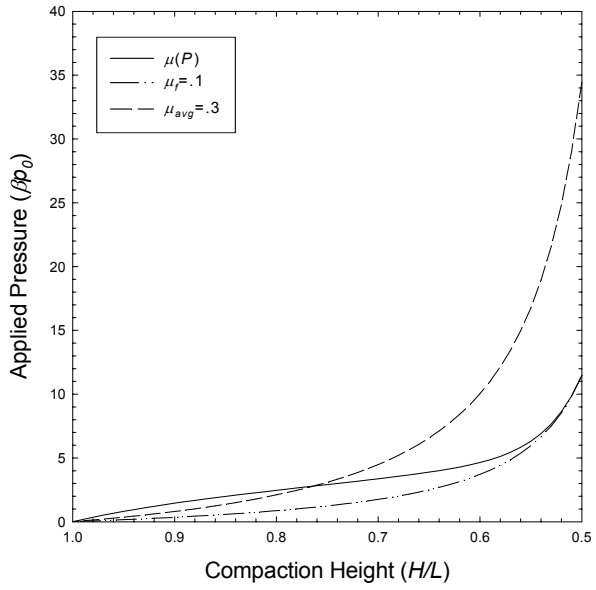

Figure 3.17: The variation of βp_0 with H/L for three different cases of μ. α is function of pressure with k=.11, n=.6, α_0=.38 and density distribution is initially uniform with η=.41, a=.5, L/R_o=8

and requires a larger fraction of the load to overcome the specimen's inherent resistance to axial contraction. In the case of variable friction ($\mu(P)$) this effect is present, but it is overwhelmed by a larger effect due to the drastic reduction in friction coefficient from μ_2=.9 to μ_1=.1.

The model employed here is based on the assumptions that the compact is comprised of many thin flat discs that remain flat during compaction. If all these thin discs were compacted by equal amounts, then uniform density distribution would result and a plot of the axial location z versus the downward displacement u will be linear. However, Figures 3.13, 3.14, and 3.15, for example, demonstrate that the degree of compaction near the top of the compact is more than it is near the bottom. Consequently, the plot of axial location versus axial displacement will be nonlinear. Figure 3.19 shows one such plot. The solid lines correspond to the displacements during actual compaction, whereas the dashed lines show the displacements that would occur if the density remained uniform throughout compaction. A comparison between any of the solid curves and its dashed counterparts provides an alternative measure of compact nonuniformity.

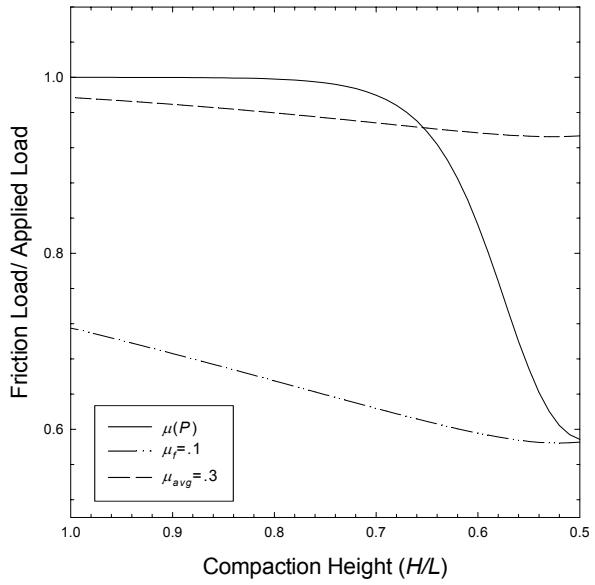

Figure 3.18: The variation of fraction of the applied load with H/L for three different cases of μ. α.is function of pressure with k=.11, n=.6, α_0=.38 and density distribution is initially uniform with η=.41, a=.5, L/R_o=8

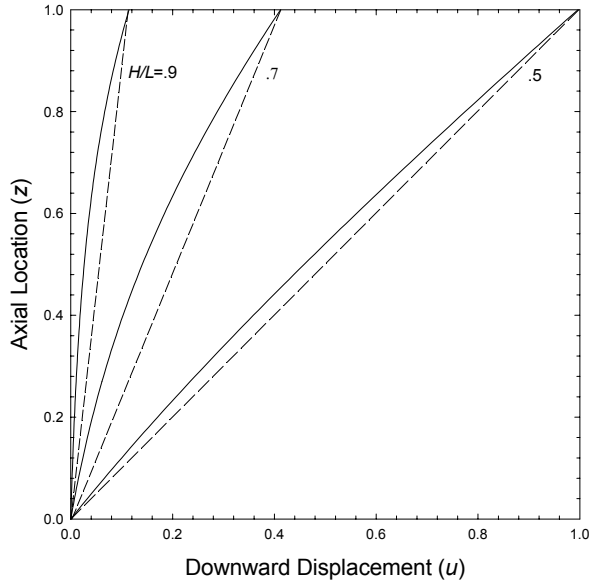

Figure 3.19: The variation of u with z for H/L=.9, .7, .5, coefficient of friction as a function of P with μ_2=.8, μ_1=.078, φ=1, α.is function of pressure with k=.11, n=.6, α_0=.38 and density distribution is initially uniform with η=.41, a=.5, L/R_o=8

CHAPTER 4

Modeling Springback and Ejection of Hollow Cylindrical Compacts

4.1 Introduction

In this chapter, we present a simple model for the spring back of the die wall and core rod that occurs after compaction, and the ejection process required to remove compact from its containing die. As in our previous work, we focus on bushing-like compacts, and we employ a compaction analysis that accounts for the evolution of the coefficients of friction and the radial-to-axial pressure ratio during compaction. In fact, the results obtained from the compaction model of Chapter 3, serve as the starting point for the calculations concerning spring back and ejection. By comparing ejection force predictions made by the model to those determined experimentally, we indirectly can evaluate the accuracy of the compaction model already described.

We first present a simple analysis of spring back, in which we employ the pressures calculated during compaction to calculate the corresponding radial pressures and frictional stresses exerted by the die wall and core rod on the compact after the axial compaction load is removed.

Next, we present an analysis of the compression that occurs during ejection. In this phase, because there is a resistance to sliding due to the frictional stresses that result from spring back, the compact is further compressed. Associated with this compression is a Poisson tendency to expand radially, and a substantial increase in both the radial pressures and frictional stresses exerted by the die wall and core rod on the compact. Because the increase is substantial, the ejection forces predicted by the complete analysis

are much higher than those that would be obtained based on the frictional stresses due to spring back alone.

Finally, we present a survey of results that is focused primarily on understanding the contributing factors that impede ejection. In particular, we focus on the individual contributions to the radial pressures that develop between the die wall and the compact, and between the core rod and the compact. These radial pressures in turn give rise to the frictional stresses that must be overcome during ejection.

4.2 Compaction Analysis

As in Chapters 2 and 3, the geometry of the compact (shown in Figure 2.1) is described by the following dimensionless quantities: the radii ratio $a \equiv R_i/R_o$; the height ratio H/L, and the aspect ratio $h \equiv H/R_o$. For axi-symmetric compaction with little radial variations in pressure and density, the one dimensional (axial) model developed in Chapter 3 is sufficient. The coordinate $Z \equiv Z^*/L$ measures axial position of any point before compaction, and $z \equiv z^*/H$ measures axial position at any instant during compaction. The dimensionless pressure P is the average axial pressure at any axial location z, nondimensionalized by the external pressure p_o applied at the top of the compact. The dimensionless pressure Σ is the average radial pressure at any location z, nondimensionalized by the external pressure p_o. The aim of the compaction analysis of Chapter 3 is to determine the axial variations of the density $\rho(z)$, the pressures $P(z)$, and $\Sigma(z)$, and the deformation $Z(z)$ just after compaction is completed but just before the axial load from the punch has been removed. As described in section 3.6, the functions $\rho(z)$, $P(z)$, and $Z(z)$, and the quantity p_o are determined by equation (3.8) and boundary

conditions (3.9), equation (3.32), and the first of equation (3.7) with boundary condition (3.6). In carrying out the solution procedure described in section 3.6, we employ equation (3.10) (with the parameters α_o=.38, k=.11, and n=.6) for the pressure variation of the radial-to-axial pressure ratio $\alpha(P)$, and equation (3.28) (with the parameter ϕ=1) for the pressure variation of the coefficients of friction $\mu_i(P)= \mu_o(P)$.

Once the pressure distribution $P(z)$ are determined, the radial pressure $\Sigma(z)$ may be computed according to the averaged form of constitutive relation (3.3):

$$\Sigma(z) = \alpha P(z) \quad , \tag{4.1}$$

where $\alpha(P)$ is given by equation (3.10). The radial pressure $\Sigma(z)$ serves as input into the springback/ejection model.

4.3 Springback

For the compact of interest shown in Figure 2.1, *before compaction* the radius of the solid core rod is R_i, the inside radius of the die wall is R_o, and the outside radius of the die wall (not shown in Figure 2.1) is R. Just as compaction concludes, *but before the compaction load is released*, the radial pressure $\Sigma(z)$ applied to the inside surface of the die wall and the outside surface of the core rod is given according to equation (4.1) computed in the manner described in the previous section. As a result of the presence of the radial pressure, the inside surface of the die wall displaces radially outward, and the outside surface of the core rod displaces radially inward. These displacements can be estimated by assuming that at any axial location z, the core rod and die deform elastically as a collection of independent disks. At any axial location, the die is taken to be a hollow

disk (of inside radius R_o and outside radius R) subjected to internal pressure $\Sigma(z)$, and the core rod is taken to be a solid disk (of radius R_i) subjected to external pressure $\Sigma(z)$. In what follows, the die wall has a Young' modulus E_D and a Poisson's ratio ν_D, and the corresponding values for the core rod are E_R and ν_R, respectively.

Employing standard elasticity solutions for these problems (see, for example, Boresi and Chung [2000]), we find that just before the compaction load is released, the radial displacement $U_o(z)$ of the inner surface of die is given by:

$$\frac{U_o(z)}{R_o} = \left(\frac{[p_o \Sigma(z)/E_D)}{(R/R_o)} \right) \left(\frac{(R/R_o)^2}{(R/R_o)^2 - 1} \right) \left[\frac{(1-\nu_D)}{(R/R_o)} + (1+\nu_D)\left(R/R_o\right) \right] \quad , \quad (4.2)$$

while the radial displacement $U_i(z)$ of the outer surface of the core rod is given by:

$$\frac{U_i(z)}{R_o} = -(1-\nu_R) \left(\frac{p_o \Sigma(z)}{E_R} \right) \left(\frac{R_i}{R_o} \right) \quad . \quad (4.3)$$

The negative sign in equation (4.3) indicates inward displacement. Both $U_o(z)$ and $U_i(z)$ are completely determined once the radial pressure, $\Sigma(z)$, is calculated from compaction. In the compaction analysis described in the previous section, the core rod and die wall were assumed to be rigid, and consequently the displacements $U_o(z)$ and $U_i(z)$ were ignored in computing the green density distributions. As it will be seen, these displacements will have a negligible effect in on density distributions during compaction, but will give rise to large radial pressures and friction forces during compaction.

Because of the removal of the compaction pressure, both the die and core rod spring back elastically. Consequently, after the compaction is completed and just before

the ejection begins, the radial displacements at the die wall and the outer surface of the core rod, are actually much smaller than the displacements given by equations (4.2) and (4.3). The die (of inside radius R_o and outside radius R), the compact (of inside radius R_i+U_i and outside radius R_o+U_o, respectively), and the solid core rod (of radius R_i) are three cylinders pressurized together by their misfit. The mismatches $U_o(z)$ and $U_i(z)$ are given by equations (4.2) and (4.3),

After the spring back, the *net* radial displacements of the inner surface of the die wall, the outer surface of the compact, the inner surface of the compact, and the outer surface of the core rod are denoted by $V_{oD}(z)$, $V_{oC}(z)$, $V_{iC}(z)$, and $V_{iR}(z)$, respectively. Compatibility requires that after springback, the inside radius R_o+V_{oD} of the die and the outside radius $R_o+U_o+V_{oC}$ of the compact be equal. Thus,

$$V_{oD} - V_{oC} = U_o \qquad . \qquad . \qquad (4.4)$$

Similarly, after springback, the radius R_i+V_{iR} of the core rod, and the inside radius $R_i+U_i+V_{iC}$ of the compact must be equal. Therefore,

$$V_{iR} - V_{iC} = U_i \qquad . \qquad . \qquad (4.5)$$

Of greatest interest here are the radial pressures ($\Sigma_o(z)$ between the inner surface of the die and the outer surface of the compact, as well as Σ_i(z) between at the inner surface of the compact and the outer surface of the core rod) developed at the end of spring back. Both give rise to friction forces that are initially responsible for the resistance to ejection that the compact experiences, and both are much different than the radial pressure $\Sigma(z)$ developed in the final stage of compaction. In order to estimate these

radial pressures, as well as the displacements $V_{oD}(z)$, $V_{oC}(z)$, $V_{iC}(z)$, and $V_{iR}(z)$, we assume that the die, compact, and core rod behave elastically during spring back, and employ the corresponding elasticity solution for a set of three misfit cylinders. For simplicity, we assume that each cylinder is composed of infinitely many independent discs. The Young's moduli and Poisson ratios of the die, compact, and core rod are E_D, E_C, E_R, and ν_D, ν_C, ν_R, respectively

In this manner, by analogy to the elasticity solution for a thick walled cylinder subjected to internal pressure only given by equation (4.2), the die wall displacement is given by,

$$\frac{V_{oD}(z)}{R_o} = \left(\frac{(p_o \Sigma_o(z)/E_D)}{(R/R_o)} \right) \left(\frac{(R/R_o)^2}{(R/R_o)^2 - 1} \right) \left[\frac{(1-\nu_D)}{(R/R_o)} + (1+\nu_D)(R/R_o) \right] \quad . \tag{4.6}$$

From the elasticity solution for a thick walled cylinder subjected to both internal and external pressures, the radial displacement of the outer surface of the compact is given by:

$$\begin{aligned} \frac{V_{oC}(z)}{R_o} = {} & \frac{(p_o \Sigma_o(z)/E_C)}{\Delta} \left\{ \frac{(1-\nu_C)[1+(U_o/R_o)]}{[(R_i/R_o)+(U_i/R_o)]^2} + \frac{(1+\nu_C)}{[1+(U_o/R_o)]} \right\} \\ & - \frac{(p_o \Sigma_i(z)/E_C)}{\Delta} \left\{ \frac{(1-\nu_C)}{[1+(U_o/R_o)} + \frac{(1+\nu_C)}{[1+(U_o/R_o)]} \right\} \end{aligned} \tag{4.7}$$

and the radial displacement of the inside surface of compact is given by,

$$\frac{V_{iC}(z)}{R_o} = \frac{(p_o\Sigma_o(z)/E_C)}{\Delta}\left\{\frac{(1-\nu_C)}{[(R_i/R_o)+(U_i/R_o)]} + \frac{(1+\nu_C)}{[(R_i/R_o)+(U_i/R_o)]}\right\}$$
$$-\frac{(p_o\Sigma_i(z)/E_C)}{\Delta}\left\{\frac{(1-\nu_C)[(R_i/R_o)+(U_i/R_o)]}{[1+(U_o/R_o)]^2} + \frac{(1+\nu_C)}{[(R_i/R_o)+(U_i/R_o)]}\right\}, \quad (4.8)$$

where U_i and U_o are functions of z given by equations (4.2) and (4.3), and the quantity Δ is defined as,

$$\Delta \equiv \frac{1}{[1+(U_o/R_o)]^2} - \frac{1}{[(R_i/R_o)+(U_i/R_o)]^2} \quad . \quad (4.9)$$

Equations (4.8) and (4.9) demonstrate that the radial displacements at inside and outside surfaces of the compact are affected by the pressures at both surfaces. The core rod also springs back after the axial pressure exerted by the punch is removed. By analogy with solution (4.3) for a solid cylinder subjected to external pressure, the radial displacement of the core rod is simply,

$$\frac{V_{iR}(z)}{R_o} = -(1-\nu_R)\left(\frac{p_o\Sigma_i(z)}{E_D}\right)\left(\frac{R_i}{R_o}\right) \quad , \quad (4.10)$$

where the negative sign again indicates inward radial movement.

With displacements $U_i(z)$ and $U_o(z)$ at the final stage of compaction completely determined by equations (4.2) and (4.3), the four unknown displacements $V_{oD}(z)$, $V_{oC}(z)$, $V_{iC}(z)$, and $V_{iR}(z)$, and the two interface pressures $\Sigma_o(z)$ and $\Sigma_i(z)$ are determined by simultaneous equations (4.4), (4.5), (4.6), (4.7), (4.8), and (4.10).

4.4 Ejection

The radial pressures $\Sigma_o(z)$ and $\Sigma_i(z)$ at the interface give rise to frictional forces that resist ejection. Once the compact experiences resistance to ejection, it is compressed further by the applied ejection force, and due to Poisson effect, it tends to expand radially. The tendency to expand radially induces normal pressures between the die wall and the compact and the core rod and the compact. These normal pressures are added to those that are already present due to spring back of the die and core rod, and give rise to additional friction forces. Consequently, the ejection forces are larger than those that would be predicted based on the friction forces maintained by the normal pressures caused by spring back alone.

In order to describe this phenomenon in a one-dimensional model, we refer to the geometry and z-coordinate shown in Figure 2.1. In what follows, $P_e(z)$ is the dimensionless axial pressure (nondimensionalized by the compaction pressure p_o) induced throughout the compact during ejection. We note here that $P_e(z)$ is quite different from its counterpart, the dimensionless pressure $P(z)$ during compaction. Force equilibrium (during ejection) on a thin disc in the compact of thickness dz involves a balance between the axial pressures $P_e(z)$ and $P_e(z) + dP_e(z)$ acting on the two sides of the disc during ejection, the frictional stresses that can be maintained in the presence of radial pressures $\Sigma_o(z)$ and $\Sigma_i(z)$ caused by spring back alone and the frictional stresses further introduced by the Poisson effect of the ejection pressures $P_e(z)$. In this manner, the axial variation of the pressure induced by an applied ejection force is governed by

$$\frac{dP_e}{dz} = \frac{-2h}{[1-(R_i/R_o)^2]}\left\{ \left[\mu_o\Sigma_o + \mu_i(R_i/R_o)\Sigma_i(z)\right] + \left[\alpha_e[\mu_o + \mu_i(R_i/R_o)]P_e(z)\right]\right\} \quad , \qquad (4.11)$$

where μ_o and μ_i are respectively the coefficients of friction between the die wall and the compact and between the core rod and the compact. In the present analysis, μ_o and μ_i are equal to each other and are functions of density and pressure as given by equation (3.28), α_e is the ratio of the radial pressure induced to the axial pressure applied in the elastic compact. The first two terms on the left hand side of the force balance equation (4.11) account for the friction forces at the die wall and at the core rod that can be maintained by the pressures $\Sigma_o(z)$ and $\Sigma_i(z)$ induced by spring back. The last two terms account for the additional friction forces that develop as a result of the Poisson response to the axial pressure $P_e(z)$ induced by ejection.

The pressure ratio α_e measures the tendency of the compact to expand radially when it is compressed axially. Although it is analogous to the pressure ratio α used during compaction, it reflects the elastic behavior of the compact, the core rod, and the die during ejection, and is in no way affected by the plastic behavior described by α during compaction. For this reason, the value of α_e is not equal to the final value of α. In principle, the ratio α_e is determined by the elastic properties of the compact, the die and the core rod. This is because the radial pressures developed at the interfaces between the compact and the die wall and between the compact and the core rod depend on the radial displacements of each. A precise treatment of this mechanism is given in the Appendix. Here, we expect that the Young's moduli of the die and the core rod are significantly greater than that of the green compact, and the radial pressures induced by the axial ejection force cause negligible radial displacements in the die and core rod. If this is nearly so, then α_e may be approximated by an expression that depends only on the Poisson's ratio ν_C of the compact according to

$$\alpha_e = \frac{\nu_C}{1-\nu_C} \quad . \tag{4.12}$$

Equation (4.11) can be integrated at any stage of ejection. If d is the length of the compact that has emerged from the die during ejection (so that $0 \le d \le H$ where H is the height of compact after compaction), then at all axial locations $z \ge (H\text{-}d)/H$, the axial pressure $P_e(z)$ vanishes. Throughout the compact that is contained within the die (i.e. $0 \le z \le (H\text{-}d)/H$), the pressure increases from zero at $z = (H\text{-}d)/H$ to the value P_o that corresponds to the pressure applied by the lower punch at $z = 0$. The appropriate boundary condition for equation (4.11) is therefore given by

$$P_e(z = (H\text{-}d)/H) = 0 \tag{4.13}$$

The value of d depends on the axial displacement D of the bottom punch during compaction. So we get,

$$d = \begin{cases} 0 & (\text{when} \quad 0 \le D \le L\text{-}H) \\ D\text{-}(L\text{-}H) & (\text{when} \quad L\text{-}H \le D \le L) \end{cases} \quad . \tag{4.14}$$

Because the value of d remains unchanged until the punch displaces by an amount $D = (L\text{-}H)$, the simple model presented here will predict that ejection force also remains unchanged until $D = (L\text{-}H)$. Because d increases to H, as D increases beyond $(L\text{-}H)$ to L, the model will predict a rapid decrease to zero in the ejection force, for the punch displacements D increasing beyond $(L\text{-}H)$.

To obtain the axial pressure distribution $P_e(z)$ at any stage of ejection, the solution procedure requires first finding the radial pressures $\Sigma(z)$ at the end of compaction in the manner outlined in section 4.2. The radial pressures, $\Sigma_o(z)$ and $\Sigma_i(z)$, induced by spring back are then computed using the solution procedure described in section 4.3. Finally, for a given punch displacement D and corresponding value of the emerged length d given by equation (4.14), force balance (4.11) is integrated from $z=(H-d)/H$, where pressure vanishes to zero, to $z = 0$, where the unknown punch pressure P_o is applied to the bottom of the compact. The resulting integration gives variation of $P_e(z)$ from $z=0$ to $z=(H-d)/H$. In fact, the unknown punch pressure P_o is fixed by $P_o=P_e(z=0)$. The dimensionless ejection force is then given by $\pi[1-(R_i/R_o)^2]P_o$.

4.5 Results and Discussion

In order to obtain results in the manner described above, we must have knowledge of the elastic properties of the compact. Pavier et al (1999) performed cyclic loading-reloading tests on iron powder compacts to obtain a variation of Young's modulus E_C of the compact with its average relative density ρ throughout. In Figure 4.1, the solid data points are the results of the experiments. For relatively low values of density, the stiffness E_C of the compact increases gradually with increasing density. As the density approaches its maximum theoretical value, the stiffness increases dramatically. Also shown (as a solid curve) in Figure 4.1 is a parametric fit to the experimental results given by

$$E_C = \{ b + c\exp[-f(1-\rho^g)] \} \tag{4.15}$$

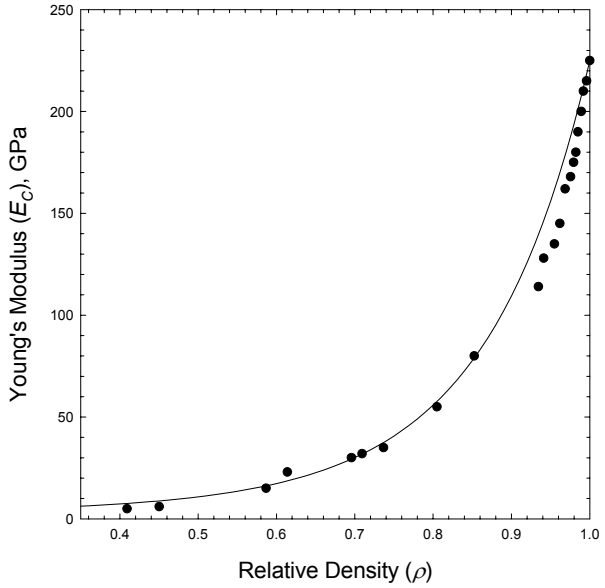

Figure 4.1 : Variation of E_C with ρ. The experimental measurements done by Pavier et al. (1999) are shown by solid dots and the empirical curve fit obtained to those results for b=2, c=223, f=5, g=1.5 in Equation (4.15), is shown by dark lir

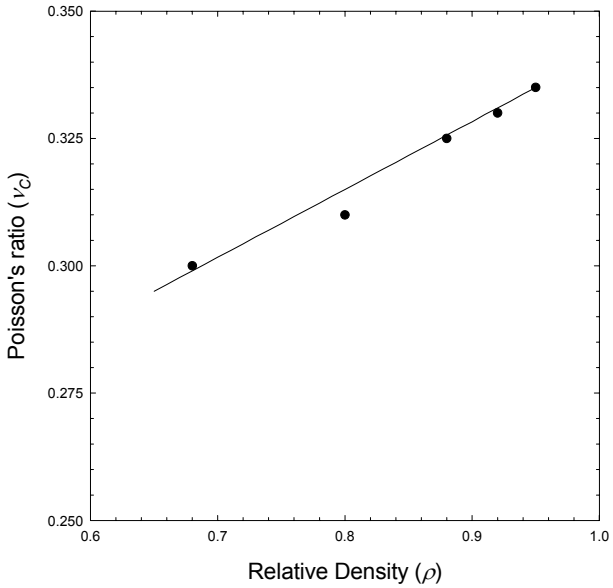

Figure 4.2 : Variation of ν_C with ρ. The experimental measurements done by Mosbah et al. (1996) are shown by solid dots and the empirical curve fit obtained to those results for A=.335, B=.133, C=.95, in Equation (4.16) is shown by dark line.

where the parameters b, c, f, and g are given as $b=2\times10^9$ N/m^2, $c=223\times10^9$ N/m^2, $f=5$, $g=1.5$.

Figure 4.2 shows (as solid data points) variation of the Poisson's ratio, ν_C, for the compact, as measured by Mosbah et al. (1996) on iron powder compacts. As the density increases over its full range, Poisson's ratio for the compact increases steadily. Also shown (as a solid curve) in Figure 4.2 is a linear fit to the experimental results given by,

$$\nu_C = A + B(\rho - C) \quad , \tag{4.16}$$

where the parameters A, B, and C are given as $A=.335$,$B=.133$, and $C=.95$.

In presenting results, unless otherwise specified, we focus on an iron powder blend of 98% SC100, 2% Cu and 1% zinc sterate, used by Gethin et al [1994] in measuring the ejection forces. The apparent density is 2.93g/cm^3, and the maximum theoretical density is 7.33 g/cm^3, so that $\eta=.40(=2.93/7.33)$. For compaction that ends at $H/L=.5$, for example, the average relative density ρ throughout the compact is .8, and according to equations (4.15) and (4.16), the elastic properties of the compact are $E_C=55$ GPa and $\nu_C=.315$. By contrast, we take the elastic properties of the die and the core rod to be $E_D=E_R=200$ GPa, and $\nu_D=\nu_R=.3$.

In all cases, we take coefficients of friction, $\mu_i=\mu_o$, as functions of axial pressure given by equation (3.28) with the parameters $\phi=1$, $\mu_2=.8$, and $\mu_1=.078$; the quantity βp_o is determined from the compaction analysis, as described in section 3.6. The radial-to-axial pressure ratio, α, depends on pressure according to equation (3.10) with the parameters $\alpha_o=.38$, $k=.11$, and $n=.6$.

In order to compare our predictions with corresponding measurements of Gethin et al [1994], we take the fill height L=80 mm unless otherwise specified, and regardless of the value of L, the compaction is carried out until H/L=.5. The inside and outside radii R_i and R_o in Figure 2.1 are equal to 8.5 mm and 12.5 mm. The corresponding geometric parameters for the model are parameters $a \equiv R_i/R_o$=.68 and L/R_o=6.4. The outside radius R of the die wall is assumed to be much larger than R_o, so that in all mathematical expressions, the ratio R_o/R can be neglected compared to 1.

With the elastic properties of the compact, die, and core rod known, it is possible to determine the dimensions of the compact at the end of compaction (before the applied punch pressure is removed) and at the end of springback (after the compaction load is removed but before the ejection force is applied). When the compact is fully ejected, it regains the shape it had at the end of compaction before the punch pressure was removed.

In Figures 4.3 and 4.4, we show, respectively, the radial deformations at the interface between the compact and the core rod and between the compact and the die wall for the two stages of compaction and ejection of interest. The solid curves in both figures give the inner shape (Figure 4.3) and the outer shape (Figure 4.4) of the compact just after compaction is complete but before the compaction load is removed. The two curves together give also the shape of the compact after ejection, and are determined by equations (4.3) and (4.2). The short dashed curves in both figures give the inner (Figure 4.3) and outer (Figure 4.4) shape of the compact after springback but before the ejection load is applied. These are determined by equations (4.8) and (4.7). For reference, the long dashed lines show the undeformed radial locations of the core rod (r=a$\equiv R_i/R_o$=.68) and die wall (r=1) before compaction begins. At the end of compaction, due to the

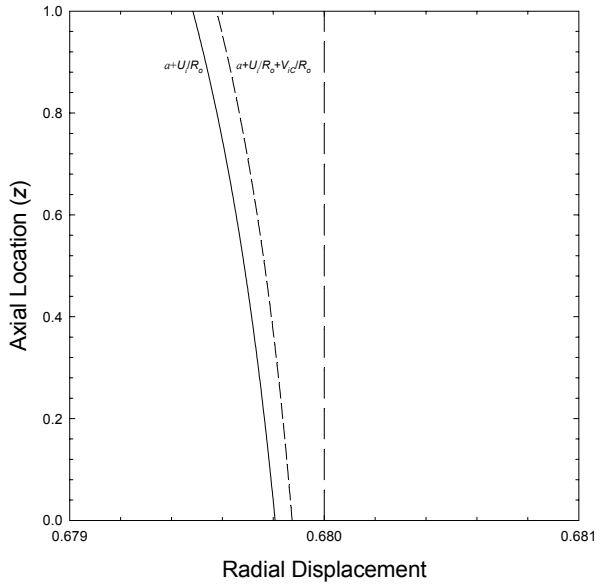

Figure 4.3 : Axial Variation of the inner radial displacement of the compact, before compaction (shown by long dashed curve), at the end of compaction (shown by solid curve), and after the spring back (shown by short dashed curve) with axial location z , for the parameter values uniform initial density η=.4, μ_2=.8, μ_1=.078, φ=1, α_0.=.38, k=.11 and n=.6 R_i/R_o=.68, R/R_o=800, H/L=.5, L/R_o=6.4, ν_C=.315, ν_D=ν_R=.3, E_C=55 GPa, E_D=E_R=200 GPa

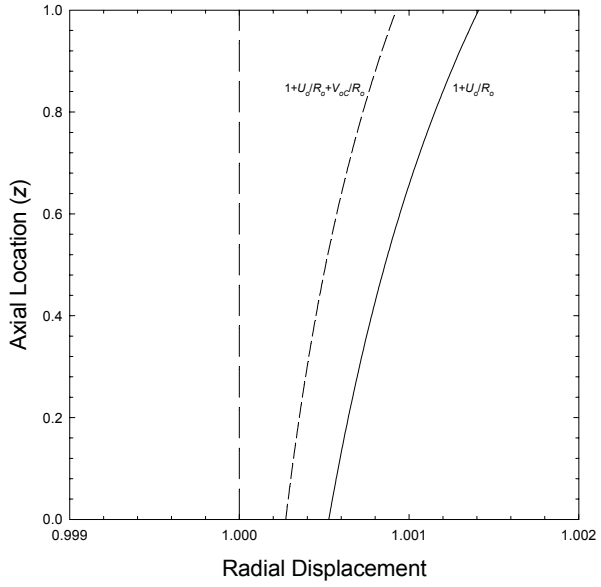

Figure 4.4: Axial Variation of the outer radial displacement of the compact, before compaction (shown by long dashed curve), at the end of compaction (shown by solid curve), and after the spring back (shown by short dashed curve) with axial location z , for the parameter values uniform initial density η=.4, μ_2=.8, μ_1=.078, φ=1, α_0.=.38, k=.11 and n=.6 R_i/R_o=.68, R/R_o=800, H/L=.5, L/R_o=6.4, ν_C=.315, ν_D=ν_R=.3, E_C=55 GPa, E_D=E_R=200 GPa

Poisson effect of the axial pressure, the interface between the compact and the core rod (shown by the solid curve in Figure 4.3) displaces radially inward, and the interface between the compact and the die wall (shown by the solid curve in Figure 4.4) displaces radially outward. Because the pressure decreases with distance from the top of the compact, so too do the radial displacements. When the compaction pressure is removed, the core rod and die wall spring back radially (to the positions shown by the short dashed curves), but not quite to their undeformed positions.

When the compact is fully ejected from the die, it regains the shape it had at the end of compaction, shown by the solid curves. For the case considered here, comparison of these curves to the (long dashed) lines corresponding to the undeformed shape of the die wall and core rod demonstrates that the difference between the radial dimensions of the ejected compact and the radial dimensions of the die are on the order of 0.1%. Given the practical tolerance for powder metal parts (see, for example, http://www.wake.com/Wakefield/tol.html), these differences can be significant.

In Figure 4.5, we show as solid lines the axial variations of the radial pressures, $\beta p_o \Sigma_i$ and $\beta p_o \Sigma_o$, due to the spring back at the inner (core rod) and outer (die wall) sides of the compact, respectively. For contrast, we also show as a dashed line, the corresponding variation of the induced radial pressure $\beta p_o \Sigma$ at the end of compaction. As expected, due to frictional effects, the radial compaction pressures and the elastic deformation of the die and the core rod decrease with distance from the punch. Consequently, when the applied compaction pressure p_o is removed, the radial pressures ($\beta p_o \Sigma_i$ and $\beta p_o \Sigma_o$) developed due to spring back also decrease with distance from the punch. The magnitudes of the radial springback pressures are less than (but of the same

order of) the magnitude of the radial compaction pressures at the end of compaction. Interestingly, the radial pressures due to springback are somewhat higher at the core rod than at the die wall.

There are two sources that make it necessary to apply a nonzero ejection force. The first is from the friction force maintained by the radial pressures ($\beta p_o \Sigma_i$ and $\beta p_o \Sigma_o$) arising from spring back. The second is addition to the friction that is maintained by the radial pressure arising from the Poisson effect experienced by the compact as the ejection pressure P_e is applied. The first two terms on the left hand side of the force balance equation (4.11) account for the first effect, and last two terms account for the additional second effect.

In Figure 4.6, we show (as a solid curve) the axial variation of the axial pressure $\beta p_o P_e(z)$ when the ejection force is first applied (i.e. D=0, and therefore d=0) and the part begins to slide through the die. This curve includes both friction effects described above. For comparison, we also show (as a dashed curve) the corresponding variation of axial pressure when the Poisson effect is ignored (i.e. α_e=0). The ejection pressure is maximum at the bottom of the compact, and decreases monotonically to the top. At the top, according to boundary condition (4.13) P_e is zero. A comparison of the solid and dashed curves demonstrates that in this case the Poisson effect during ejection can not be ignored and is responsible for about one third of the required ejection force. The pressure distribution throughout the compact is given by the curves shown in Figure 4.6 provided that no part of the compact has emerged from the die (i.e. $0 \le D \le L-H$), because in this range (according to equation (4.14)) $d \equiv 0$.

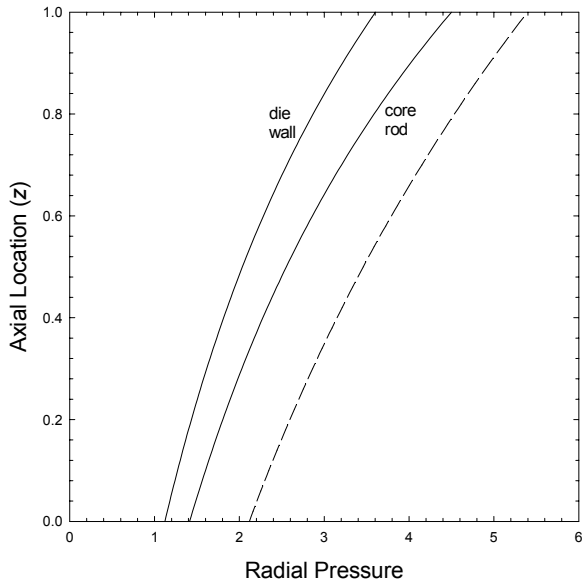

Figure 4.5 : Variation of $\beta p_o \Sigma$ indicated by dashed line and $\beta p_o \Sigma_i$ and $\beta p_o \Sigma_o$ indicated by solid lines with z for the parameter values uniform initial density η=.4, μ_2=.8, μ_1=.078, φ=1, $\alpha_{0.}$=.38, k=.11 and n=.6 R_i/R_o=.68, R/R_o=800, H/L=.5, L/R_o=6.4, ν_C=.315, ν_D=ν_R=.3, E_C=55 GPa, E_D=E_R=200 GPa

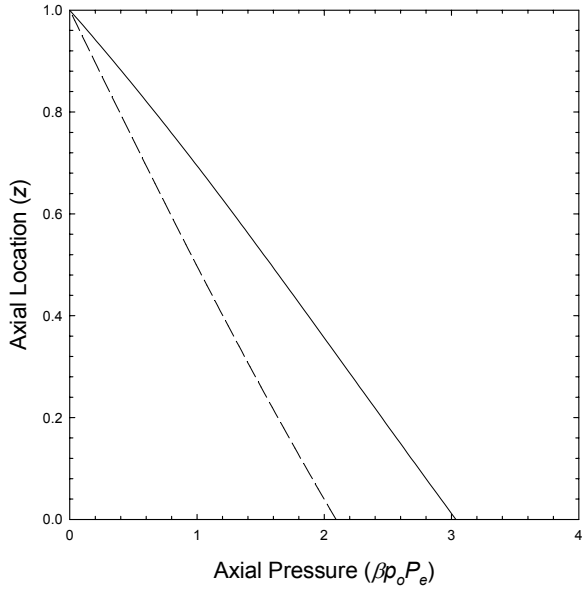

Figure 4.6 : Variation of the $\beta p_o P_e$ with z for improved ejection analysis (shown by solid line) and simple ejection analysis (shown by dashed line), at the start of ejection, for the parameter values uniform initial density η=.4, μ_2=.8, μ_1=.078, φ=1, $\alpha_{0.}$=.38, k=.11 and n=.6 R_i/R_o=.68, R/R_o=800, H/L=.5, L/R_o=6.4, ν_C=.315, ν_D=ν_R=.3, E_C=55 GPa, E_D=E_R=200 GPa

In Figure 4.7, we show how the axial ejection pressure profile changes as the ejection proceeds. With H/L=.5, the part does not emerge from the die until $D(=L-H)=H$, so that for all values of D/H between 0 and 1 the axial pressure variation corresponds to that given by the solid curve in Figure 4.6. When the bottom punch moves by an amount D that is greater than L-H(=H), the compact emerges from the die, d increases according to equation (4.14), and the total area of the compact that remains in contact with the die walls and core rod decreases. This, in turn, reduces both the friction to be overcome and the ejection pressure required from the bottom punch. In the case when H/L=.5, the values D/H=1.25, 1.5, and 1.75 shown in Figure 4.7 correspond to times at which the part is 25, 50, and 75 percent ejected. At all instances when the compact is only partly contained in the die, the pressure vanishes at all points in the compact that are outside the die.

Figure 4.8 shows (as solid curves) the axial variation of the radial pressure $\beta p_o(\Sigma_i+\alpha_e P_e)$ at the core rod and the radial pressure $\beta p_o(\Sigma_o+\alpha_e P_e)$ at the die wall when the ejection force is first applied (i.e. D=0, and therefore d=0) and the part begins to slide through the die. Also shown (as dashed curves) for contrast are the corresponding variations predicted when $\alpha_e=0$. The dashed lines are identical to the radial pressures due to spring back as shown (as solid curves) in Figure 4.5. Because the spring back analysis accounts for radial variations, the model predicts different radial pressures at the core rod and at the die wall. When the Poisson effect on ejection is ignored, the radial pressures vary axially in a manner that is qualitatively similar to the variations of the compaction pressures themselves. However, the Poisson effect is most pronounced at the bottom of the compact (where the spring back is least pronounced), and decreases

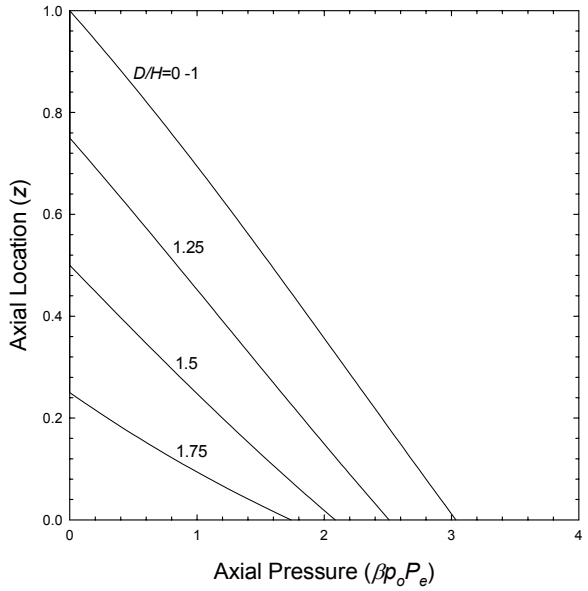

Figure 4.7 : Variation of the $\beta p_o P_e$ with z as the ejection evolves for D/H=0-1, 1.25, 1.5, 1.75, for improved ejection analysis, for the parameter values uniform initial density η=.4, μ_2=.8, μ_1=.078, φ=1, α_0.=.38, k=.11 and n=.6 R_i/R_o=.68, H/L=.5, L/R_o=6.4, ν_C=.315, $\nu_D=\nu_R$=.3, E_C=55 GPa, $E_D=E_R$=200 GPa, R/R_o=800

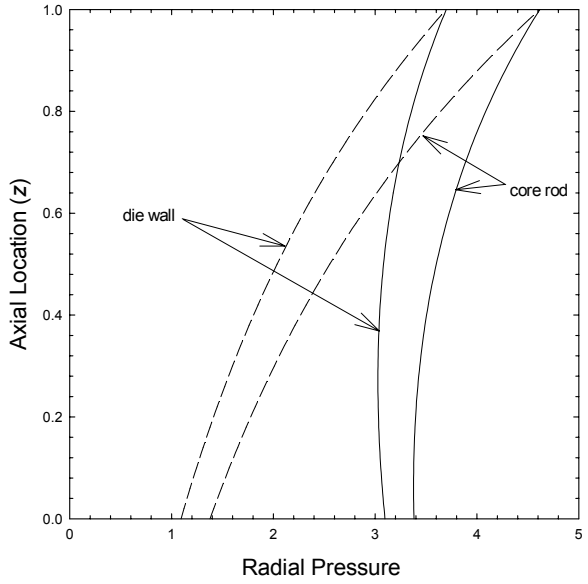

Figure 4.8 : Variation of the radial pressures, with z. Solid lines show the results corresponding to improved ejection analysis ($\beta p_o(\Sigma_i+\alpha_e P_e)$ and $\beta p_o(\Sigma_o+\alpha_e P_e)$) and dashed lines correspond to simple ejection analysis ($\beta p_o \Sigma_i$ and $\beta p_o \Sigma_o$) for the parameter values uniform initial density η=.4, μ_2=.8, μ_1=.078, φ=1, α_0.=.38, k=.11 and n=.6 R_i/R_o=.68, H/L=.5, L/R_o=6.4, ν_C=.315, $\nu_D=\nu_R$=.3, E_C=55 GPa, $E_D=E_R$=200 GPa, R/R_o=800

monotonically until it vanishes at the top (where the spring back is most pronounced). Consequently the radial pressure variations are qualitatively very different when the Poisson effect during ejection is incorporated.

Figure 4.9 shows the evolution of the radial pressure variation at the die wall, as the ejection proceeds. As in Figure 4.7, with H/L=.5, the part does not emerge from the die until $D(=L-H)=H$, so that for all values of D/H between 0 and 1 the axial pressure variation corresponds to that given by the corresponding solid curve in Figure 4.8. When the bottom punch moves by an amount D that is greater than $L-H(=H)$ the compact emerges from the die, d increases according to equation (4.14), and the total area of the compact that remains in contact with the die walls and core rod decreases. This reduces both the friction to be overcome, and the axial ejection pressure required from the bottom punch. This in turn reduces the corresponding radial pressures. As in Figure 4.7, the values D/H=1.25, 1.5, and 1.75 shown in Figure 4.9 correspond to times at which the part is 25, 50, and 75 percent ejected.

To compare the predictions of the model presented here with the results of the ejection experiments carried out by Gethin et al [1994], we need to determine the value of the compressibility factor β for the iron powder blend (98% SC100, 2% Cu and 1% zinc sterate) used by Gethin et al [1994]. As in section 3.4, we compare the measured variation of applied compaction load at top and the transmitted load at the bottom of the compact with the results predicted by our model, and adjust β to obtain the best match. Figure 4.10 shows the experimental data (as solid points) obtained by Gethin et al. (1994) for the variation of the force at the top and bottom of the compact during compaction. The solid curves show the corresponding theoretical predictions (made by the model

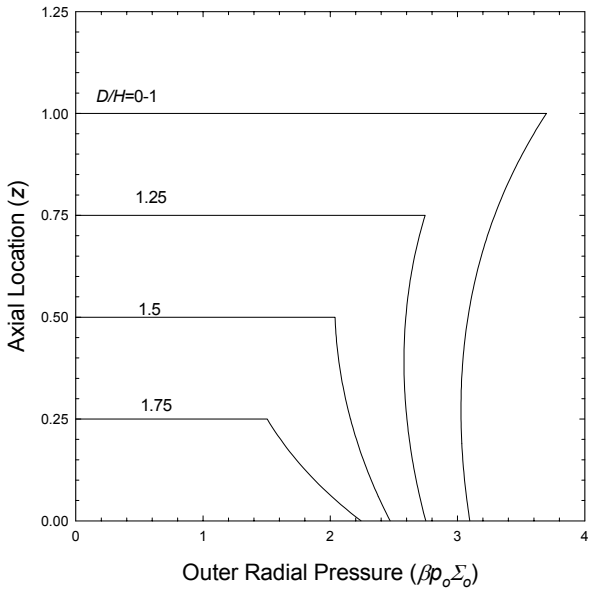

Figure 4.9 : Variation of the outer radial pressure $\beta p_o \Sigma_o$, with z as the ejection evolves for D/H=0-1, 1.25, 1.5, 1.75 , for improved ejection analysis, for the parameter values uniform initial density η=.4, μ_2=.8, μ_1=.078, φ=1, α_0.=.38, k=.11 and n=.6 R_i/R_o=.68, H/L=.5, L/R_o=6.4, ν_C=.315, ν_D=ν_R=.3, E_C=55 GPa, E_D=E_R=200 GPa, R/R_o=800.

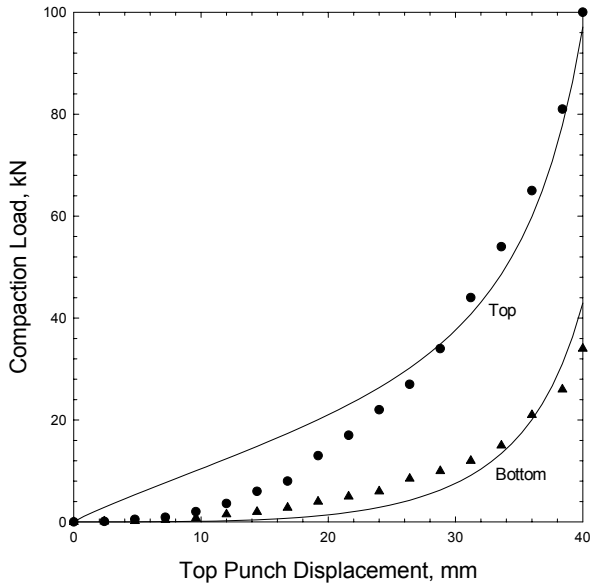

Figure 4.10 : Variation of the compaction load with top punch displacement as the compaction evolves. The solid points indicate experimental values obtained by Gethin et al (1994), circles are at the top and the triangles at the bottom and curve shows the results of this model for the parameter values uniform initial density η=.4,μ_2=.8, μ_1=.078, φ=1, α_0.=.38, k=.11 and n=.6 R_i/R_o=.68, H/L=.5, L/R_o=6.4, ν_C=.315, ν_D=ν_R=.3, E_C=55 GPa, E_D=E_R=200 GPa, L=80mm, R_i=8.5mm, R=10m.

described in Chapter 3) for a compressibility factor of $\beta=2.6\times10^{-8}$ m^2/N, chosen as the best fit. In addition to measuring the forces during compaction, Gethin et al (1994) also measured variation with lower punch displacement of the force required throughout ejection. With all parameters (including β) known, we can compare the results of these ejection experiments with the corresponding predictions of the model presented here. In Figure 4.11, we show the variation with punch displacement of the required ejection force when the fill height L=80 mm and the compact height H=40 mm. The solid points indicate the experimental results while the solid line indicates the result obtained using the ejection analysis described in the previous sections. For comparison, we also show (as a dashed curve) the predictions made when the Poisson effect during ejection is ignored (i.e. $\alpha_e=0$). As it must, the model predicts that while the compact is fully contained within the die (i.e. $0<D<40$ mm), the ejection force remains unchanged. As an increasingly larger fraction of the compact emerges, the friction between the compact and the die decreases, and the required ejection force decreases to zero when the compact is fully removed. The experimental results indicate that, while the bottom punch moves upward but while the compact is still fully contained in the die, the ejection force appears to increase. While the reasons for this increase are not clear, it may indicate that in the experiments the compact is accelerating while it is contained in the die. The predictions made by the current model, on the other hand, are based on the assumption that the compact moves with constant upward velocity. Despite this qualitative discrepancy, most notable is the excellent agreement between the magnitudes of the measured and predicted ejection forces in this range ($0<D<40$ mm) of punch displacement provided that the Poisson effect during ejection is included. Moreover, even in the experiments, once

the compact emerges from the die, the effects of decreasing friction dominate the ejection force, which decreases to zero when the part is fully ejected. Again, in this range of punch displacement (i.e. 40 mm<D<80 mm), agreement between the experimental results and theoretical predictions is quite good provided the Poisson effect is included.

In Figure 4.12, we show corresponding results when the fill height L=40 mm and the compact height H=20 mm. As in Figure 4.11, the solid points are the experimental results obtained by Gethin et.al. (1994), the solid curve indicates the result obtained using the ejection analysis described in the previous sections, and the dashed curve gives the prediction with α_e=0. Comments made concerning Figure 4.11 apply to Figure 4.12 as well.

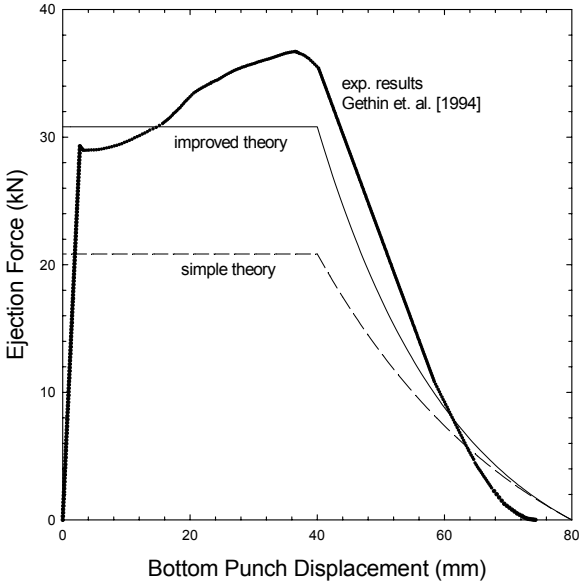

Figure 4.11: Variation of the ejection force with bottom punch displacement with the results of improved ejection analysis (shown by solid line) superimposed over those of simple theory and compared with the experimental results of Gethin et al., for the parameter values uniform initial density η=.4, μ_2=.8, μ_1=.078, φ=1, α_0.=.38, k=.11 and n=.6 R_i/R_o=.68, R/R_o=800, H/L=.5, L/R_o=6.4, ν_C=.315, ν_D=ν_R=.3, E_C=55 GPa, E_D=E_R=200 GPa, L=80 mm, R_i=8.5 mm..

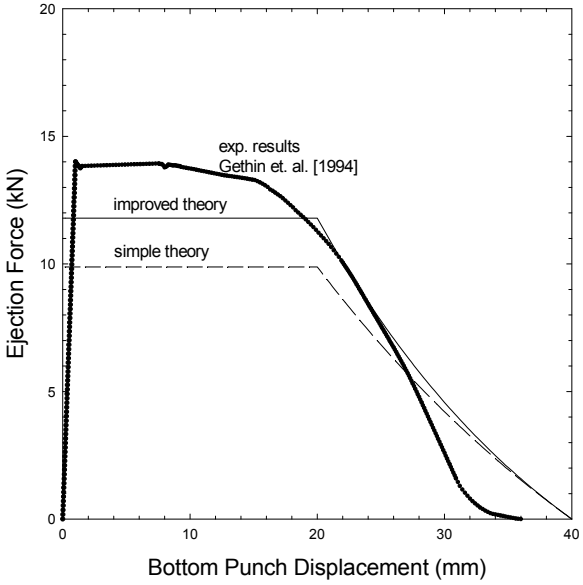

Figure 4.12: Variation of the ejection force with bottom punch displacement with the results of improved ejection analysis (shown by solid line) superimposed over those of simple theory and compared with the experimental results of Gethin et al., for the parameter values uniform initial density η=.4, μ_2=.8, μ_1=.078, φ=1, α_0.=.38, k=.11 and n=.6 R_i/R_o=.68, R/R_o=800, H/L=.5, L/R_o=3.2, ν_C=.315, ν_D=ν_R=.3, E_C=55 GPa, E_D=E_R=200 GPa, L=40 mm, R_i=8.5 mm..

CHAPTER 5

Conclusion

In this work, we have extended the existing phenomenological theory of Richman to investigate the problems involving a variation in initial density distribution for single punch compaction in hollow cylindrical compacts. We looked into the effects of nonuniform initial density distribution on the resulting final pressure and density variations. We then included the pressure and density dependence of the coefficients of friction and radial to axial pressure ratio into the model. Finally, we modeled the springback and ejection of the compact. It was not always possible to obtain solutions in the closed form and we resorted to numerical solutions, when needed.

The analysis was carried out as a continuum analysis. Powder particles are neither of the same size nor do they have the same shape. Existence of varying particle size would have introduced significant complications in the analysis and so, the work here assumed that all particles have the same size and spherical shape. Particle size plays an important role as far as the applicability of the continuum analysis is concerned. Larger the particle size, less smooth will be the variation of the physical properties of the compact, questioning the assumption of continuum. So, the applicability of this analysis is valid to the problems where the particle size and shape is such that the continuum assumption is not obviously violated. Also, the particles were assumed to have no attractive or repulsive forces and the effect of the interstitial fluids (air, lubricants and binders) was assumed to be negligible. Also the effect of gravity was ignored in favor of the tremendous compaction force. The inertia of the punch during the downward

compacting motion, was also neglected for the same reason, and hence the model is insensitive to compaction speeds.

Equations of motion were applied to differential volume satisfying the balance of mass and the balance of momentum. Equation of state, which related the local pressure to the local density, was used. A constitutive relation, formulating the dependence of radial pressure on axial, was employed. Within the framework of these equations, solutions were obtained to the density and pressure distributions throughout the compact. The total applied compaction force on the punch, the friction forces between the powder and the containing walls of the compact served as boundary conditions. Additionally, the compatibility constraints that the powder particles in contact with the top and the bottom punches maintain their positions relative to the punches, provide more boundary conditions.

In Chapter 2, we focused attention on the effects of nonuniformity in the initial density distribution. First, we saw that because of friction, pressure decreases exponentially in the downward direction but radial variation of pressure is almost negligible. We observed that the radial density variations evolving from uniform initial density distribution were negligible and also that in the case of nonuniform initial fills, the initial nonuniformities in radial density variations die down during compaction. On the contrast, density variations are significant in axial direction. Also, the axial variation of density during the compaction, initially increases, reaches a maximum and then decreases to its final value, instead of increasing monotonically. The effects of increase in coefficient of friction, increase in radial to axial pressure ratio and increase in the ratio of

radii, on final density variation in axial direction are qualitatively similar. Increase in any of these, results in larger variations in final density distribution.

We also solved the inverse problems where to obtain a desired final state, we predicted the required initial density distribution. An important conclusion that can be drawn from these results is, to obtain a compact with better uniformity in density distribution, we should start with initial fill, more dense at the bottom rather than starting with a uniform initial density distribution. Also this initial variation in density required to obtain a uniform final density distribution, increases with increase in the coefficient of friction or the ratio of radii or the radial to axial pressure ratio.

In Chapter 3, we included in our model the dependence of radial to axial pressure ratio and coefficients of friction on pressure and density. We saw the effect of this dependence on the axial density distributions. The varying radial to axial pressure ratio as a function of pressure can be approximated by a constant radial to axial pressure ratio appropriate to that particular stage of compaction. However, the density variations produced by using such constant radial to axial pressure ratio are always more than that produced by varying radial to axial pressure ratio. The effect of including this dependence was more of a quantitative nature than a qualitative one. We obtained the value of compressibility factor β for Distalloy AE powder blend. For the same powder blend, we also obtained the relation between the compressibility and the radial to axial pressure ratio.

Including the dependence of coefficient of friction on pressure and density indicated quantitative differences in the axial density variations obtained using an appropriate constant value pertaining to that stage of compaction. Comparison of the

results obtained using varying coefficient of friction and using an appropriate constant value was excellent near the final stages of compaction and was poor during initial stages. Also, it was seen that a substantial part of applied load is spent in overcoming friction during the initial stages of compaction.

Finally, in Chapter 4, we obtained the radial pressures resulting form the springback of the die walls after removal of applied compaction load. The shape of the compact was estimated. We saw the ejection pressure is maximum at the bottom of the compact and then we also obtained the variation of ejection pressure as ejection proceeds. Then for iron powder, we compared the variation of applied ejection force predicted by our model (both including and excluding the contribution of Poisson effect of applied ejection pressure) and experimental results of Gethin et al. The results indicated good agreement and we observed that the Poisson effect of applied ejection pressure is significant in the prediction of ejection force.

REFERENCES

Ariffin, A., Gethin, D., Lewis, R., (1998). Finite element simulation and experimental validation for multilevel powder compact. Powder Metallurgy, 41(3), 189-197.

Bocchini, G. F., Rapallo, (1995). Friction effects in metal powder compaction, part one-theoretical aspects. Advances in Powder Metallurgy 2, 115-151.

Boresi, A., Chong, K. (2000). Elasticity in engineering mechanics, Elsevier Publication

Briscoe, B., Rough, S., (1998). The effects of wall friction on the ejection of pressed ceramic parts. Powder Technology 99, 228-233.

Brown, S. B., Weber, G. G. B., (1988). A constitutive model for the compaction of metal powders. Modern Developments in Powder Metallurgy 18-21, 465-476.

Doremus, P., Geidreau, C., Martin, A., Debove, L., Lecot, R., Dao, M., (1995). High pressure triaxial cell for metal powder. Powder Metallurgy 38(4), 284-287.

Ferguson, B., Krauss, T., (1989). Modeling ejection of die pressed parts. Advances in Powder Metallurgy 1, 147-164.

Gasiorek, S., Korczak, K. Z., Kaminski, K. K., (1989). Compressibility of metal powders. Advances in Powder Metallurgy 1, 53-62.

German, R. M., (1994). Powder Metallurgy Science. Published by Metal Powder Industries Federation.

Gethin, D., Lewis, R., Ariffin, A., (1995). Modeling compaction and ejection processes in the generation of green powder compacts. AMD- Vol 216, Net Shape Processing of Powder Materials, ASME 1995, 27-45.

Gethin, D. T., Tran, V. D., Lewis, R. L., Ariffin A. K., (1994). An investigation of powder compaction processes. The International Journal of Powder Metallurgy 30(4), 385-398.

Gethin, D., Ariffin, A., Tran, D., Lewis, R., (1994). Compaction and ejection of green powder compacts. Powder Metallurgy 37(1), 42-52.

Guyoncourt, D.M.M., Tweed, J. H., Gough, A., Dawson, J., Pater, L., (2001). Constitutive data and friction measurement of powders using instrumented die. Powder Metallurgy, 44(1), 25-33.

Holownia, B., (1996). Balanced die method for metal powder compaction. Powder Metallurgy, 39(3), 207-209.

Kim, K. T., Suh, J., Kwon, Y. S., (1990). Plastic yield of cold isostatically pressed and sintered porous iron under tension and torsion. Powder Metallurgy 33(4), 321-326.

Morimoto, Y., Hayashi, T., Takei, T., (1982). Mechanical behavior of powders during compaction in a mold of variable cross sections. The International Journal of Powder Metallurgy and Powder Technology 18(2), 129-145.

Mosbah, P., Bouvard, D., Ouedraogo, E., Stutz, P., (1997). Experimental techniques for analysis of die pressing and ejection of metal powder. Powder Metallurgy, 40(4), 269-277.

Mosbah, P., Bouvard, D., (1996). Finite element simulation of die compaction and ejection of iron powder. Advances in Powder Metallurgy, vol 7, 23-37.

Pavier, E., Doremus, P., (1999). Triaxial characterization of iron powder behavior. Powder Metallurgy 42(4), 345-352.

Pavier, E., Doremus, P., (1996). Mechanical behavior of a lubricated iron powder. Advances in Powder Metallurgy and Particulate Materials, vol 2 (6), 27-40.

Redanz, P., (2001). A study of stresses in powder compacted components during and after ejection. International Journal of Solids and Structures 38, 759-775.

Richman M. W., Gaboriault, E., (2000). Radial and axial variations of pressures and densities in hollow cylindrical p/m compacts. Proceedings of int'l conference on Powder Metal and Particulate Materials, 2000.

Richman, M.W., Gaboriault, E., (1999). The effects of fill-nonuniformities on the densified states of cylindrical green p/m compacts. Proceedings of int'l conference on Powder Metal and Particulate Materials, 1998.

Richman, M. W., Apelian, D., Burgos, G., (1998). A simple analysis of compaction of multi-powder p/m parts. Proceedings of int'l conference on Powder Metal and Particulate Materials, Las Vegas, Nevada, 1998.

Roure, S., Bouvard, D., Doremus, P., Pavier, E., (1999). Analysis of die compaction of tungsten carbide and cobalt powder mixtures. Powder Metallurgy 42(2), 164-170.

Shima, S., Oyane, M., (1976). Plasticity theory for porous metals. Int. J. Mechanical Science 18, 285-291.

Sinka, I. C., Cocks, A. C. F., Morrison, C. J., Lightfoot, A., (2000). High pressure triaxial facility for powder compaction. Powder Metallurgy 43(3), 253-261.

Solimanzad, N., Wikstrom, H., Larsson, R., (2001). A new device for measurement of

friction during metal powder compaction. Proceedings of PM2TEC 2001, May 2001.

The Wakefield Corporation, (2003). General commercial tolerances. Company website http://www.wake.com/Wakefield/tol.htm.

Trasorras, J. R. L., Parameswaran, R., Cocks, A. C. F., (1998). Mechanical behavior of metal powders and powder compaction modeling. ASM Handbook Volume 7, 326-342.

Trasorras, J. R. L., Krishnaswami, S., Godby, L. V., Armstrong, S., (1995). Finite element modeling for the design of steel powder compaction, Advances in Powder Metallurgy and Particulate Materials 1(2), 153-167.

Trasorras, J. R. L., Armstrong, S., McCabe, T. J., (1994). Modeling the compaction of steel powder parts. Advances in Powder Metallurgy and Particulate Materials 7, 33-50.

Watson, T. J., Wert, J. A., (1993). On the development of constitutive relations for metallic powders. Metallurgical Transactions A 24A, 2071-2081.

White D. G., (2001). State of the North American P/M industry-2001, Proceedings of PM2TEC 2001, May 2001.

Wikman, B., Solimanzad, N., Larsson, R., Oldenburg, M., Haggblad, H. A., (2000). Wall friction coefficient estimation through modeling of powder die pressing experiment. Powder Metallurgy 43(2), 132-138.

APPENDIX

We are concerned here with three coaxial, linear-elastic cylinders in contact: a solid cylinder (core rod) of radius R_i; a hollow cylinder (compact) of inside radius R_i and outside radius R_o; and a large hollow cylinder (die) of inside radius R_o and outside radius R. The modulus of elasticity and the Poisson's ratio of the core rod, compact, and die are E_R and ν_R, E_C and ν_C, and E_D and ν_D, respectively. For simplicity, we assume that the surfaces of the cylinders (at R_i and R_o) are frictionless. The z-coordinate measures axial distance along the cylinder, and the r-coordinate measures distance from the centerline of each cylinder. The compact is subjected to an external compressive axial pressure p_e as shown in Figure A.1.

In response to the applied pressure p_e, the radial displacements $u_R(r)$ (in the core rod), $u_C(r)$ (in the compact) and $u_D(r)$ (in the die) depend on r only. The axial displacements $w_R(z)$ (in the core rod), $w_C(z)$ (in the compact) and $w_D(z)$ (in the die) depend on z only. The tangential displacements, the shear strains, and the shear stresses vanish everywhere in all three cylinders.

We focus first on the compact. The normal strains in the radial, tangential, and axial directions are du_C/dr, u_C/r and dw_C/dz respectively. The corresponding normal stresses are

$$\sigma_{rr} = \frac{E_C(1-\nu_C)}{(1-2\nu_C)(1+\nu_C)}\left[\frac{du_C}{dr} + \frac{\nu_C}{1-\nu_C}\left(\frac{u_C}{r} + \frac{dw_C}{dz}\right)\right] \quad , \tag{A.1}$$

$$\sigma_{\theta\theta} = \frac{E_C(1-\nu_C)}{(1-2\nu_C)(1+\nu_C)}\left[\frac{u_C}{r} + \frac{\nu_C}{1-\nu_C}\left(\frac{du_C}{dr} + \frac{dw_C}{dz}\right)\right] \quad , \tag{A.2}$$

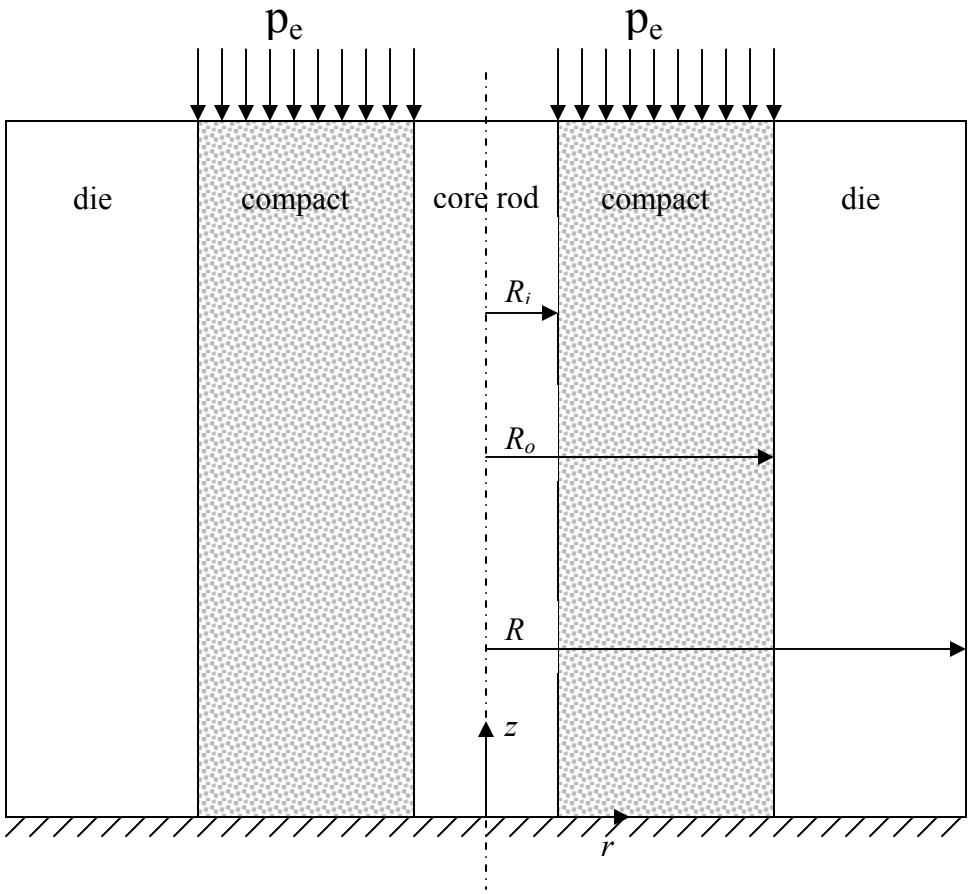

Figure A.1: Three concentric cylinders of which the middle cylinder is compressed by an axial pressure p_e.

and

$$\sigma_{zz} = -p_e = \frac{E_C(1-\nu_C)}{(1-2\nu_C)(1+\nu_C)}\left[\frac{dw_C}{dz} + \frac{\nu_C}{1-\nu_C}\left(\frac{du_C}{dr} + \frac{u_C}{r}\right)\right] \quad . \tag{A.3}$$

Rearranging equation (A.3) yields the axial strain,

$$\frac{dw_C}{dz} = \frac{-(1-2\nu_C)(1+\nu_C)p_e}{E_C(1-\nu_C)} - \frac{\nu_C}{1-\nu_C}\left(\frac{du_C}{dr} + \frac{u_C}{r}\right) \quad , \tag{A.4}$$

in terms of the applied axial pressure and the strains in the radial and tangential directions.

The radial equilibrium equation in this simple case reduces to

$$\frac{d\sigma_{rr}}{dr} + \frac{1}{r}\left(\sigma_{rr} - \sigma_{\theta\theta}\right) = 0 \quad . \tag{A.5}$$

By employing equations (A.1) and (A.2) in equation (A.5), we find that,

$$\frac{d^2u_C}{dr^2} + \frac{1}{r}\frac{u_C}{r} - \frac{u_C}{r^2} = 0 \quad . \tag{A.6}$$

Therefore,

$$u_C = \frac{A}{r} + Br \quad , \tag{A.7}$$

where the constants A and B are determined by appropriate boundary conditions. The tangential and axial equilibrium equations are identically satisfied.

When equations (A.7) and (A.4) are employed in equations (A.1) and (A.2) , we find that the radial variations of σ_{rr} and $\sigma_{\theta\theta}$ are given by,

$$\sigma_{rr} = \frac{-\nu_C p_e}{1-\nu_C} + E_C\left[\frac{-A}{(1+\nu_C)r^2} + \frac{B}{(1-\nu_C)}\right] \tag{A.8}$$

and,

$$\sigma_{\theta\theta} = \frac{-\nu_C p_e}{1-\nu_C} + \frac{E_C}{(1+\nu_C)}\left[\frac{A}{r^2} + D\right] \tag{A.9}$$

In particular, if p_1 and p_2 are the unknown, induced radial pressures at the interfaces at $r=R_i$ and $r=R_o$, then according to equation (A.8),

$$-p_1 + \frac{\nu_C p_e}{1-\nu_C} = E_C\left[\frac{-A}{(1+\nu_C)R_i^{\,2}} + \frac{B}{(1-\nu_C)}\right] \tag{A.10}$$

and,

$$-p_2 + \frac{\nu_C p_e}{1-\nu_C} = E_C\left[\frac{-A}{(1+\nu_C)R_o^{\,2}} + \frac{B}{(1-\nu_C)}\right] \tag{A.11}$$

Equations (A.10) and (A.11) may be inverted to find the unknown constants of integration A and B in terms of the unknown induced radial pressures p_1 and p_2. In fact. Equations (A.10) and (A.11) demonstrate that AEC/pe and BEC/pe depend linearly on p1/pe and p2/pe, and nonlinearly on ν_C, R_i and R_o.

In order to determine p_1 and p_2, we first write down the radial displacements $u_R(r)$ and $u_D(r)$ in the core rod and die wall, respectively. The core rod is simply a solid, elastic

cylinder of radius R_i subjected to external pressure p_1, and the die wall is simply an elastic cylinder of inside radius R_o and outside radius R, subjected to internal pressure p_2 and no external pressure. The classical elasticity solutions for these cases (see for example: Boresi and Chong (2000)) yields:

$$u_R = \frac{-(1-\nu_R)p_1 r}{E_R} \quad , \tag{A.12}$$

and

$$u_D = \frac{(1+\nu_D)R_o^{\,2} p_2 r}{E_D(R^2 - R_o^{\,2})}\left[\frac{R^2}{r^2} + \frac{(1-\nu_D)}{(1+\nu_D)}\right] \quad . \tag{A.13}$$

The two conditions that guarantee that the displacements $u_R(r)$, $u_C(r)$ and $u_D(r)$ are compatible with one another are:

$$u_R(r = R_i) = u_C(r = R_i) \quad , \tag{A.14}$$

and

$$u_C(r = R_o) = u_D(r = R_o) \quad , \tag{A.15}$$

where, $u_C(r)$ is given by equation (A.7).

Equations (A.10), (A.11), (A.14) and (A.15) determine p_1, p_2, A and B. Although we do not show the explicit solution here, it is easy to demonstrate that the values p_1/p_e and p_2/p_e depend on E_R/E_C, E_D/E_C, ν_R, ν_C, ν_D, R_i, R_o and R. In the extreme case, when the core rod and the die are rigid, E_R/E_C and E_D/E_C become unbounded and u_R and u_D vanish

for all r. Equation (A.14) and (A.15) dictate that A=0 and B=0 so that u_C also vanishes for all r. In this case, equations (A.10) and (A.11) yield:

$$\frac{p_1}{p_e} = \frac{p_2}{p_e} = \frac{\nu_C}{1-\nu_C} \quad . \tag{A.16}$$

This is the simple result used in Chapter 4. (see equation (4.12) with α_e defined as the radial-to-axial pressure ratio)

Interestingly, for general parameter values, the pressure ratios p_1/p_e and p_2/p_e are not equal. In this case, equation (4.12) would be modified to

$$\frac{dP_e}{dz} = \frac{-2}{\left[1-(R_i-R_o)^2\right]} \left\{ \begin{array}{l} \left[\mu_o \Sigma_o + \mu_i (R_i/R_o)\Sigma_i(z)\right] \\ +\left[\alpha_2 \mu_o + \alpha_1 \mu_i (R_i/R_o)\right] P_e(z) \end{array} \right\} \quad , \tag{A.17}$$

where α_1 and α_2 are the radial-to-axial pressure ratios at r=R_i and r=R_o respectively. A more precise model than that employed in Chapter 4 would include taking α_1= p_1/p_e and α_2= p_2/p_e, where p_1/p_e and p_2/p_e are determined as described above.

In Figure A.2, we show the variation of p_1/p_e and p_2/p_e with E_R/E_C=E_D/E_C for ν_R=ν_D=0, .3 and .5, when R_i/R_o=.68 and ν_C=.315. These values of R_i/R_o and ν_C coincide with those used in Chapter 4, where we employed ν_R=ν_D=.3. When E_R and E_D are equal to zero, the compact experiences no resistance to radial expansion when it is compressed axially. Consequently, no radial pressures are developed, and p_1=p_2=0. As the stiffness of the core rod and die increases relative to the stiffness of the compact itself, the resistance to radial expansion, and therefore the induced radial pressures increase as well. (Although p_1 and p_2 are not exactly equal, they are indistinguishable in Figure A.2. This is primarily

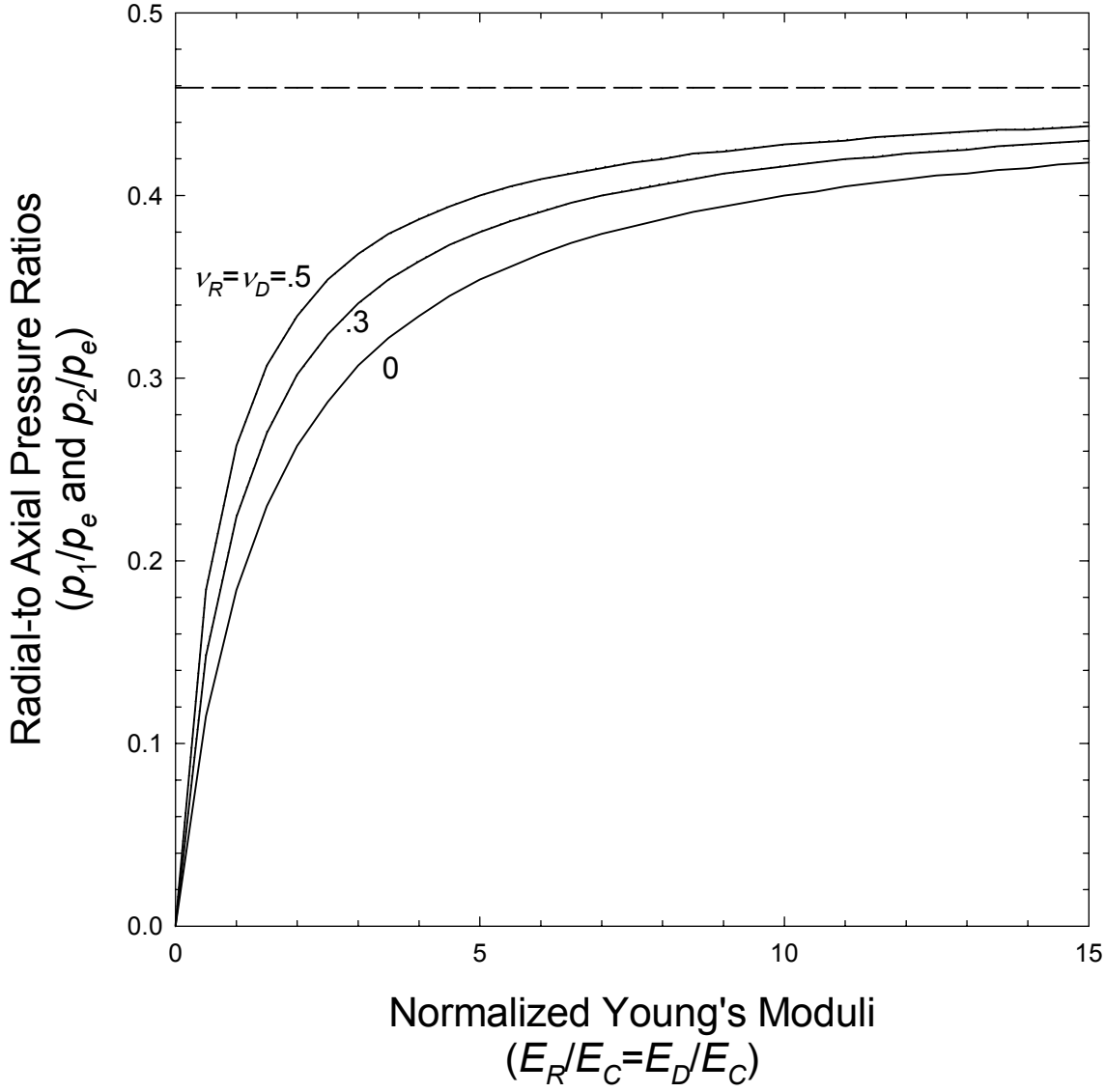

Figure A.2: The variation of p_1/p_e and p_2/p_e with E_R/E_C=E_D/E_C for ν_R=ν_D=0, .3 and .5, when R_i/R_o=.68 and ν_C=.315.

because of our assumption that the core rod and the die have equal elastic properties.) As the stiffness of the core rod and die becomes large compared to that of the compact, the radial-to-axial pressure ratios approach $\nu_C/(1-\nu_C)$=.459, as predicted by equation (A.16).

In Chapter 4, the ratios E_R/E_C and E_D/E_C were equal to 3.636. Figure A.2 demonstrates that under these circumstances, the limiting value of $\nu_C/(1-\nu_C)$=..459 overestimated by 28.93% the more precise value (.356) predicted by the model presented here.